

Technische Universität München  
Max-Planck-Institut für Plasmaphysik

# Development and Application of a Nonlinear Axisymmetric Resistive MHD-Code

**Christian Wigger**

Vollständiger Abdruck der von der Fakultät für Physik der  
Technischen Universität München zur Erlangung des  
akademischen Grades eines Doktors der Naturwissenschaften  
(Dr. rer. nat.) genehmigten Dissertation.

Vorsitzende: Univ.-Prof. Dr. K. Krischer  
Prüfer der Dissertation: 1. Hon.-Prof. Dr. S. Günter  
2. Priv.-Doz. Dr. A. Ulrich

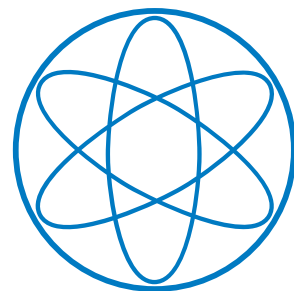
Die Dissertation wurde am 03.03.2011 bei der Technischen  
Universität München eingereicht und durch die Fakultät für  
Physik am 16.06.2011 angenommen.



# Development and Application of a Nonlinear Axisymmetric Resistive MHD-Code

PhD Thesis at the Max-Planck-Institut für Plasmaphysik  
Garching and the Technische Universität München

by  
Christian Wigger





# Contents

<b>1</b>	<b>Introduction</b>	<b>1</b>
<b>2</b>	<b>Theory</b>	<b>5</b>
2.1	Magnetohydrodynamics (MHD) . . . . .	5
2.2	Tokamak . . . . .	7
2.3	Equilibrium and passive stabilization . . . . .	14
2.4	Current filament model and resistive wall modes . . . . .	17
2.5	Passive conductors in ASDEX Upgrade . . . . .	22
<b>3</b>	<b>Code description</b>	<b>25</b>
3.1	Assumptions and adaption to the problem . . . . .	25
3.2	Extension of an existing linear model . . . . .	27
3.3	Non-linear resistive MHD code . . . . .	33
3.3.1	Code version for $\beta = 0$ . . . . .	33
3.3.2	Extension to finite $\beta$ . . . . .	36
3.3.3	Normalization . . . . .	39
3.4	Solving the system of equations . . . . .	40
3.4.1	Passive Stabilizing Loops (PSL) . . . . .	43
3.4.2	Boundary conditions . . . . .	43
3.4.3	Remarks on the conductivity $\sigma$ and the force term . . . . .	47
3.4.4	Dissipation . . . . .	48
<b>4</b>	<b>Application and results</b>	<b>51</b>
4.1	Testing and validation . . . . .	51
4.1.1	Vertical movement . . . . .	53
4.1.2	Passive conductors . . . . .	54
4.1.3	Plasma pressure . . . . .	61
4.2	Effect of boundary conditions . . . . .	63
4.3	Comparison with current filament model . . . . .	67
4.3.1	Resistive growth . . . . .	70
4.4	Application to realistic plasma configurations at ASDEX Upgrade	72
4.4.1	Moderately unstable cases . . . . .	72
4.4.2	Strongly unstable cases . . . . .	84

---

4.4.3	Approach to marginal stability . . . . .	87
4.4.4	Stabilization by a continuous resistive wall . . . . .	89
<b>5</b>	<b>Summary and Outlook</b>	<b>93</b>
<b>A</b>	<b>Appendix</b>	<b>97</b>
A.1	Finite element method . . . . .	97
A.1.1	Shape functions . . . . .	97
A.1.2	Solving partial differential equations . . . . .	101
A.1.3	Boundary conditions . . . . .	103
A.1.4	Time-dependent problems . . . . .	104
A.1.5	Patch recovery . . . . .	105
A.2	Contouring . . . . .	107
A.3	Slip Motion Condition . . . . .	107
A.4	Vorticity equation . . . . .	108
A.5	Resistance and inductance of the PSL . . . . .	110
A.6	Estimate of required computer resources for building up a data base of VDE growth rates . . . . .	111
	<b>Bibliography</b>	<b>111</b>

# 1 Introduction

The World Energy Council (WEC) has recently developed several energy policy scenarios. All of them predict an increase of the world's energy demand of 70 to 100 % in the next 40 years compared to today's level [1]. At the same time, it warns of the risks that go along with the climate change, most of all caused by the emission of  $CO_2$  into the atmosphere. Considering this, research in the sector of regenerative and ecofriendly technologies appears to be more important than ever. One of these technologies is the production of energy by fusion of light particles in a reactor. The concept of energy production by fusion is much older than the insight that a change of thinking concerning the way we live and produce energy is inevitable. Fortunately, it gains more relevance and attention nowadays, a part of it surely owed to the closeness to reaching the goal and the impressive milestones on that way (for example the construction of the large fusion device ITER in Cadarache, France).

The principle of fusion is easily explained. The actual mass of an atomic nucleus with the atomic number  $A$  is not the sum of the  $Z$  protons with the mass  $m_p$  and the  $A - Z$  neutrons with the mass  $m_n$  of which it consists. It is slightly lighter, which is described by the so-called mass defect

$$\Delta = [Zm_p + (A - Z)m_n] - m_z.$$

The mass defect has been converted to energy, following Einstein's famous equation  $E = \Delta c^2$  when the nucleus was formed. The energy that has to be converted to mass when disassembling the nucleus to its constituents is called binding energy. Figure 1 shows the binding energy per nucleon. Processes that lead to a higher amount of binding energy per nucleon lead to a conversion of mass to energy. Nuclei with  $A < 56$  (iron) have to merge to gain energy (fusion), those with higher atomic numbers have to split (fission).

For two nuclei to merge the long range coulomb repulsion has to be overcome so that the short-range nuclear attraction can lead to the formation of a compound nucleus. To get over the so called Coulomb barrier, particles need high energies. For a thermic ensemble, that means extremely high temperatures (about  $10^8 K$  corresponding to  $\approx 10^4 eV$ ). At this temperature, they are completely ionized and constitute a plasma consisting of ions and electrons. As there is the same

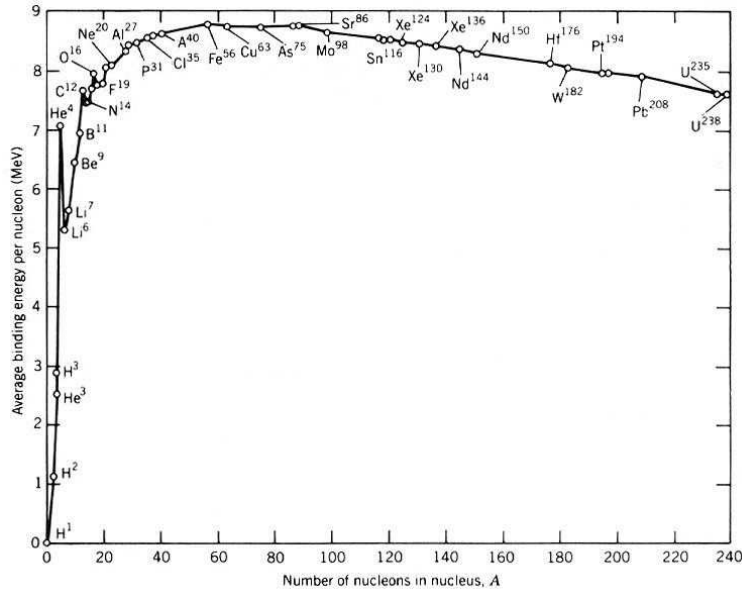


**Figure 1.1:** Binding energy per nucleon (taken from [2])

amount of protons and electrons in the plasma, it is macroscopically neutral. Nevertheless, its constituents react to electromagnetic fields, which makes the confinement of a plasma possible in the first place, as no wall material could stand those temperatures without vaporizing and polluting the plasma. Instead, magnetic fields force the ions and electrons on gyrating orbits. The most advanced concept to confine a plasma is a fusion reactor called tokamak, a toroidal axisymmetric device in which currents in external conductors and in the plasma keep the appearing electromagnetic and expansive forces in balance. The most favorable fusion condition is achieved with Deuterium and Tritium:



Among all reactions of interest, it has the largest reaction rate at temperatures achievable in a reactor, as is shown in figure 1.2. A large fraction of the energy (14.1 MeV) goes to the neutrons, which heat a blanket that surrounds the plasma. The transformation to electrical energy is accomplished by conventional means. For an economically useful fusion reactor, the heat produced by fusion of nuclei has to exceed the externally applied heat to initiate (and possibly sustain) the fusion process by a significant factor  $Q$  ( $>20-40$ ). Therefore it is important to find configurations of the system that enable to confine and thermally isolate a hot plasma for a long time, i.e. there must exist an equilibrium of all forces that is stable or can be stabilized by other means. While an equilibrium of expanding and confining forces is relatively easy to find, its stability is still a

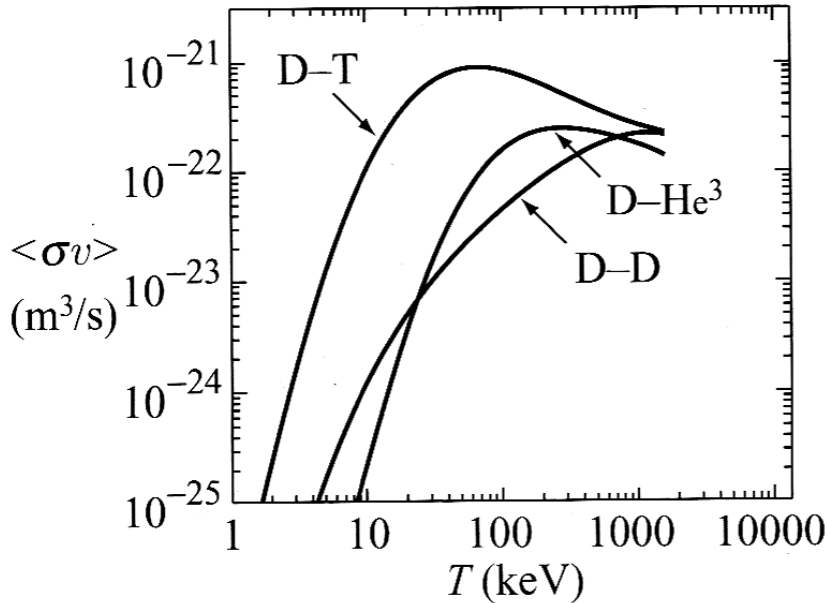


**Figure 1.2:** Velocity averaged cross-sections for the  $D - T$ ,  $D - He^3$  and  $D - D$  reactions as a function of temperature. (taken from [2])

problem and topic of intensive research. There are many different kinds of instabilities caused by a large variety of reasons and evolving both on microscopic and macroscopic length and time scales. One of these macroscopic instabilities affects the vertical position of the plasma column. Due to the external currents that are necessary to give the plasma a desired D-shape (this issue is addressed in detail in section 2.3), small deviations from the equilibrium position lead to a force that accelerates the whole plasma column in essentially vertical direction. If undamped, these movements can result in potentially dangerous mechanical stresses and excessive localized heat loads which would damage the vessel. This is an important concern in the design of ITER [15]. They can be counteracted by externally applied magnetic fields (active feedback). However, as they take place on the very fast magnetohydrodynamic time scale, passive conductors like walls or other dedicated structures must be used to dampen the movement to a slower time scale, which gives the active feedback system the time to calculate and establish the necessary correction fields.

For small amplitudes and growth rates of these axisymmetric perturbations, observations on the fusion experiment ASDEX Upgrade agree well with predictions made by an ad-hoc engineering expression. However, growth rates of configurations with stronger destabilizing forces, which are of practical interest as they allow more advantageous plasma parameters (confinement time, temperature, thermal energy density, ...), exceed substantially the predictions by the engineer-

ing model. The aim of this work is to develop a code that models the axisymmetric time evolution of a given plasma configuration. Of particular interest is the non-linear development of the instabilities, as it determines the limits of intervention by a control system and the potential damage to the device. To analyze the situation we chose to develop ab-initio an own code, as we wanted to have full control over assumptions and flexibility to adjust to the specific experimental conditions of ASDEX Upgrade. As this instability is very sensitive to the detailed nature (shape, conductivity distribution, electrical connections) of the stabilizing conducting structures, the capability to accurately model complex, 2-d structures was deemed essential.

Contrary to the engineering model, the plasma motion is not restricted to a rigid shift and both plasma and conducting structures have finite conductivity. All quantities, e.g. magnetic flux, pressure and current distribution, can be modeled accurately by using finite elements at each point of time.

There exist only two other codes which treat the non-linear axisymmetric dynamics of toroidal plasmas: DINA[6] and the Tokamak Simulation Code (TSC)[11]. Like the code developed in this work, both model only cases for which plasma inertia does not play a part: DINA calculates sequences of axisymmetric force equilibria and TSC (like done here) assumes an artificially enhanced plasma mass, making the problem numerically tractable (by reducing the Alfvén speed and hence easing the constraints set by the Courant-Friedrichs-Lewy condition) without affecting the numerical results.

This work is structured as follows: Chapter 2 deals with the theoretical background of plasma physics and the tokamak. A complete set of equations is developed that accounts for the special limitations and simplifications immanent to the problem of axisymmetric instabilities. A simple wire model is also presented that exhibits characteristic qualities of purely vertical instabilities and serves as reference for comparison with code results. Chapter 3 describes in detail the development of the code and the way the dependent variables are dealt with. It shows the results of first applications to simple test cases, including growth rates, current distributions and the comparison to the analytically expected behavior. Chapter 4 documents the comparison of the experimental data obtained on ASDEX Upgrade with the code adapted to its specifications. Chapter 5 finally concludes the work.

# 2 Theory

## 2.1 Magnetohydrodynamics (MHD)

A plasma is a gas consisting of free charged ions and electrons. Depending on which information is of interest, several physical models exist to describe the plasma that are valid on different space and time scales. For example, microinstabilities or fast particle transport require a kinetic model at some point, whereas problems concerning the macroscopic equilibrium or stability are preferentially treated with a fluid model. The scope of this work is to simulate the macroscopic, predominantly vertical instability of a plasma column, hence the latter model is an appropriate choice. The simplest fluid model is called magnetohydrodynamics (MHD). It is a combination of the Navier-Stokes equation of fluid dynamics and Maxwell's equations of electrodynamics and contains electrodynamic, inertial and pressure forces appearing in a plasma.

The governing equations of the resistive MHD are [33]

$$\frac{\partial \rho}{\partial t} + \nabla \cdot \rho \mathbf{v} = 0 \quad (\text{Continuity equation}) \quad (2.1)$$

$$\rho \frac{d\mathbf{v}}{dt} - \mathbf{J} \times \mathbf{B} + \nabla p = 0 \quad (\text{Equation of motion}) \quad (2.2)$$

$$\rho \frac{\partial e}{\partial t} + \rho(\mathbf{v} \cdot \nabla) e + (\gamma - 1) \rho e \nabla \cdot \mathbf{v} + \nabla \mathbf{q} = \mathbf{J} \cdot \mathbf{E} + R_{\text{Rad}} \quad (\text{Energy balance}) \quad (2.3)$$

$$\mathbf{E} + \mathbf{v} \times \mathbf{B} = \frac{1}{\sigma} \mathbf{J} \quad (\text{Ohm's law}) \quad (2.4)$$

$$\nabla \times \mathbf{E} = -\frac{\partial \mathbf{B}}{\partial t} \quad (\text{Faraday's law}) \quad (2.5)$$

$$\nabla \times \mathbf{B} = \mu_0 \mathbf{J} \quad (\text{Ampère's law}) \quad (2.6)$$

$$\nabla \cdot \mathbf{B} = 0 \quad (2.7)$$

where

$\mathbf{E} =$	electric field	$\mathbf{B} =$	magnetic field
$\mathbf{J} =$	current density	$\rho =$	mass density
$\mathbf{v} =$	velocity	$p =$	pressure
$\mathbf{q} =$	heat flux	$R_{\text{Rad}} =$	energy loss due to radiation
$\sigma =$	conductivity	$e =$	internal energy

and the convective derivative  $\frac{d}{dt} = \frac{\partial}{\partial t} + \mathbf{v} \cdot \nabla$  .

Equations (2.1)-(2.3) describe the time evolution of mass, momentum and energy, equations (2.4)-(2.7) govern the behavior of the electric and magnetic fields. In a dynamic problem, eq. (2.7) has to be satisfied only by the initial condition, as in the further evolution eq. (2.6) ensures that the magnetic field is divergence-free.

In this closed set of equations, some assumptions and simplifications are made, the most important are:

- The plasma is collision dominated: a fluid model requires a high collisionality. The distribution function then becomes nearly Maxwellian and particles stay close to each other on the time scale of interest.
- The plasma is described as a single fluid: instead of using an equation for ion and electron movement, the fluid is described as if it would consist of only one species. The electron mass is neglected and since the ions carry the momentum the fluid velocity is given by the velocity of the ions.
- The displacement current can be neglected: all phase velocities of electromagnetic waves in the plasma are small compared to the velocity of light. The displacement current does not play a role and is neglected in eq. (2.6).
- The plasma is quasi-neutral: the electron and ion density are equal, i.e. there are no macroscopic space charges. This assumption is justified as we are considering space scales large compared to the Debye length and frequencies low compared to the plasma frequency [12] .

The term describing the magnetic force on the left hand side of eq. (2.2) can be transferred into an intuitive form when expressing the current by eq.(2.6):

$$\mathbf{J} \times \mathbf{B} = \frac{1}{\mu_0} (\nabla \times \mathbf{B}) \times \mathbf{B}, \quad (2.8)$$

and using

$$\frac{1}{2}\nabla(\mathbf{B} \cdot \mathbf{B}) = (\mathbf{B} \cdot \nabla)\mathbf{B} + \mathbf{B} \times (\nabla \times \mathbf{B})$$

which leads to

$$\mathbf{J} \times \mathbf{B} = -\nabla \left( \frac{B^2}{2} \right) + B \cdot \nabla B \quad (2.9)$$

The first term on the right hand side is called the magnetic pressure that applies perpendicular to the field lines, the second is the magnetic tension and is directed along magnetic field lines.

In static equilibrium, these forces balance the kinetic pressure of the plasma and allow its containment.

Contrary to the so-called "ideal MHD", the resistivity of the plasma and surrounding structures is taken into account. That means that currents and magnetic fields will dissipate due to ohmic losses and magnetic field lines can tear apart, if that is energetically advantageous. The known phenomenon of the frozen flux (the coupled movement of magnetic field and plasma) does not hold strictly anymore in resistive MHD but the regions where reconnection takes place is typically only a small part of the plasma.

## 2.2 Tokamak

The aim of this work is to examine axisymmetric instabilities of toroidal plasmas. Preceding to a stability analysis, a state of stationary force equilibrium is necessary. The simplest device to get a plasma in equilibrium not prone to end losses (i.e. loss of plasma due to open ends of the device) is a so-called tokamak, a transliteration of the Russian acronym for toroidal chamber with magnetic coils. One of the biggest European tokamaks, ASDEX Upgrade (**A**xisymmetric **D**ivertor **E**xperiment), is located at the Max-Planck-Institut für Plasmaphysik in Garching and the code described in the following was developed with emphasis on the application to it. With simple adjustments (favoured by the finite element approach taken in it) it can, of course, be readily applied to other devices. In fact, this is done in section 4.4.4, where simulations are carried out not for the present ASDEX Upgrade, but a potential future "upgrade" of it, which differs, apart from the bigger plasma, essentially also in the structure of passive stabilizing elements.

The basic structure is shown in figure (2.1). Several sources of magnetic fields are necessary to keep the plasma confined. In this way, an expansion of the plasma

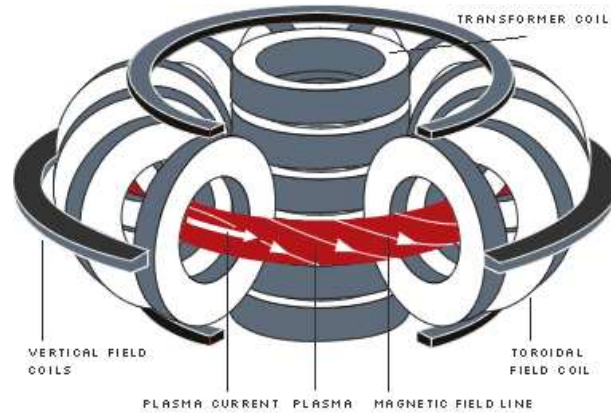


**Figure 2.1:** Tokamak Scheme (taken from [28])

and contact with wall structures is inhibited. The field in toroidal direction (see figure 2.2),  $B_\phi$ , which is generated by toroidal field coils, is the strongest. The weaker poloidal field,  $B_p$ , is mainly generated by the toroidal plasma current  $I_{tor}$ , which in turn is induced by a large central solenoid. It acts as the primary winding of a transformer, using the plasma itself as secondary winding (see figure 2.3).

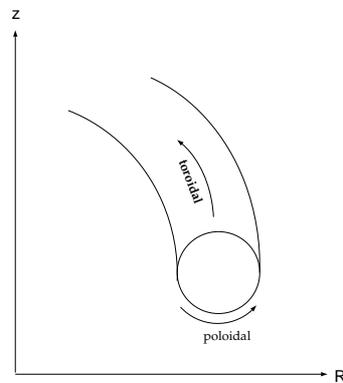


**Figure 2.2:** Denotation of directions in a tokamak

Additionally to the magnetic field generated by the plasma current, a vertically oriented magnetic field  $B_{vert}$  generated by external currents contributes to the poloidal field. It counters the radially outward directed forces due to the toroidal geometry and is described in more detail in chapter 2.3. The combination of toroidal and poloidal fields results in helical field lines, in their center lies the magnetic axis (see figure 2.4).

In cylindrical coordinates,  $R$  points radially outwards and is called major radius.

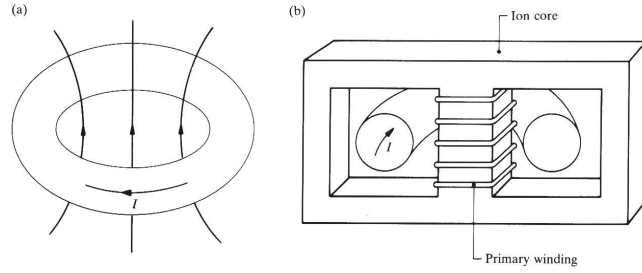


**Figure 2.3:** transformer principle (taken from [10])

$R_0$  is the distance of the torus axis to the magnetic axis.  $\mathbf{e}_\phi$  and  $\mathbf{e}_z$  are the unit vectors in toroidal and vertical direction, respectively.

For an axisymmetric, static equilibrium (i.e. there are no inertia terms) the momentum balance (2.2) reads:

$$\mathbf{J} \times \mathbf{B} - \nabla p = \rho \frac{d\mathbf{v}}{dt} = 0 \tag{2.10}$$

$$\Rightarrow \mathbf{B} \cdot \nabla p = 0, \quad \mathbf{J} \cdot \nabla p = 0.$$

$\mathbf{B}$  and  $\mathbf{J}$  lie on surfaces of constant pressure that build nested tori (see fig. 2.5).

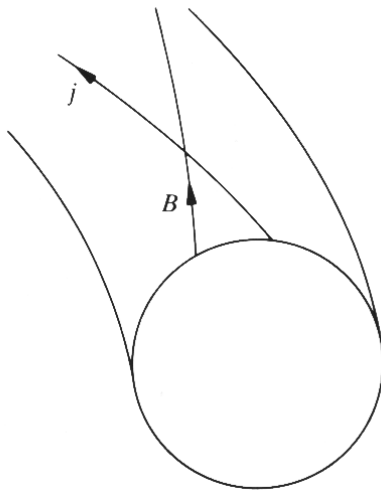


**Figure 2.4:** Magnetic field line and current density on a flux surface.

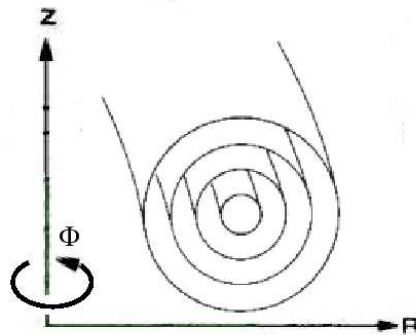


**Figure 2.5:** Nested tori (taken from [10])

These surfaces can be labeled with single-valued functions that define them

uniquely. Possible labels beside the pressure  $p$  are the enclosed volume or the enclosed poloidal flux  $\Psi_p$  with

$$\Psi_p = \int \mathbf{B}_p \cdot d\mathbf{A}_p. \quad (2.11)$$

$\Psi_p$  describes the flux of the poloidal magnetic field through a poloidal surface element shown in figure 2.6 (the toroidal analogon can be defined as well, shown in the same figure). Due to the constancy of the flux integrals on the surfaces, these are also called flux surfaces. The poloidal flux function  $\Psi$  is defined as the total flux per radian and differs from  $\Psi_p$  only by a factor of  $2\pi$ :

$$\Psi = \frac{1}{2\pi} \Psi_p.$$

Throughout the following work, only the definition for the flux per radian is used, as it is the common definition in equilibrium literature. The poloidal magnetic field can then be written as

$$\mathbf{B}_p = -\frac{1}{R} \mathbf{e}_\phi \times \nabla \Psi. \quad (2.12)$$

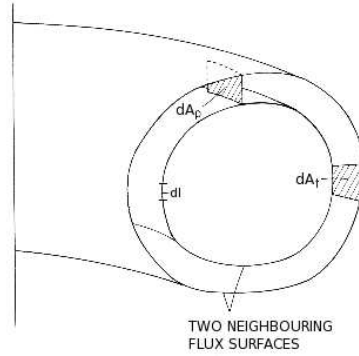


**Figure 2.6:** Poloidal and toroidal surface elements  $dA_p$  and  $dA_t$  and line element  $dl$  (taken from [9])

Analogously to the magnetic field, a function  $F$  related to the poloidal current (with contributions of the plasma and the toroidal field coils) can be defined:

$$F = -\frac{1}{2\pi} \int \mathbf{J}_p \cdot d\mathbf{A}_p = \frac{R B_\phi}{\mu_0}, \quad (2.13)$$

$$\mathbf{J}_p = -\frac{1}{R} \mathbf{e}_\phi \times \nabla F. \quad (2.14)$$

This definition allows for a different writing of the toroidal magnetic field:

$$B_\phi = \mu_0 \frac{F(\Psi)}{R}. \quad (2.15)$$

Inserting 2.12 in Ampère's law leads to the following representation of the current density:

$$\mu_0 \mathbf{J} = -\mu_0 \frac{1}{R} \Delta^* \Psi \mathbf{e}_\phi + \frac{1}{R} \nabla(RB_\phi) \times \mathbf{e}_\phi, \quad (2.16)$$

where the operator  $\Delta^*$  is given by

$$\Delta^* = R^2 \nabla \cdot \left( \frac{1}{R^2} \nabla \right) = R \frac{\partial}{\partial R} \left( \frac{1}{R} \frac{\partial}{\partial R} \right) + \frac{\partial^2}{\partial z^2}.$$

Using  $p = p(\Psi)$  and inserting the definition for  $F$  in the equation of motion (2.2) leads to the Grad-Shafranov equation:

$$\Delta^* \Psi = -\mu_0 R^2 \frac{dp}{d\Psi} - F \frac{dF}{d\Psi} = -\mu_0 R J_\phi. \quad (2.17)$$

This equation is a semi-linear partial differential equation that governs  $\Psi$  and gives the flux surface topology  $\Psi(R, \phi, z)$ . Usually the poloidal current and pressure profiles  $F(\Psi)$  and  $p(\Psi)$  are prescribed and the equation is solved numerically.

## Definition of $\beta$

A figure of merit associated with the plasma pressure is the ratio of the volume averaged plasma pressure to the averaged magnetic energy, called  $\beta$ . It is useful to define the following relation containing the plasma pressure and the poloidal component of the magnetic field, called the poloidal  $\beta$  or  $\beta_p$ :

$$\beta_p = \frac{2\mu_0 \bar{p}}{\langle B_p^2 \rangle}, \quad (2.18)$$

where

$$\bar{p} = \int p \, dA / \int dA$$

is the average of the pressure over the plasma area in the poloidal plane and

$$\langle B_p^2 \rangle = \oint_{\Psi_b} \frac{RB_p^2 dl}{|\nabla\Psi|} / \oint_{\Psi_b} \frac{R dl}{|\nabla\Psi|}$$

is the average value of  $B_p^2$  on the outermost closed flux surface (flux surface mean). In the remainder of this work, only the poloidal  $\beta$  will play a part.

The significance of  $\beta$  can be seen by taking a circular plasma and a large aspect-ratio. The poloidal field on the surface can be written as

$$B_{p,a} = \frac{\mu_0 I_p}{2\pi a}$$

where  $I_p$  is the plasma current and  $a$  the plasma radius. After partial integration of the numerator of eq. (2.18) for a circular, large aspect-ratio plasma and using the pressure balance, it follows [45]:

$$\beta_p = 1 + \frac{1}{(aB_{p,a})^2} \int_0^a \frac{dB_\phi^2}{dr} r^2 dr, \quad (2.19)$$

where  $r$  denotes a radial variable in direction of the plasma radius. If there are no poloidal currents, the integrand of eq. (2.19) vanishes and  $\beta_p = 1$ . The plasma does not change the toroidal field produced by the toroidal field coils. A value of  $\beta_p$  larger than one means that  $\frac{\partial B_\phi^2}{\partial r}$  is positive. In this case, the vacuum toroidal field plays a part in confining the plasma, as the poloidal field is not sufficient (the plasma is diamagnetic relative to the toroidal field) to balance the kinetic pressure of the plasma. For  $\beta_p$  smaller than one, the pressure cannot compensate the magnetic pressure from the poloidal field, so that the toroidal field is compressed and increased. The plasma is paramagnetic relative to the toroidal field. All three cases,  $\beta_p < 1$ ,  $\beta_p = 1$ , and  $\beta_p > 1$  are shown in figure 2.7.

The most extreme case for diamagnetic plasmas is for  $\beta_p = 0$ . Such a plasma can be either extremely cold ( $T = 0$ ) or extremely thin ( $\rho \rightarrow 0$ ) and hot. As there are no pressure forces, the electromagnetic forces have to balance among themselves, which implies  $\mathbf{J} \times \mathbf{B} = 0$ , leading to the expression of "force-free" magnetic fields.

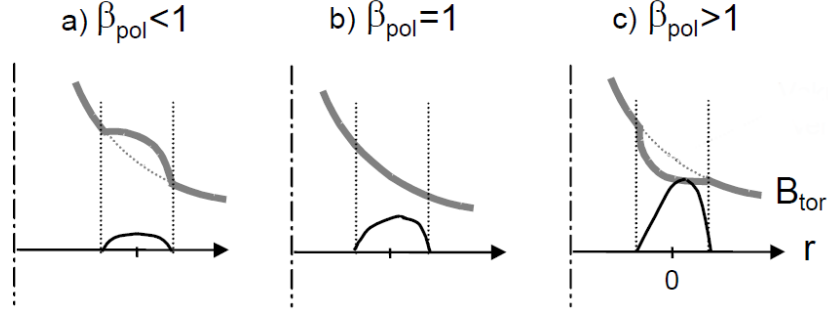


**Figure 2.7:** Change of the toroidal field for different values of  $\beta$ . The dotted line shows the toroidal field as it is generated by the toroidal field coils. The solid grey line is the sum of toroidal field contributions from the coils and the plasma. The solid black line is a measure for the plasma pressure. Taken from [47]

### Definition of the safety factor $q$

The name safety factor derives from the fact that, in general, high values of  $q$  lead to an increased stability of the plasma against current driven modes. In a tokamak, field lines follow helical paths on flux surfaces due to the superposition of toroidal and poloidal magnetic fields. A field line that starts at a toroidal angle  $\phi$  at a certain position in the poloidal plane will return to that poloidal position after a change of toroidal angle  $\Delta\phi$ . The  $q$  value of this field line is defined as

$$q = \frac{\Delta\phi}{2\pi}. \quad (2.20)$$

$q$  is a flux quantity, so this relation holds for any field line on a flux surface. If a field line joins up on itself after  $m$  toroidal and  $n$  poloidal rotations,  $q = m/n$  is rational and the connected flux surface is called resonant surface. If  $q$  is irrational, the surface is called ergodic and the field lines cover the whole flux surface when following their trajectories. To calculate  $q$  for a general, numerically computed equilibrium, one starts from the field line equation for the magnetic field in a torus

$$\frac{R}{dl} \frac{d\phi}{dl} = \frac{B_\phi}{B_p}$$

and inserts this relation in eq. (2.21), which yields:

$$q(\Psi) = \frac{1}{2\pi} \oint_\Psi \frac{1}{R} \frac{B_\phi}{B_p} dl. \quad (2.21)$$

## 2.3 Equilibrium and passive stabilization

The Grad-Shafranov equation describes a plasma equilibrium completely. It can be split into contributions that would be present even in a straight cylinder (corresponding to an infinite aspect ratio) and such contributions which have their origin in the toroidicity of the tokamak. The "straight" part requires that the expansive kinetic pressure is balanced by compressing magnetic forces. The toroidal contribution consists of three forces that are directed outward or inward in major radius direction. The first one is the hoop force that can also be observed at a current carrying loop of wire. Due to flux conservation, the magnetic pressure on the inside of the plasma column is larger than on the outer area, leading to an outward directed net force. The second one is the tire tube force. In the plasma, the constant pressure lies on nested isocontour lines, but as the surface on which the pressure is exerted is smaller on the inside than on the outer area, there is a further net force in the same direction. It is the tire tube force that leads to an outward shift of the inner flux surfaces in an equilibrium. The third force applies to the plasma in the case of  $\beta \neq 1$ , because this configuration allows for poloidal currents that cross with the toroidal field. As the toroidal field gets stronger towards the torus axis and the current has to close on a flux surface, a net force results that is directed outwards ( $\beta > 1$ ) or inwards ( $\beta < 1$ ).

Forces balancing the toroidal forces can be produced by either a conducting shell or external toroidal currents. In the case of a conducting shell, any radial expansion of the plasma column will lead to mirror currents in the shell that produce a vertical magnetic field which crosses with the toroidal current. This way, it generates an inward force so that the outward forces are balanced. In case of an ideally conducting shell, these mirror currents remain ad infinitum. If the wall has a finite resistivity, the mirror currents dissipate on the  $L/R$ -time of the conductor (where  $L$  denotes the inductance and  $R$  the resistivity, respectively). The other possibility, the usage of externally applied vertical fields, has the advantage of being independent of any  $L/R$ -time and is quite simple to realize. This method is mainly used in present tokamak experiments. A rough estimation of the magnitude of the vertical field for large aspect ratios gives: [14]

$$B_v = -\frac{\mu_0 I_p}{4\pi R_0} \left( \ln \frac{8R_0}{r} + \beta_p + \frac{l_i}{2} - \frac{3}{2} \right) \quad (2.22)$$

where the new quantity  $l_i$  denotes the dimensionless internal inductance per unit length of the plasma,

$$l_i = \frac{8\pi^2 \int B_p^2 r dr}{\mu_0^2 I_p^2}, \quad (2.23)$$

which is a measure for the "peakedness" of the current distribution and lies roughly between 0.5 and 1.5 for typical experimental plasmas.

So far, no attention was given to the stability of such an equilibrium. The question that arises when asking for vertical stability is, how the system reacts when the plasma moves an infinitesimal distance away from its equilibrium position. In the case of a homogeneous vertical applied magnetic field, the equilibrium behaves neutral (marginal stable) to the displacement, so there will neither be a restoring nor an enhancing force. The situation changes when the applied field gets curved. Curved field lines are the result of superimposing a quadrupole field to the vertical field. The parameter describing the resulting field is the field index

$$n = - \left( \frac{R}{B_{vert}} \frac{\partial B_{vert}}{\partial R} \right). \quad (2.24)$$

If  $n > 0$ , the vertical field lines have convex curvature as shown in figure 2.8. It is clear that a small upward (or downward) displacement will result in a restoring downward (upward) force, as there is a non-vanishing component of the cross product of the toroidal current and the radial magnetic field, that in both cases is directed towards the equilibrium position. Hence,  $n > 0$  corresponds to vertical stability.

The argumentation in the case of a radial displacement is slightly more complicated. as in this case, in addition to the radial variation of the applied vertical field, also the conservation of poloidal flux has to be taken into account, leading to a criterium for stability against this mode [14]

$$n < \frac{3}{2}.$$

A field index  $0 < n < \frac{3}{2}$  means stability in vertical and horizontal direction. Unfortunately, this condition is not fulfilled for plasmas in state-of-the-art tokamaks. For several reasons, the plasma in modern tokamaks is D-shaped, which includes a vertical elongation. A D-shape increases the energy confinement, as for the same value of  $q$  a higher current can be achieved. It allows a higher  $\beta$  value, that is a measure for the economical efficiency of the tokamak (see chapter 1), as it is more stable against pressure driven modes ([38]). Furthermore, as the toroidal field coils are D-shaped for reasons of homogeneous load distribution [16], the volume occupancy is optimized and finally, a divertor configuration in which a separatrix lies between regions of closed and open flux contours leads naturally to an elongation. To produce a vertically elongated plasma, there must be currents above and below the plasma with the same direction or currents beside the plasma with opposite direction (or both). The currents in the same

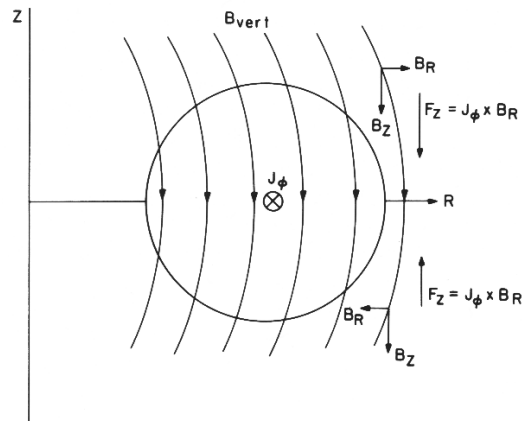


**Figure 2.8:** Resulting vertical forces  $F_z$  as product of crossing  $J_\phi$  and  $B_R$  for convex field lines. Taken from [9]

direction attract the plasma, whereas those of opposite direction repel it, leading to a stretching or squeezing. The basic arrangement is shown in figures 2.9 and 2.10.

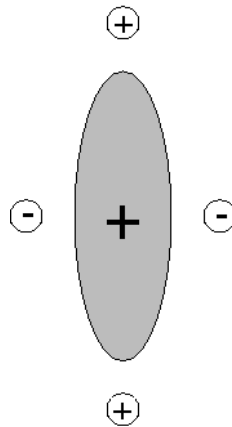


**Figure 2.9:** Basic arrangement of currents to elongate the plasma

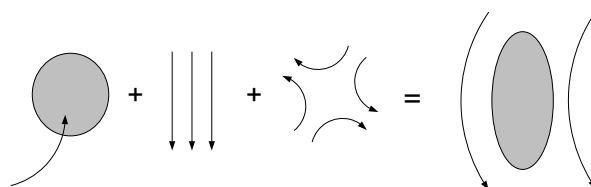


**Figure 2.10:** Superposition of vertical and quadrupole magnetic fields lead to an elongated plasma and a negative field index  $n$

The radial components of the quadrupole field generate together with the vertical field a concave curvature of the field lines. This leads to an unstable situation for the vertical position, as will be shown in section 2.4. Figure 2.11 shows the positions of the coils in ASDEX Upgrade that are necessary to create a plasma equilibrium with elongation and triangularity.  $V$  denotes the coils that are necessary for plasma shaping and balancing radial forces,  $OH$ -coils heat the plasma via Ohmic heating and induce the toroidal current and  $Co$ -coils are responsible for position control (active feedback).

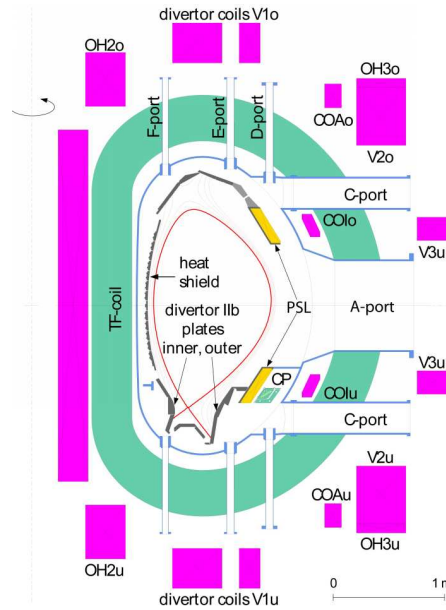


**Figure 2.11:** Poloidal field (PF) coils at ASDEX Upgrade

## 2.4 Current filament model and resistive wall modes

An unstable vertical movement of the plasma is also called vertical displacement event (VDE) or, as it concerns the whole plasma column and is axisymmetric,  $n=0$  mode ( $n$  is the toroidal mode number, that gives the periodicity of a distortion when a spectral analysis is carried out; the analogous poloidal mode number is denoted with  $m$ . In this terminology, the vertical displacement instability has a dominant  $m = 1$  component). The  $n = 0$  mode has no resonant surface inside the plasma, but the separatrix which divides closed field lines from open ones, is a resonant surface. On it holds  $q = \infty$ .

If undamped, the movement of such a mode occurs on Alfvénic time scale (for a realistic experiment in order of  $\mu s$ ) and can cause extreme stresses on the mechanical structures (in ASDEX Upgrade up to 1000kN). Besides the need of long discharge times, these VDEs are also a potential threat to the integrity of the device and must be suppressed.

Although the purpose of this thesis is a plasmaphysical description of axisymmetric instabilities, at first a very simple electrotechnical model of them is described in some detail. This allows to exhibit in a very transparent way the principle of their reduction in growth rates into a range amenable to active feedback systems (the concept of resistive wall modes), and the implications of a key plasma physics assumption made in the code: the usage of an artificially enhanced plasma inertia.

In this model, circular current filaments (formed to a ring) represent the plasma and the conducting structures, as shown in figure 2.12. The wire ring with index  $p$  is movable in vertical direction and has the radius  $R_0$ . It represents a plasma with infinite conductivity and is exposed to a curved external field whose direction is chosen so as to lead to an inward directed force on the current ring. This has no consequences in the wire model assuming a rigid ring, but simulates the situation in a tokamak, where the external fields have to balance the outward directed plasma expansion forces. The wires with index  $c$  are fixed in space and represent the conducting structures that are connected and treated as a system. The vertical force that acts on the "plasma ring" reads:

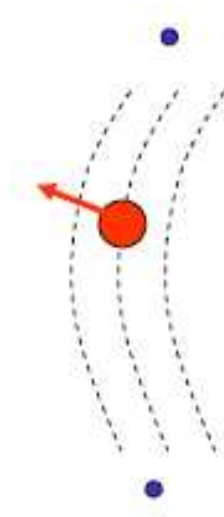


**Figure 2.12:** wire model: the red point symbolizes the vertically movable plasma, the smaller points the fixed passive conductors. The dashed lines are the magnetic field and the arrow is the resulting  $\mathbf{J} \times \mathbf{B}$  force.

$$F = m_p \cdot \frac{\partial^2 z}{\partial t^2} = 2\pi R_0 I_p B_R. \quad (2.25)$$

with  $m_p$  and  $I_p$  the plasma mass and plasma current, respectively,  $z$  the deviation of the plasma equilibrium position in vertical direction and  $B_R$  the radial component of the magnetic field.  $B_R$  vanishes at  $z = 0$  and has contributions from the applied external field and from induced currents in the conducting wires due to plasma movement. The external field leads, Taylor expanded and crossed with the plasma current  $I_p$ , to a force that is destabilizing, due to the considerations about the field index made above:

$$F_{destab} = -2\pi R_0 \frac{\partial B_{R,0}}{\partial z} I_p z. \quad (2.26)$$

The second contribution has its origin in the induction of eddy currents in the conductors. The vertical shift of the plasma wire leads to a change of the magnetic flux through the conducting wire loop, which again results in an induced current due to Faraday's Law. Following Lenz's rule, this current is directed in a way that tries to dampen the movement of the plasma filament, similar to the stabilizing effect of the conducting shell mentioned above. The magnetic field component at the position of the plasma filament is given by the spatial derivative of the (total) poloidal flux  $\Psi$  coupled to it :

$$\Psi = L_p \cdot I_p + M_{cp} \cdot I_c$$

$$B_R = -\frac{1}{2\pi R} \frac{\partial \Psi}{\partial z} = -\frac{1}{2\pi R} \frac{\partial M_{cp}}{\partial z} I_c$$

with  $I_c$  the current in the fixed conductors and  $M_{cp}$  the mutual inductance between the plasma and the conductors. The plasma current crosses with the radial magnetic field connected with the current in the conductor and the resulting force has a restoring effect:

$$F_{stab} = \frac{\partial M_{cp}}{\partial z} I_c I_p. \quad (2.27)$$

The circuit equation for the induction in the conductors reads (with  $\dot{I}_p = 0$  and  $L_c$  denoting the self-inductance of the passive conductors):

$$\frac{\partial \Psi}{\partial t} = \frac{\partial M_{cp}}{\partial z} I_p \dot{z} + L_c \dot{I}_c = -\mathcal{R}_c I_c, \quad (2.28)$$

For the moment, the resistance  $\mathcal{R}_c$  is set to zero, describing ideal conductors. Time integration of 2.28 leads to an expression for  $I_c$  :

$$I_c = -I_p \frac{\partial M_{cp}}{\partial z} \frac{z}{L_c}. \quad (2.29)$$

Insertion in eq. (2.27) results in

$$F_{stab} = - \left( \frac{\partial M_{cp}}{\partial z} \right)^2 I_p^2 \frac{z}{L_c}.$$

Obviously, the stabilizing effect is the stronger, the closer the passive conductor is positioned to the plasma (stronger coupling) and the smaller the self-inductance of the conductor is.

The equation of motion for the ring with the mass  $m_p$  reads:

$$m_p \cdot \frac{\partial^2 z}{\partial t^2} = - \left( \frac{\partial M_{cp}}{\partial z} \right)^2 I_p^2 \frac{z}{L_c} + 2\pi R_0 \frac{\partial B_{R,0}}{\partial z} I_p z. \quad (2.30)$$

As the vertical magnetic field necessary to counteract the toroidal expansive forces will be of order  $\frac{\mu_0 I_p}{2\pi R_0}$ , it is convenient to normalize the appearing magnetic fields to it, leading to the expressions:

$$d_{curv} = \frac{2\pi R_0^2}{\mu_0 I_p} \left( \frac{\partial B_{R,0}}{\partial z} \right)$$

$$s_{cond} = \frac{R_0 \left( \frac{\partial M_{cp}}{\partial z} \right)^2}{\mu_0 L_c}$$

where  $d_{curv}$  and  $s_{cond}$  denote the destabilizing contribution from the externally applied magnetic field and the stabilizing contribution due to the passive conductors, respectively.

Inserting these definitions into the force balance together with the exponential ansatz  $z, I_c \sim e^{\gamma t}$ , where  $\gamma$  denotes the growth rate, yields

$$\frac{1}{\gamma_0^2} \cdot \gamma^2 z = d_{curv} \cdot z - s_{cond} \cdot z$$

with

$$\gamma_0 = \sqrt{\frac{\mu_0 I_p^2}{m_p R_0}}.$$

The normalized growth rate  $\gamma^* = \gamma/\gamma_0$  reads then:

$$\gamma^* = \sqrt{s_{cond}} \sqrt{\frac{d_{curv}}{s_{cond}} - 1}.$$

If  $\frac{d_{curv}}{s_{cond}} < 1$ , the growth rate gets imaginary and hence the position of the plasma wire is stable and would oscillate if an external perturbation is applied. On the other hand, a ratio larger than 1 will lead to an acceleration of the movement on inertia (Alfvénic) time scale.

The inclusion of resistive effects gives a slightly more complicated picture. The circuit equation (2.28) describing the current in the conductors has now to consider a finite resistance of the filament, leading to an modified expression for  $I_c$ :

$$I_c = -I_p \frac{\partial M_{cp}}{\partial z} \frac{z}{L_c} \left( \frac{\gamma}{\gamma + \frac{\mathcal{R}_c}{L_c}} \right). \quad (2.31)$$

A new parameter consistent with the normalization can be introduced, that describes the resistive decay time of the eddy currents:

$$\gamma_w^* = \frac{\mathcal{R}_c/L_c}{\gamma_0}.$$

The dispersion relation for the growth rate with resistive conductors becomes:

$$\gamma^{*2} + s_{cond} \cdot \frac{\gamma^*}{\gamma^* + \gamma_w^*} - d_{curv} = 0 \quad (2.32)$$

with instability setting in already for  $d_{curv} > 0$  (rather than  $d_{curv} > s_{cond}$  for the ideal case). That means that a configuration with unstable curvature, which can be stabilized with ideal conductors, will inevitably be unstable when the conductors are resistive. The reason for this behavior is as follows: as stated above, a shift in the vertical position of the plasma leads to currents which flow in a direction to counteract the movement. In ideal conductors these currents could exist ad infinitum and plasma and conductors build a new equilibrium (if

the configuration is not already unstable even for ideal conductors). For resistive conductors, these currents dissipate on the resistive time scale  $\tau_R = L_c/\mathcal{R}_c$  and allow the instability to grow. However, the growth rate can be significantly reduced compared to the absence of any conductors, as the movement occurs on the same time scale as the decay of the currents (which is of the order of milliseconds for a realistic experiment). Due to the slow evolution of the instability, it can be seen as transition through a series of equilibria, determined by plasma position and currents in the inductors and inertia playing no role. As the growth rate is exclusively determined by the resistivity of the conducting structures and occur on the resistive time scale, these instabilities are also called resistive wall modes. This slowdown is the great practical relevance of passive stabilization, as it makes the usage of active feedback possible. Figure 2.13 shows the most unstable solutions of eq.(2.32) for different values of  $\gamma_w$  against  $\frac{d_{curv}}{s_{cond}}$ . It shows that the transition from resistive to inertia dominated growth at  $\frac{d_{curv}}{s_{cond}} = 1$  is quite abrupt for  $\gamma_w \ll 1$ , which is not surprising, considering that in the ideal case instability sets in at this value (with growth rates on inertia time scale). For small values of  $\gamma_w^*$  and  $\frac{d_{curv}}{s_{cond}} < 1$ , the unstable solution of eq. (2.32) is approximately given by

$$\frac{\gamma}{\gamma_w} \approx \frac{\frac{d_{curv}}{s_{cond}}}{1 - \frac{d_{curv}}{s_{cond}}}. \quad (2.33)$$

The same expression can be derived when neglecting the inertia term in the force balance. These solutions are drawn in the figure with dashed lines. For small  $\gamma_w$ , the approximation holds almost till  $\frac{d_{curv}}{s_{cond}} = 1$ .

## 2.5 Passive conductors in ASDEX Upgrade

The passive conductors in a tokamak are not idealized thin wires, but have a significant extension, frequently taking the shape of a complete wall. In ASDEX Upgrade, massive copper conductors formed to two loops connected in series build the passive stabilizing loops (PSL). They were installed because the resistive time of the conducting wall was too low (about 10 ms) to enable active feedback. The PSL have a resistive time of about 600 ms. Furthermore the inductive coupling to the plasma is significantly increased due to the proximity of the PSL. The intention of the PSL is to stabilize vertical movements of the plasma. Any spatially constant change of the poloidal flux encircled by loops will induce a current in both legs of the PSL of the same amount but different directions in a poloidal cross section, due to the series connection of both PSL legs. This change of flux can be the result of an vertical plasma movement which leads to opposite

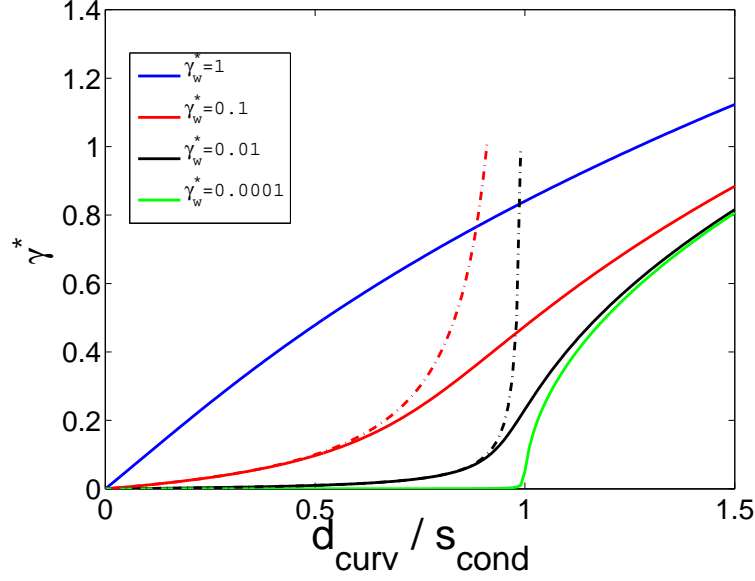


**Figure 2.13:** Normalized growth rates for different  $\gamma_w^*$  as result of eq. (2.32) (solid lines) and asymptotic solutions following equation (2.33) (dashed lines) when inertia is neglected.

currents in the upper and lower PSL. Radial movement, current dissipation, and compensation of Ohmic dissipation of the plasma current (by changing the flux through the central solenoid over time to induce a voltage along the toroidal circumference of the plasma) also lead to a change of flux through the loops. However, as the PSL are connected and both legs see the same induced voltage from the OH transformer, no current induction occurs. Figure 2.14 illustrates the connection and the resulting current direction. In a cross section at fixed toroidal angle  $\phi$ , the currents flow in opposite direction, whereas currents in the same direction are not possible.

As the PSL have a finite extension and are subject to the rules of induction, one expects a current distribution inside of them that deviates from homogeneity. This well-known phenomenon is called skin effect. Its origin is the induction of eddy currents inside the conductors (see figure 2.15). These currents weaken the original current in the middle and displace the current flow to a layer ('skin') on the surface. The skin depth is determined by

$$\delta = \sqrt{\frac{2}{\mu_0 \sigma \omega}}, \quad (2.34)$$

where  $\sigma$  is the conductivity and  $\omega$  the frequency of the current. For a circular conductor, the skin depth is the distance to the surface at which the current den-

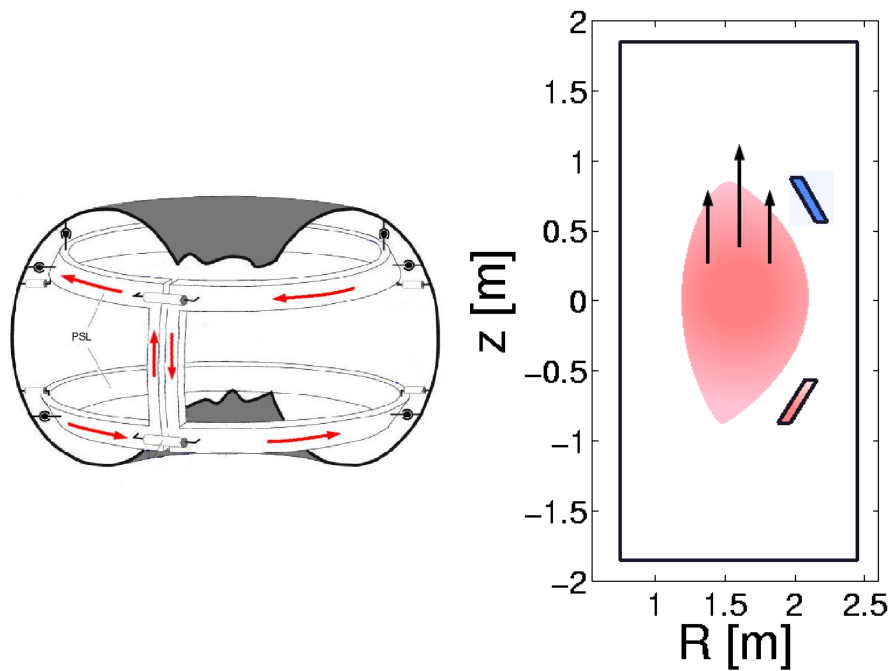


**Figure 2.14:** Current directions in the PSL. *Left:* total view of the PSL in ASDEX Upgrade. Red arrows mark an induced current. *Right:* poloidal cross section of the torus. An upward shift of the plasma column leads to induction of opposing currents in the upper and lower PSL.

sity drops by a factor of  $e^{-1}$ . The higher the frequency, the thinner is the layer; the same holds for the conductivity. At the same time, the effective resistance of the conductor increases, because the effective conducting cross section decreases.

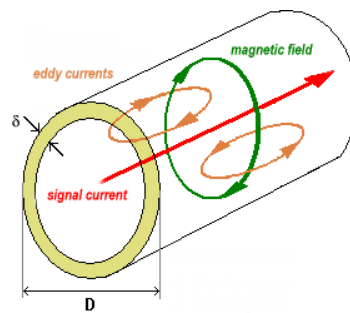


**Figure 2.15:** Skin effect

# 3 Code description

## 3.1 Assumptions and adaption to the problem

At this point, all necessary theoretical background about MHD, axisymmetric instability and passive stabilization is given. Theoretically, one could solve all the equations of chapter 2.1 to get the state of the plasma and the whole system around it at each point of time. But, of course, it is far too expensive to solve the complete system of equations in this framework. As a consequence, the problem is reduced to only those aspects that are relevant for the predominantly vertical instability and its stabilization.

The most important simplification is the limitation to two dimensions, as the vertical displacement is axisymmetric ( $n=0$ ). Most plasma instabilities can be stabilized by a sufficiently large toroidal magnetic field. Unfortunately, that does not hold for the vertical instability, as a linear examination of the energy contributions following the energy principle [7] shows. The energy principle states in simple words, that any displacement  $\xi$  of the plasma which leads to a negative variation of the potential energy of the system describes an unstable mode. The reason is energy conservation: as the sum of potential and kinetic energy must be conserved (neglecting losses due to radiation, resistivity and so on), the plasma must gain kinetic energy when lowering its potential energy. Generally, it is sufficient to examine the contributions of the potential energy if there is no need to determine exact growth rates. The total energy can be separated into contributions of the plasma and the surrounding vacuum:

$$\delta W = \delta W_p + \delta W_v$$

$$\delta W_p = \frac{1}{2} \int_{Plasma} \left[ (\nabla \times (\xi \times \mathbf{B}))^2 + (\mathbf{J} \times \xi) \cdot \nabla \times (\xi \times \mathbf{B}) + (\xi \cdot \nabla p) \nabla \xi + \frac{5}{3} p (\nabla \xi)^2 \right] dV$$

$$\delta W_v = \frac{1}{2} \int_{Vacuum} (\delta B_v)^2 dV,$$

where  $\xi$  denotes the displacement from equilibrium and  $\delta B_v$  the perturbed vacuum magnetic field.

If now only the contributions involving the toroidal magnetic field are considered,  $\delta W_p$  reads [4]

$$\begin{aligned} \delta W_p &= \frac{1}{2} B_\phi^2 R^2 \int_{Plasma} \left( \nabla \times \left( \xi \times \frac{1}{R} \mathbf{e}_\phi \right) \right)^2 dV \\ &+ \frac{1}{2} B_\phi R \int_{Plasma} \left( \nabla \times \left( \xi \times \frac{1}{R} \mathbf{e}_\phi \right) \right) \cdot (\mathbf{J} \times \xi) dV \end{aligned}$$

where  $\mathbf{e}_\phi$  denotes the unit vector in toroidal direction. The stabilizing vacuum contribution  $\delta W_v$  depends on  $B_\phi$  only through

$$B_\phi R \nabla \Psi \cdot \left( \nabla \times \left( \xi \times \frac{1}{R} \mathbf{e}_\phi \right) \right).$$

Thus, for all displacements  $\xi$  that fulfill the condition

$$\nabla \times \left( \xi \times \frac{1}{R} \mathbf{e}_\phi \right) = 0 \quad (3.1)$$

both contributions vanish and the toroidal field has no stabilizing contribution to the energy balance, no matter how large it is. The plasma "slips" through the toroidal field without doing any work against it. This condition is called "Slip Motion Condition" by Rebhan and Salat [3]. For an elliptical plasma and in the case of infinite aspect ratio,  $A = \infty$ , the most unstable mode that fulfills this condition has the poloidal mode number  $m = 1$ , corresponding to a rigid vertical shift [5] with  $\xi = \xi_z = const$ . Codes using the energy principle often use this test function to check equilibria against vertical instability. Due to the finite aspect ratio, the more general plasma shape and the influence of conducting structures in a realistic tokamak configuration, the shift will not be strictly rigid, but also include a component in radial direction.

By introducing a stream function  $\tilde{\eta}$  for the displacement (quite analogous to the flux function  $\Psi$  for the magnetic field) with

$$\xi = -R \cdot (\mathbf{e}_\phi \times \nabla \tilde{\eta}), \quad (3.2)$$

the Slip Motion Condition is inherently fulfilled (see section A.3). Differentiation with respect to time leads to a stream function  $\eta$  connected to the velocity:

$$\mathbf{v} = -R \cdot (\mathbf{e}_\phi \times \nabla \eta). \quad (3.3)$$

## 3.2 Extension of an existing linear model

A first approach for calculating realistic growth rates was to extend the existing linear eigenvalue code that has been developed in the framework of a diploma thesis. By using the Slip Motion ansatz and the energy principle [7], the code could calculate transitions from unstable to stable regimes in dependence on several parameters (e.g. proximity to conducting walls, plasma current, position of the PSL, etc.. for details see [39],[5]) but was constrained to ideally conducting plasmas and ideally conducting passive stabilizing elements. Some basic results - the reproduction of the transition point from stability to instability predicted by Laval [5] and the influence of present PSL - are shown in figure 3.1. The abscissa is the wall parameter  $\alpha = (a' - b)/(a - b)$ , where  $a$  and  $b$  denote the minor and major half-axes of the plasma and  $a'$  and  $b'$  those of the surrounding elliptical wall, respectively.

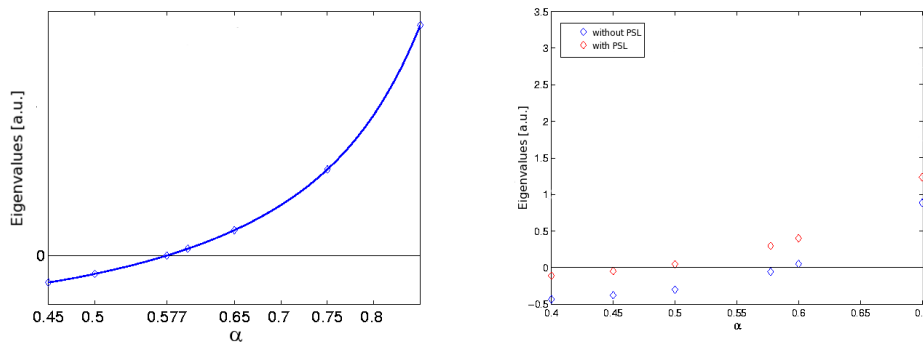


**Figure 3.1:** Eigenvalues (correlated to the growth rate) against the wall parameter  $\alpha$ . *Left:* analytical models predict point of marginal stability at  $\alpha=0.577$  for an elliptical plasma with  $\beta_p = 0$ , a flat current distribution and an aspect ratio of  $A = 50$ . This is reproduced by code results. *Right:* The point of marginal stability for the same plasma moves towards more distant walls when including PSL (their position is shown in figure 3.2).

For an assumed variation of all perturbed quantities like  $\sim e^{\gamma t}$ , the perturbation has to satisfy an energy balance

$$\delta W_p + \delta W_v + \gamma^2 K = 0. \quad (3.4)$$

$\delta W_p$ ,  $\delta W_v$  and  $K$  are quadratic expressions in  $(\xi, A_\phi)$  measuring the change in potential and kinetic energy of the system due to a virtual displacement.  $\xi$  denotes the displacement of the plasma and  $A_\phi$  is the toroidal component of the magnetic vector potential in the vacuum. Due to the inclusion of the vacuum

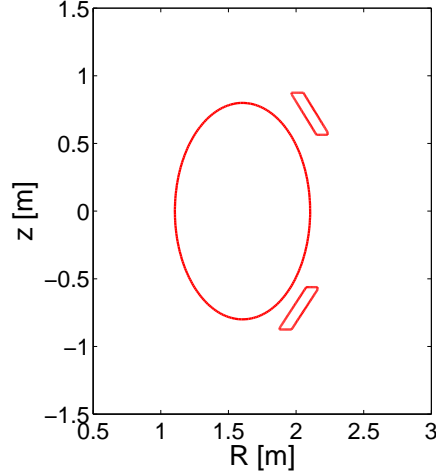


**Figure 3.2:** Plasma boundary for an elliptical plasma and position of the PSL in the code

into the calculations (where the density would ideally go to zero),  $K$  is replaced there by a quadratic expression in  $A_\phi$  with a small coefficient. Although  $\gamma$  loses thereby its physical meaning of growth rate (or, if imaginary,  $\text{Re}(\gamma)$  that of oscillation frequency), the sign of  $\gamma^2$ , and hence the question of existence of unstable perturbations, will not be affected.

In the framework of the diploma thesis this was justified, as only a statement of stability or not was aimed at and any passive structures were assumed to have infinite electrical conductivity. Nevertheless the code can be applied to a resistive case, and actually derive a true (though approximate) growth rate when we consider the regime where resistivity in the conducting structures rather than inertia determine the actual growth rate. In addition to the implementation of pressure terms in the plasma energy expression, the conductors are in the following assumed to be resistive. The energy balance is therefore extended by a term that describes the dissipated energy in the conductors due to Ohmic losses

$$\frac{\partial}{\partial t} \delta W_c = \mathcal{R} I_c^2,$$

where  $\mathcal{R}$  is the total resistance and  $I_c$  the current in the passive conductors. These currents are assumed to flow on the boundaries of the PSL which corresponds (following equation 2.34 for the calculation of the skin depth) to either very high conductivity, very large growth rates or both. The currents are driven by the variation of the flux linking them, i.e. determined by

$$2\pi \frac{\partial}{\partial t} (\Psi_1 - \Psi_2) = 2\pi \gamma (\Psi_1 - \Psi_2) = \mathcal{R} I_c \quad (3.5)$$

where  $\Psi_1$  and  $\Psi_2$  denote the value of the poloidal flux  $\Psi = R \cdot A_\phi$  on the surfaces of the upper and lower PSL. In the former code version, this difference is zero, as the PSL were ideal conductors and as both PSL form a closed loop through which no change of flux was allowed to occur. However, the condition of equal but opposed currents is kept.

The energy balance (still including inertia) from the perturbation would now read

$$\delta W = \delta W_p + \delta W_v + \frac{\mathcal{R}}{2\gamma} I_c^2 + \gamma^2 K = 0. \quad (3.6)$$

Eigenvalues of this equation would be in general complex and could be derived by suitable routines, taking note of the fact that, after substitution of  $I_c$  by  $\Psi = R \cdot A_\phi$ , the third term in eq. (3.5) becomes  $\sim \gamma$ . In the resistive wall mode case, however, the energy freed by the plasma displacement is used only to overcome the Ohmic dissipation in the conductors; we are thus interested in solutions in which the kinetic energy vanishes. Considering this and the fact that the model is only of transient interest, we adopt an approach allowing to use as much as possible of the structure of the already existing ideal code. Eq. (3.6) is therefore rewritten:

$$\delta W_p + \delta W_v + \frac{\lambda_c}{2} I_c^2 - \Lambda K = 0, \quad (3.7)$$

treating  $\lambda_c = \mathcal{R}/\gamma$  as a parameter, appearing both in eq. (3.7) and in the induction equation for the PSL (3.5). Equation (3.7) then becomes an eigenvalue problem with  $\lambda_c$  an (assumed) input parameter, and  $\Lambda(\lambda_c)$  as eigenvalue. Of relevance to us is only the result corresponding to  $\Lambda(\lambda_c^*)=0$ , which is obtained through parametric variation of  $\lambda_c$  as intersection (or via a suitable iterative search). The physics model and the energy balance equation corresponds to that used in the STARWALL code [46] for 3D resistive wall modes, although the solution procedure applied here is different.

If  $\Lambda = 0$  and  $\lambda_c > 0$ , the configuration corresponds to a situation where the plasma position is stable for ideal conductors but unstable if resistivity is taken into account. The growth rate can be calculated with the equation

$$\gamma = \frac{\mathcal{R}}{\lambda_c^*}. \quad (3.8)$$

If  $\Lambda$  is zero only for  $\lambda < 0$  the plasma is stable even for resistive conductors.

As an example, shot number 23348 is shown which was created for the purpose to

compare experimental with code results. The left picture in figure 3.3 shows the  $z$  position of the current barycenter versus time. Active feedback is deactivated in the red marked area and a vertical displacement event occurs.

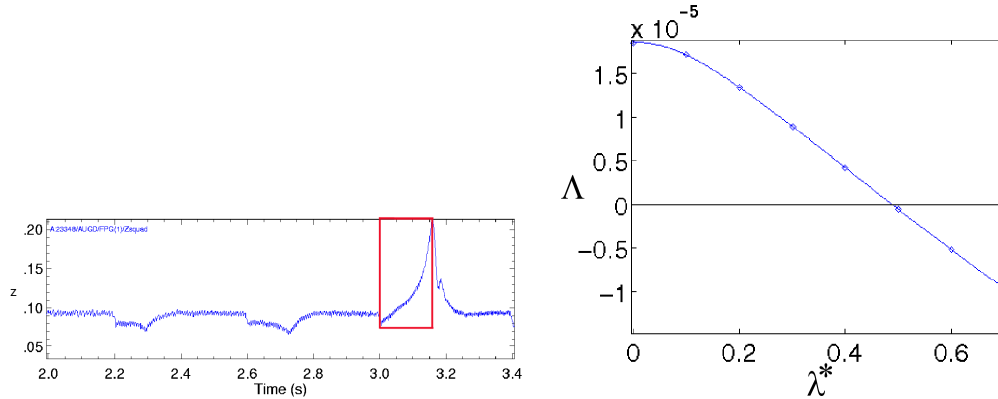


**Figure 3.3:** Left:  $z$  position of the current barycenter for shot number 23348. Right: Eigenvalue  $\Lambda$  versus the normalized parameter  $\lambda^*$ .

An exponential fit yields a growth rate of about 25 Hz. The right picture of figure 3.3 shows the transition of the sign of  $\Lambda$ . This point determines  $\lambda_c$  which yields, inserted in eq. (3.8), a growth rate of about 3.6 Hz.

There are several possible explanations for the strong difference between the experimental and theoretical value. First of all, the plasma is treated as if it would be a perfect conductor and as a result, no electromagnetic field can penetrate the separatrix. In reality, the plasma has a finite resistivity and following from that a skin depth in which electromagnetic waves can penetrate. That's why the shape of the plasma must be modified for the calculations to an effective plasma boundary. The skin depth is defined as  $\delta = \sqrt{\frac{2}{\mu_0 \sigma \omega}}$  (see section 2.5). Figure 3.4 shows the skin depth of copper and a plasma with different temperatures in dependence on the growth rate.

For three different values of the temperature at the boundary (with the simplifying assumption that the temperature is constant in this small boundary layer) the resulting separatrix shapes and the corresponding values for  $\gamma$  are shown in figure 3.5.

The dependence on the choice of the "cut off" plasma boundary is the most critical one and the code exhibits numerical problems when including the x-point into the calculations.

Furthermore the skin effect in the PSL has to be considered. The induced currents do not flow on the surface, as it would be the case with high-frequency alternating

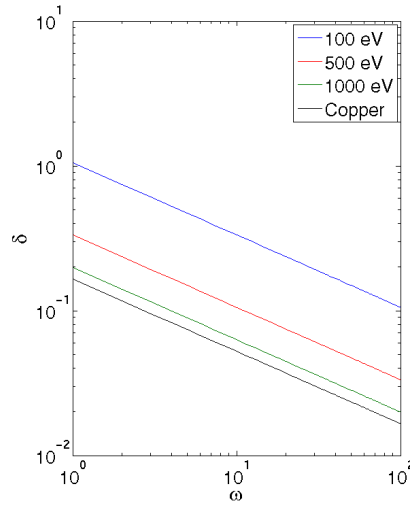


**Figure 3.4:** Skin depth for a plasma with different temperatures and copper in dependence on the growth rate (corresponding to a frequency).

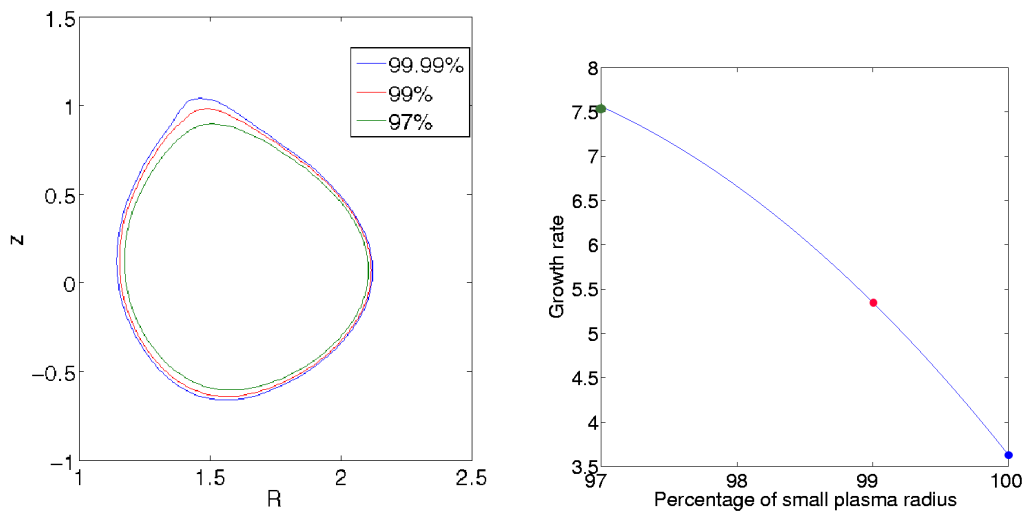


**Figure 3.5:** Left: Effective plasma boundary considering the skin effect (no change of total current). Right: Resulting growth rates for different plasma boundaries

currents. In the contrary, the frequencies are relatively small (about 30 Hz in this case), so that the currents are more localized in the inner part of the conductor. This can be taken into account by reducing the size of the PSL which enhances the self-inductance and reduces the coupling of the conductors to the plasma.

A third reason is the assumed resistance of the PSL. The value used here corresponds to the steady state (dc) resistance. The ac-resistance is increased above

---

this value by a factor dependent on the frequency, as the current flows only in a part of the conductor. With all these corrections, it is possible to "predict a posteriori" the growth rates, i.e. reproducing the growth rate with reasonable parameters. Nevertheless, the constraint to know the growth rate before calculating it is unsatisfying. That's why another approach is pursued that is independent of these corrections but covers the physics intrinsically. If doing so, the effort to take the non-linearity into account is relatively small which makes its inclusion obvious. This approach is described in the next sections.

### 3.3 Non-linear resistive MHD code

The results of the preceding section show that several aspects of the linear model lead to difficulties, which have a strong effect on the calculation of the growth rate and other figures of merit. It was shown that the existence of an X-point in the plasma has a severe impact, as well as the assumptions of surface currents on passive conductors. Furthermore, experimental data shows that the growth rate of an VDE is not constant during the time the instability grows (the growth rate in figure 3.3 varies during the VDE). The most logical step to solve these problems is the incorporation of resistivity in both plasma and passive structures and to take the non-linear behavior of the instability into account, which makes the solving of time evolution equations necessary. The MHD equations shown in section 2.1 for an axisymmetric configuration build the basis for the treatment of the problem. Two different approaches are followed for the treatment of the problem. The first one makes the Slip Motion ansatz as it is described in section 3.1. This restricts this code version to  $\beta = 0$  cases. The second approach takes the effect of finite pressure into account.

#### 3.3.1 Code version for $\beta = 0$

As mentioned above, the  $\beta = 0$  version of the code uses the Slip Motion ansatz. The condition for the plasma velocity (3.3) also could have been derived by making a straightforward ordering ansatz of the relevant quantities. The MHD equations are expanded in the inverse aspect ratio  $\epsilon = a/R$  with  $a$  the small and  $R$  the large plasma radius. Together with assumptions concerning density and pressure, the resulting set of equations is called "reduced MHD", as many terms of higher order in  $\epsilon$  can be neglected and a smaller number of equations has to be solved. For convenience, the MHD equations are repeated here:

$$\frac{\partial \rho}{\partial t} + \nabla \cdot \rho \mathbf{v} = 0 \quad (3.9)$$

$$\rho \frac{d\mathbf{v}}{dt} - \mathbf{J} \times \mathbf{B} + \nabla p = 0 \quad (3.10)$$

$$\rho \frac{\partial e}{\partial t} + \rho(\mathbf{v} \cdot \nabla) e + (\gamma - 1) \rho e \nabla \cdot \mathbf{v} + \nabla \mathbf{q} = \mathbf{J} \cdot \mathbf{E} + R_{\text{Rad}} \quad (3.11)$$

$$\mathbf{E} + \mathbf{v} \times \mathbf{B} = \frac{1}{\sigma} \mathbf{J} \quad (3.12)$$

$$\nabla \times \mathbf{E} = -\frac{\partial \mathbf{B}}{\partial t} \quad (3.13)$$

$$\nabla \times \mathbf{B} = \mu_0 \mathbf{J} \quad (3.14)$$

$$\nabla \cdot \mathbf{B} = 0 \quad (3.15)$$

$$(3.16)$$

And the Slip Motion ansatz for the velocity

$$\mathbf{v} = -R \cdot (\mathbf{e}_\phi \times \nabla \eta). \quad (3.17)$$

Due to the restriction to  $\beta = 0$ , no equation for the pressure (corresponding to the energy balance (3.11)) has to be solved.

When inserting the Slip Motion ansatz into the continuity equation [52],[51], it follows:

$$\frac{d(R^2 \rho)}{dt} = 0.$$

The continuity equation is trivially fulfilled for the quantity  $\tau = R^2 \rho$ , which is initially assumed constant in space. An inward shift of the plasma will lead to a higher density (which does not appear in the equations), as it is impossible to keep both toroidal magnetic field and density incompressible. It can be shown (see section A.4) that the Slip Motion ansatz with this assumption for the density eliminates all contributions of the toroidal magnetic field in the momentum equation (3.10).

Although this is not a realistic assumption for the density variation, it is not expected to influence the results in the regime of resistive wall modes, as there the inertial forces are not important.

The magnetic field is described by

$$\mathbf{B} = -\frac{1}{R} \mathbf{e}_\phi \times \nabla \Psi + \frac{R_0 B_{\phi,0}}{R},$$

where  $R_0$  and  $B_{\phi,0}$  denote the major radius of the magnetic axis and the value of the toroidal magnetic field on it, respectively. Equating the expressions for the current in Ohm's law (3.12)

$$\begin{pmatrix} J_R \\ J_\phi \\ J_z \end{pmatrix} = \frac{1}{\sigma} \begin{pmatrix} E_R + (\mathbf{v} \times \mathbf{B})_R \\ \frac{\partial A_\phi}{\partial t} + (\mathbf{v} \times \mathbf{B})_\phi \\ E_z + (\mathbf{v} \times \mathbf{B})_z \end{pmatrix} = \frac{1}{\sigma} \begin{pmatrix} 0 \\ \frac{1}{R} \frac{\partial \Psi}{\partial t} + (\mathbf{v} \times \mathbf{B})_\phi \\ 0 \end{pmatrix} \quad (3.18)$$

and Ampère's law (3.14)

$$\begin{pmatrix} J_R \\ J_\phi \\ J_z \end{pmatrix} = \begin{pmatrix} 0 \\ -\frac{1}{\mu_0 R} \left( \frac{\partial^2 \Psi}{\partial R^2} - \frac{1}{R} \frac{\partial \Psi}{\partial R} + \frac{\partial^2 \Psi}{\partial z^2} \right) \\ 0 \end{pmatrix} \quad (3.19)$$

leads to an equation that describes the time evolution of the poloidal magnetic flux  $\Psi$ :

$$\frac{\partial \Psi}{\partial t} + R \left( \frac{\partial \Psi}{\partial z} \frac{\partial \eta}{\partial R} - \frac{\partial \Psi}{\partial R} \frac{\partial \eta}{\partial z} \right) = \frac{1}{\mu_0 \sigma} \left( \frac{\partial^2 \Psi}{\partial R^2} - \frac{1}{R} \frac{\partial \Psi}{\partial R} + \frac{\partial^2 \Psi}{\partial z^2} \right) = \frac{1}{\mu_0 \sigma} \Delta^* \Psi \quad (3.20)$$

The right hand side of this equation shows the dissipative character of the system and is proportional to  $\sigma^{-1}$  (showing the difference to ideal MHD and the linear code). The higher the conductivity, the smaller is the dissipation. The conductivity treated as a surface quantity, its exact definition in the plasma is given in section 3.4.3. At the plasma boundary and in the vacuum region it is zero. The second term on the left hand side is the convective part, containing the plasma velocity  $v$  and describing the movement of the plasma. Using  $\Psi$  as evolving variable has the advantage that it is scalar and the poloidal magnetic field  $\mathbf{B}_p = -\frac{1}{R} \mathbf{e}_\phi \times \nabla \Psi$  is divergence-free.

The force balance (3.10) gives a further scalar equation when applying the operator  $R \cdot \mathbf{e}_\phi (\nabla \times)$  on it. One gets a time evolution equation for the vorticity

$$\Omega = R \mathbf{e}_\phi \cdot (\nabla \times \mathbf{v}) \quad (3.21)$$

which reads:

$$\frac{\partial \Omega}{\partial t} + v \nabla \Omega = \frac{R^4}{\tau} \left( \mathbf{B}_p \cdot \nabla \left( \frac{J_\phi}{R} \right) + 2 \frac{1}{R^2} J_\phi B_R \right) \quad (3.22)$$

where some non-obvious vector identities have been used (shown in section A.4). Note that in the case of an Grad-Shafranov equilibrium, the right hand side of equation 3.22 vanishes. Again, the left hand side contains a convective part, but there is no viscosity in this model.

For a given solution of  $\Omega$ , the stream function  $\eta$  (and with it the velocity  $\mathbf{v}$ ) is obtained as the solution of the Poisson problem in cylindrical coordinates after inserting the Slip Motion condition into (3.21):

$$\frac{\partial^2 \eta}{\partial R^2} + \frac{1}{R} \frac{\partial \eta}{\partial R} + \frac{\partial^2 \eta}{\partial z^2} = -\frac{\Omega}{R^2} \quad (3.23)$$

From 8 independent variables in the "standard" MHD model (three for the velocity, three for the magnetic field, pressure, and temperature) only two remain: the poloidal flux and the vorticity. So it remains to solve the equations (3.20) and (3.22) and to use Ampere's Law (3.19) and the relation (3.23) to obtain  $J_\phi$  (by differentiation) and  $\eta$  (by solution of the Poisson equation).

### 3.3.2 Extension to finite $\beta$

The model described in the preceding section is valid for only plasmas with  $\beta = 0$  as it used the Slip Motion Condition. The model is now extended to treat contributions from finite pressure. Under regular operating conditions of a tokamak the energy balance (3.11) is governed by heat conduction and heat sources. However, non-linear VDEs occur mostly in anomalous conditions where other effects (especially radiation losses) play a significant part, which can hardly be modeled. The experimental reality could be matched by prescribing the evolution of the plasma temperature profile (which is accessible with experimental means) via

$$p = 2 kT(\Psi, t) \frac{\rho}{m_i},$$

where  $T$  is the temperature,  $\rho$  the mass density and  $m_i$  the ion mass. As we are interested in instabilities growing on the relatively slow resistive time scale (small compared to sonic, heat conducting and Alfvén time scale) and due to the extremely high parallel heat conductivity (the parallel component is up to 10 orders of magnitude larger than the perpendicular component), the assumption of  $T = T(\Psi)$  is reasonable. For the test cases shown in this work an adiabatic law is used, as the exact choice of the temperature profile is considered to have only a weak influence on the results. As consequence of the constancy of  $p$  and  $T$  on flux surfaces, the density is a flux surface quantity as well.

The finite pressure leads to a modification of the vorticity equation (its derivation is shown in section A.4):

$$\frac{\partial \Omega}{\partial t} + R \left( \frac{\partial \Omega}{\partial z} \frac{\partial \eta}{\partial R} - \frac{\partial \Omega}{\partial R} \frac{\partial \eta}{\partial z} \right) = \frac{1}{\rho} \left( \mathbf{B} R^2 \nabla \left( \frac{J_\phi}{R} \right) - \frac{2FF' \partial \Psi}{R^2 \partial z} \right).$$

Note that in the limit of  $\beta = 0$ ,  $FF'/R$  is the total toroidal current density and the equation is the same as (3.22) but with different treatments of the density. Contrary to the  $\beta = 0$  case, the density  $\rho$  is a flux surface quantity and the above equation now depends on the pressure  $p$  and the function  $FF'$ , additionally to the  $\mathbf{J} \times \mathbf{B}$  terms that appear in both cases. The density at the beginning of the

simulation,  $\rho_0$ , is chosen to be similar to experimental values. However, as long as holds  $\rho = \rho(\Psi)$ , the exact density profile is not of high importance, as the cases of interest are considered to be independent of inertia. Nevertheless, to avoid singularities when dividing by  $\rho$ , the "vacuum" is assumed to have a density  $\rho_{vac}$  (but no pressure or conductivity) to which the plasma density connects smoothly.

To model the time evolution of  $\rho$ , mass conservation is used:

$$M(\Phi) = \int \rho(\Phi) \frac{dV(\Phi)}{d\Phi} d\Phi = const,$$

where  $V$  is the plasma volume inside a flux surface with  $\Psi = const$  and  $\Phi$  is the toroidal flux defined as the area integral

$$\Phi(\Psi) = \int_{A(\Psi)} \mathbf{B}_{tor} \cdot d\mathbf{A}.$$

The initial mass distribution  $M_0(\Phi)$  can be calculated with the given values for  $\rho$  and  $\frac{dV(\Phi)}{d\Phi}$ . Using the assumption that it doesn't change during time evolution, it follows that the density at the beginning and at every time step afterwards can be calculated via

$$\rho(\Phi) = \left( \frac{dV(\Phi)}{d\Phi} \right)^{-1} \cdot \frac{dM_0(\Phi)}{d\Phi}. \quad (3.24)$$

To calculate  $\frac{dV(\Phi)}{d\Phi}$  it is convenient to define an expression for the volume inside a contour determined by the poloidal flux:

$$V(\Psi) = 2\pi \int_{\Psi_0}^{\Psi} d\Psi \oint_{\Psi} \frac{dl_{pol}}{B_{pol}},$$

$$dV = V(\Psi + \Delta\Psi) - V(\Psi) = 2\pi d\Psi \oint_{\Psi} \frac{R dl_{pol}}{|\nabla\Psi|},$$

where  $dl_{pol}$  is a line element on a contour of  $\Psi$ . Hence, with

$$d\Phi(\Psi) = \int_{S_{\Phi+\delta S\Phi}} \mathbf{B}_{tor} \cdot d\mathbf{A} - \int_{S_{\Phi}} \mathbf{B}_{tor} \cdot d\mathbf{A} = d\psi \oint \frac{1}{|\nabla\Psi|} \frac{F}{R} dl_{pol}$$

and the chain rule

$$\frac{dV}{d\Phi} = \frac{dV}{d\Psi} \cdot \frac{d\Psi}{d\Phi}$$

the desired expression is found.

As mentioned above, an adiabatic law is used to describe the pressure. It states that the ratio  $\frac{p}{\rho^\gamma}$ , with  $\gamma$  denoting the adiabatic coefficient, does not change in time. Hence at all times, the ratio has to correspond to the ratio at the beginning:

$$\frac{p(\Phi, t)}{p_0(\Phi)} = \left( \frac{\rho(\Phi, t)}{\rho_0(\Phi)} \right)^\gamma. \quad (3.25)$$

The initial pressure profile  $p_0$  is given by the equilibrium and  $\rho_0$  can be fitted to experimental data. As (3.24) determines  $\rho(\Phi, t)$ , the time-dependent pressure can be calculated.

The last remaining expression necessary for the vorticity equation is  $FF'$ . As the net plasma motion damped by the resistive conductors evolves on a time scale slow compared to the Alfvénic and the sound time scale, it can be assumed that there is an equilibrium of forces due to pressure and  $\mathbf{J} \times B$  forces. Then,  $FF'$  can be calculated via the relation

$$R J_\phi = R^2 p' + FF'. \quad (3.26)$$

$R J_\phi$  is not constant on flux surfaces, hence a flux surface average is defined that reads:

$$\langle f \rangle = \oint_\Psi \frac{f dl}{|\nabla \Psi|} / \oint_\Psi \frac{dl}{|\nabla \Psi|},$$

where  $dl$  is a line element on a contour defined by the poloidal flux. For the calculation of the integrals, a contouring routine is implemented (A.2). Applying the average process on eq. 3.26 makes the quantities constant on flux surfaces and yields

$$FF'(\Psi) = \left( - \oint_\Psi \frac{R^2 p' dl}{|\nabla \Psi|} + \oint_\Psi \frac{R J_\phi dl}{|\nabla \Psi|} \right) / \oint_\Psi \frac{dl}{|\nabla \Psi|}$$

$p'$  is given at the beginning of the simulation and then calculated at every time step out of eq. (3.25) with

$$\frac{dp}{d\Psi} = \frac{dp}{d\Phi} \frac{d\Phi}{d\Psi}.$$

### 3.3.3 Normalization

As the quantities vary strongly in their magnitude, it is useful and convenient to normalize them. In absence of conductors, the vertical instability grows on the Alfvénic time scale

$$\tau_A = \frac{R_0}{v_a},$$

where  $R_0$  is a characteristic length of the system, usually the major radius of the magnetic axis, and  $v_a$  the (poloidal) Alfvén velocity which is defined as

$$v_A = \frac{B_0}{\sqrt{\mu_0 \rho_0}},$$

with  $\mu_0$  the vacuum permeability,  $\rho_0$  the plasma mass density at the magnetic axis and  $B_0$  a characteristic value for the poloidal field, e.g. at the last closed flux surface on the high-field side of the torus. These definitions lead to the normalization

$$\begin{aligned} t^* &= t/\tau_A \\ \mathbf{v}^* &= \mathbf{v}/v_A \end{aligned}$$

where the asterisk symbolizes the lack of dimension. After a straight forward normalization of the quantities and together with  $\sigma_0$ , the value for the plasma conductivity at the magnetic axis, equations (3.22) and (3.20) become dimensionless.

In the equation describing  $\Psi$ , the dimensionless Lundquist number  $S = \mu_0 \cdot \sigma_0 \cdot R_0 \cdot v_A$ , which is the ratio of resistive time to Alfvén time, is introduced.

$$\frac{\partial \Psi^*}{\partial t^*} + R^* \left( \frac{\partial \Psi^*}{\partial z^*} \frac{\partial \eta^*}{\partial R^*} - \frac{\partial \Psi^*}{\partial R^*} \frac{\partial \eta^*}{\partial z^*} \right) = \frac{1}{S \sigma^*} \left( \frac{\partial^2 \Psi^*}{\partial R^{*2}} - \frac{1}{R^*} \frac{\partial \Psi^*}{\partial R^*} + \frac{\partial^2 \Psi^*}{\partial z^{*2}} \right) \quad (3.27)$$

Typical fusion plasmas<sup>1</sup> have Lundquist numbers of the order  $10^8$  (often Lundquist numbers based on the toroidal rather than on the poloidal magnetic field are quoted which are typically one order of magnitude larger), whereas the code of this work operates because of reasons explained in section 3.4.4 in the regime of  $S \approx 10^4$ . Usually, equilibria of interest are stable if the conductors are ideally conducting. The growth rate of an instability is then determined exclusively by

---

<sup>1</sup> with a plasma current of about 1 MA, density  $\rho \approx 1 \cdot 10^{-7} \frac{kg}{m^3}$  and conductivity  $\sigma \approx 1 \cdot 10^8 (\Omega m)^{-1}$

the resistivity of the passive conductors and their geometric properties, but not by inertia, as outlined in section 2.4, and not by the plasma resistivity as shown in section 4.3.1. In this regime, the mismatch of  $S$  can be compensated. The instability evolves on the (normalized) resistive time scale on which the stabilizing currents decay:

$$\tau_w^* = \frac{L}{\mathcal{R}} / t_0$$

introduced in section 2.4, or, expressed as growth rate:

$$\gamma_w^* = \frac{\mathcal{R}}{L} \cdot t_0 = \frac{\mathcal{R}}{L} / \gamma_0. \quad (3.28)$$

The resistance and inductance are those of the PSL and can be calculated (see sections A.5 and 4.1.2 for details). Here,  $\gamma_0 = 1/t_0 = 1/t_A$  is defined slightly different than in the current filament model. For a circular plasma, the expressions can be transformed into each other, but the exact value is not important, as it cancels out when calculating growth rates in absolute units.

Inserting the expressions for resistance, inductance and  $\gamma_0$  into eq. (3.28) leads to

$$\gamma_w^* = \Gamma^* \frac{\sigma_0}{S \cdot \sigma_{PSL}},$$

where  $\Gamma^*$  is a dimensionless factor dependent only on the geometry of the conductors. If now the growth rate depends only on the decay of the induced currents, which is proportional to  $\gamma_w$ , the value of  $S$  is not important. Instead, for given instability drive and coupling to the passive structures, the product  $S \cdot \sigma_{PSL}^*$  determines the growth rate. As for the Lundquist number holds  $S \sim \frac{1}{\rho}$ , low values of  $S$  can be interpreted as enhanced plasma mass. That leads to a reduction of frequency and growth rates of modes on the Alfvénic time scale but does not influence the resistive wall modes.

### 3.4 Solving the system of equations

The set of equations cannot be solved analytically, hence a numerical method has to be used. As mentioned at the beginning of this chapter, the finite element method (FEM) is appropriate here for its good qualities concerning the inclusion of conducting structures of arbitrary shape and its mature status of development due to the broad applications in engineering problems. The basic mechanism of the FEM is described in the appendix, to which is referenced as well for the more detailed problems concerning the FEM. Essential for the FEM is the approxi-

mation of all quantities through (mostly) polynomial functions on a mesh. In this work, the mesh is irregular and constructed of triangles with an Delaunay algorithm [25]. Triangles are the best choice when modeling irregular boundaries and have some appealing qualities concerning the representation and integration of quantities. The elements are superparametric quadratic triangles of second order, i.e. the approximated quantities are represented by polynomials of second order on straight-edged triangles (6-node-triangles). In principle, it would also be possible to use curved (isoparametric) triangles without any change in the code (however, the passive structures appearing in the applications do not make this necessary). A picture of a typical mesh with about 6000 grid points is shown in fig. 3.6. The number of points is significantly reduced to show the mesh structure. The code runs typically with meshes that have at least about 50.000 grid points. In most of the applications shown here, the domain is rectangular and

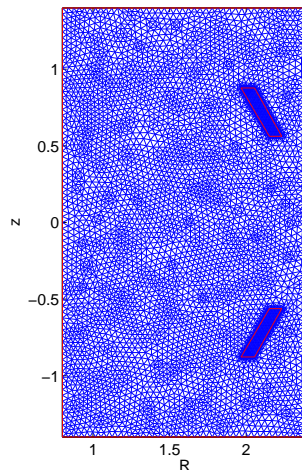


**Figure 3.6:** Typical mesh used for the calculations

includes two subdomains, the upper and the lower PSL. The size of the elements is quite homogeneous, except in the PSL, where the resolution is significantly increased because of a potentially thin current layer due to the skin effect and the subsidiary condition described in chapter 3.4.1 below. The discretization of the domain transforms the equations to matrix equations. The rank of the matrices is  $n_p$ , which is the number of grid points. The representation of the operators and quantities is described in detail in section A.1. Both evolution equations 3.20 and 3.22 have to be linearized. This is done by solving each of the equation at different stages of time. Starting with an initial solution for the poloidal flux distribution, both equations for poloidal flux and vorticity evolution are solved. Every  $n + \frac{1}{2}$  time step, the equation for  $\Psi$  is solved and the current density  $j$  and the magnetic field  $B$  is derivated from it. They are inserted in the right hand side

of the equation for  $\omega$ , which is solved every integer time step  $n$ . The velocity is calculated and inserted in the convective terms of both evolution equations. Figure 3.7 shows schematically the solution pattern which is called leap-frog scheme. This is an explicit time scheme, leading to a restriction concerning the maximum time step  $\Delta t$  (Courant-Friedrichs-Lewy-Condition, [50]) which is determined by the ratio of the element size to the velocity,  $\Delta t \approx \frac{\Delta x}{v_a}$ . While the coupling of both

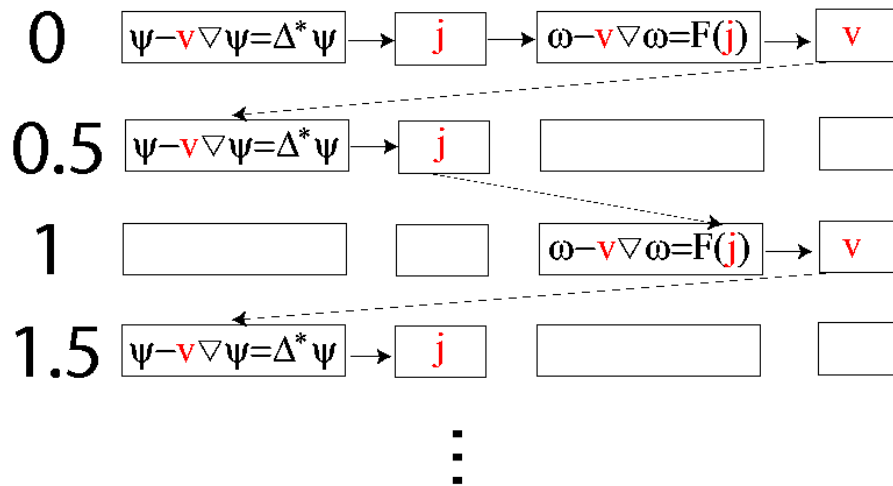


Figure 3.7: Leap frog scheme

equations is done explicitly, the equations themselves are solved implicitly. This requires to solve a matrix equation every time step, involving the current state of the system and the state of the next time step. This is more expensive than explicit methods, where in principle only a matrix-vector-multiplication has to be carried out. But as the time step restriction for the diffusion equation is proportional to the inverse of the conductivity,  $\Delta t \sim \frac{1}{\sigma}$ , and the vacuum is considered to be insulating (see section 3.4.3), the implicit method is chosen. Furthermore, it is easily possible to impose subsidiary conditions for the solution as the system of equations for each grid point is solved simultaneously. This advantage will be used in the code and is described later in this chapter. Another reason speaking against the explicit method is that it would require the inversion of the so-called "mass matrix" (see section A.1.4). In many problems, this has to be done once and afterwards, the simple matrix-vector-multiplication can be executed. As the mass matrix depends in this case on a time dependent variable (the equation for the time evolution of  $\Psi$  is multiplied by  $\sigma$  to avoid terms due to the partial integration of the second order operator, see A.1), this inversion would have to be done every time step. Even this would be possible with linear triangular elements, because the mass matrix can be *lumped*, leaving only nonzero entries on the main

diagonal. This is not the case for quadratic elements, where lumping leads to zero entries and makes an inversion impossible (this can be circumvented by choosing a different space for the finite element representation, that is "enriched" by a bubble function and dimensionally between quadratic and cubic elements [56]; nevertheless, this approach is not followed).

### 3.4.1 Passive Stabilizing Loops (PSL)

To model the connection of the both PSL legs, an potential difference  $\delta\phi$  is introduced that adds an electrostatic field to the electric field due to induction. This field ensures the equality of the currents in the upper and the lower leg as it leads to a compensating current. Inside the PSL, the equation describing the poloidal flux takes the form

$$\frac{\partial\Psi}{\partial t} - \delta\phi = \frac{1}{\sigma \cdot S} \Delta^* \Psi \quad (3.29)$$

with  $\delta\phi$  as new unknown variable. The current equality condition is implemented via the condition:

$$\oint_{PSL1} \mathbf{B}_p d\mathbf{l} + \oint_{PSL2} \mathbf{B}_p d\mathbf{l} = 0, \quad (3.30)$$

where the ring integrals are the integral form of Ampère's Law and encircle the upper and lower PSL, respectively, and the magnetic field is expressed via  $B_p = -\frac{1}{R} e_\phi \times \nabla \Psi$ . The gap in the PSL is treated as infinitely thin (to keep axisymmetry) and inductance and resistivity of the bridge are neglected. As the system is solved implicitly, the implementation of this constraint can easily be done by extending the system of equations by one row, as the solution for each grid point and the new variable  $\delta\phi$  are calculated simultaneously. The physical significance of  $\delta\phi$  is the gap voltage, which forms across the gap if for example net voltage is applied to the system (to maintain the plasma current against its finite resistivity in a quasi stationary state).

### 3.4.2 Boundary conditions

As the problem dealt with includes elliptic operators in space for  $\Psi$ , one has to specify boundary conditions for it on a curve enclosing the domain. The computational domain is given by the data of an equilibrium solver and includes the whole plasma, but not every coil that is necessary to generate the external

fields (see figure 3.8).

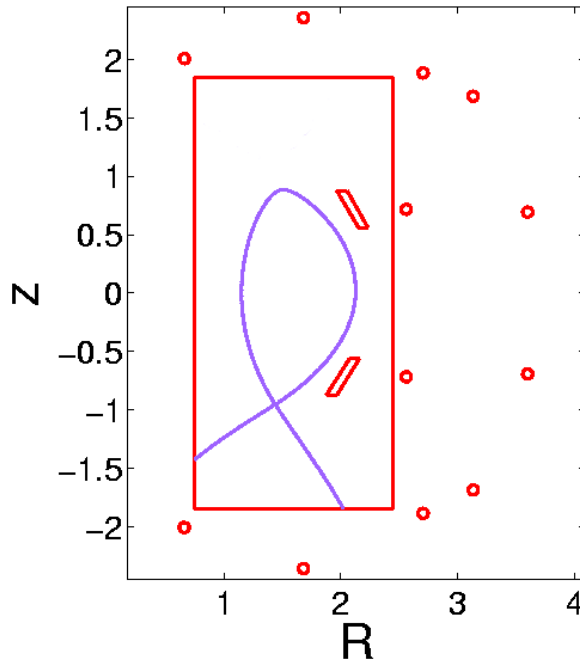


**Figure 3.8:** Computational domain and position of the external coils

The simplest kind of boundary conditions is of Dirichlet type, i.e. the solution of the problem has prescribed values on the boundary. If  $\Psi$  has prescribed time-independent values, the boundary, which does not include the PSL surface but only the border of the computational domain, behaves like an ideally conducting wall, as  $\frac{\partial \Psi}{\partial t} = \frac{\partial R \cdot A}{\partial t} = R \mathbf{E}_{\text{tangential}} = 0$ . No flux can penetrate the wall, so it has a stabilizing influence on the macroscopic motion of a plasma as mentioned in previous chapters. The stabilizing effect of the wall depends crucially on its distance to the plasma and is by far strongest for the  $m=1$  mode (i.e. in the axisymmetric case for a displacement of the plasma column) as a rigorous calculation of the energy contributions shows [9]. A way to treat the problem more realistically is to impose  $\Psi(R=0) = \Psi(R=\infty) = 0$  (as the absolute value of the poloidal flux has no meaning but only its derivatives, the choice of  $\Psi$  being zero at infinity is arbitrary but convenient). The stabilization is then achieved only by the PSL, but as the stabilizing effect of the real experimental wall is rather small due to its large distance to the plasma and the very short resistive time  $t_R = L/R$ , this treatment of the problem is much more realistic than using the ideal wall condition even when modeling the exact geometric wall of the device. As an ideal wall is strongly stabilizing, it would have to be placed far away from the plasma, but this approach is impracticable due to its huge calculation effort. So realistic results within reasonable computation times are possible only

with a boundary that allows unhampered flux penetration. Its implementation can be achieved with the help of Green's functions. Imagine two domains  $I$  and  $O$ , where  $I$  shall be totally included in  $O$  (see fig. 3.9) and  $\delta I$  (red) marks the boundary between them. Any current distribution  $\mathbf{J}_I$  in  $I$  will generate a

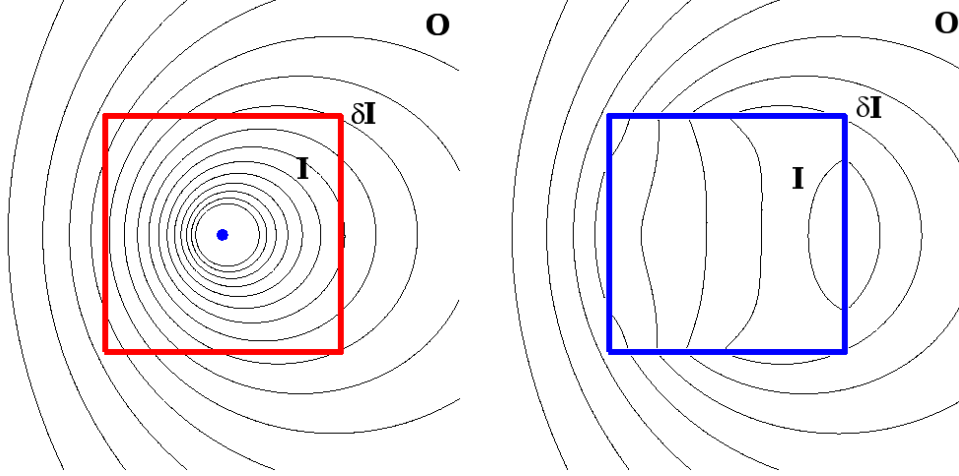


**Figure 3.9:** Different domains  $I, O$ , and  $\delta I$  and the poloidal flux  $\Psi$  for different current distributions (marked blue). *Left:* filament. *Right:* surface current.

magnetic field in  $I$  and  $O$ . In figure 3.9 on the left, this current distribution is a filament (blue dot), the shown isocontour lines belong to the associated poloidal flux. One can find a unique surface current distribution  $\sigma_{\delta I}$  on the boundary for which the associated magnetic field in  $O$  and on the boundary  $\delta I$  is exactly the same as if it was generated by the original current distribution  $\mathbf{J}_I$  [54]. This case is shown in figure 3.9 on the right. For the moment, it is assumed that this current distribution on the boundary  $\sigma_{\delta I}$  was known. Green's function for the Grad-Shafranov operator that relates the poloidal magnetic flux  $\Psi$  to the generating toroidal current reads [17],[8]

$$G(\mathbf{r}, \mathbf{r}') = -\frac{\mu_0 \sqrt{RR'}}{\pi k} \left[ \left(1 - \frac{k^2}{2}\right) K(k) - E(k) \right] \quad (3.31)$$

with  $K$  and  $E$  the complete elliptical integrals of first and second order and  $k$  defined as

$$k = \frac{4RR'}{(R+R')^2 + (z-z')^2},$$

with  $r$  and  $z$  the usual cylindrical coordinates and the prime denoting the source points. Following the method of Green's functions, multiplying the inhomogeneity (the surface current density) with  $G(\mathbf{r}, \mathbf{r}')$  and integrating over the domain

leads to the solution for  $\Psi$ , intrinsically using boundary conditions at infinity. As this calculation is only necessary to define boundary conditions, this solution is only needed on  $\delta I$ , hence:

$$\Psi(s) = \oint_{\delta I} G(s, s') \sigma_{\delta I}(s') ds' \quad (3.32)$$

with  $s$  a continuous coordinate on  $\delta I$ . The aim is to identify the region  $I$  with the computational domain that is used in the code and mentioned above. Then it is clear, that the boundary  $\delta I$  has no physical meaning and that there is not any real surface current on it. One needs the values of the magnetic flux on  $\delta I$  that would result, if there **were** a surface current equivalently to the current distribution in  $I$ . For matching to the "inner" solution,  $\Psi$  and the tangential magnetic field inside and outside  $I$  have to be continuous. The tangential magnetic field reads

$$B_{tan} = \mathbf{e}_t \cdot \left( -\frac{1}{R} \mathbf{e}_\phi \times \nabla \Psi \right) = -\frac{1}{R} \mathbf{e}_n \cdot \nabla \Psi = -\frac{1}{R} \mathbf{e}_n \cdot \oint_{\delta I} \nabla G(\mathbf{r}, s') \Big|_s \sigma_{\delta I}(s') ds',$$

with  $\mathbf{e}_t$  and  $\mathbf{e}_n$  the unit vectors in tangential and normal direction, respectively. If now the quantities are discretized, the integral equations turn into matrix equations. Hence, eq. (3.32) is written as

$$\Psi_i = G_{ik} \cdot \sigma_{k, \delta I}$$

and  $G$  can be inverted to get an discretized expression for the discretized surface current density  $\sigma_{k, \delta I}$ ,

$$\sigma_{k, \delta I} = G_{ik}^{-1} \Psi_i$$

which is inserted in the discretized equation for the tangential magnetic field:

$$-\frac{1}{R} \mathbf{e}_n \cdot \nabla \Psi \Big|_l = -\frac{1}{R} G_{lk}^* \sigma_{k, \delta I} = -\frac{1}{R} G_{lk}^* G_{ik}^{-1} \Psi_i$$

with the matrix  $G_{lk}^*$  as result of discretizing  $\mathbf{e}_n \cdot \oint_{\delta I} \nabla G(\mathbf{r}, s') \Big|_s$ . This condition links the values of  $\Psi$  on the boundary with its normal derivative, ensuring that the inner solution will satisfy the true boundary conditions at infinity. The formulation is similar to Robin boundary conditions, but while these are defined locally, here all values of  $\Psi$  on  $\delta I$  contribute to the value of the normal derivative.

As described above, the boundary condition applies only for currents inside the computational domain. As shown in figure 3.8, several currents are positioned beyond the computational domain, e.g. the currents in the shaping coils, but

their fields contribute to the magnetic flux distribution of the initial plasma. When applying the boundary condition, the "external" contributions to  $\Psi$  on the boundary must be subtracted, leading to

$$-\frac{1}{R} \mathbf{e}_n (\nabla \Psi - \nabla \Psi_{ext}) \Big|_l = -\frac{1}{R} G_{l,k}^* \sigma_{k,\delta I} = -\frac{1}{R} G_{lk}^* G_{ik}^{-1} (\Psi_i - \Psi_{ext}).$$

A further change of the boundary conditions is necessary if time changes in currents in external conductors are to be included. A practically important case is that of an applied loop voltage, necessary to keep the plasma current constant in spite of resistive dissipation, which is treated mathematically in section 3.4.4.

The condition applied in the code for the velocity stream function on the boundary (including the PSL boundary) reads  $\eta = 0$ . This leads to vanishing normal components of the velocity perpendicular to the boundary. The same condition is used for the vorticity  $\omega$ . Although this does not match the real conditions for the outer boundary, where no wall shall exist, the introduced error is small as long as the plasma is sufficiently far away from the border of the computational domain. This condition is met for all considerations made in this work.

### 3.4.3 Remarks on the conductivity $\sigma$ and the force term

Special attention is given to the conductivity. In the whole vacuum region  $\sigma$  is zero so that no currents exist there. Inside the plasma, it is treated as a flux quantity as it is a function of the temperature [10] for which holds  $T = T(\Psi)$  following the considerations made above. The initial conductivity profile is chosen to be consistent with the equilibrium current distribution, i.e. it is calculated as flux surface average  $\langle R J_\phi \rangle$ , leading to a profile  $\sigma(\Phi(\Psi))$ . In regions inside the separatrix where the toroidal flux increases beyond its initial value (e.g. caused by an increased plasma volume at the same position on the R-axis), the conductivity is zero as well; if the toroidal flux decreases, the conductivity profile is irreversibly cut off. This mechanism is illustrated in figure 3.10. The separatrix (in a case of a divertor plasma) is found by searching a saddle point in  $\Psi$ , as the absolute value of the poloidal magnetic field vanishes at the X-point. Having located the X-point and knowing the value of  $\Psi$  at this position, the separatrix can be identified by an tracing algorithm [58]. Inside the PSL, the conductivity is finite again. In ASDEX Upgrade, its value is that of copper, which means that the conductivity inside the PSL is about a third of the value at the center of a typical plasma. Of a more numerical interest is the treatment of the representation of  $\sigma$ . As there is a large, abrupt jump between the conductivity inside and outside the PSL, the question arises how to deal with the boundary nodes. Here,

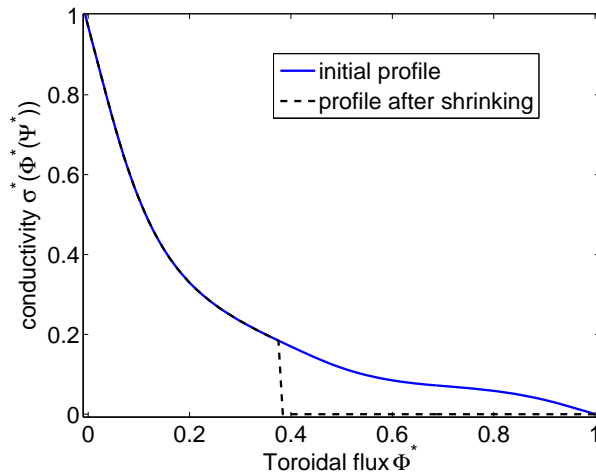


**Figure 3.10:** Exemplary initial conductivity profile (blue). If the toroidal flu decreases (e.g. by shrinking), the profile is cut off irreversibly.

the boundary nodes are associated with two values for  $\sigma$ : one, if the operation of interest happens inside the PSL, the other if operating outside. This is quite similar to the method of Discontinuous Galerkin with the difference, that  $\sigma$  is not a variable one is looking a solution for.

Another quantity that needs special treatment is the right hand side of the vorticity equation as it contains the expression  $\nabla \mathbf{J}_\phi$ . Usually, a derivative operation on a quantity results in the reduction of the order of representation and as the current density is essentially the second derivative of  $\Psi$ , it would be already a 0-th order representation (constant in an element). There exist schemes to construct derivatives of such given distributions (similar to those used in the finite volume method), but they lead to an inaccuracy one should be anxious to avoid. A better way, which is used in this work, is the method of patch recovery, where local least square fits are performed over several elements ("patch") after each derivation. Details can be found in section A.1.5. Figure 3.11 shows an comparison of the result of  $\Delta^* \Psi$  on a relatively coarse grid once using the "standard" procedure (left) and patch recovery (right).

### 3.4.4 Dissipation

Finite elements are advantageous when modeling irregular boundaries or structures and dealing with pure elliptic or parabolic problems. Convection-diffusion and convection equations can be cumbersome, if the convective part becomes too large compared to the ratio of finite element diameter to the time step (CFL criterion). The procedure gets unstable and the solution is polluted by non-physical

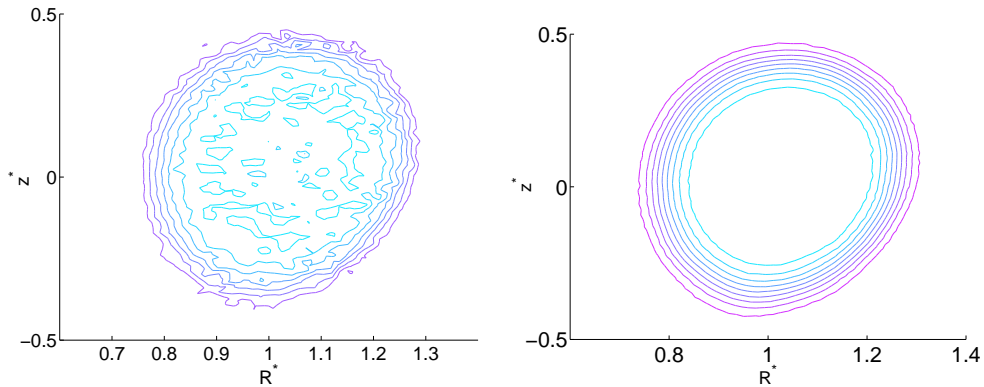


**Figure 3.11:** Result of  $\Delta^*\Psi$ . *Left:* "standard" procedure. *Right:* patch recovery.

oscillations. Various techniques have been proposed for the stabilization (e.g. exponential fitting, symmetrization, upwinding, least squares regularization, .. [55]). Those approaches are not followed here but could be added at a later point of time. Instead, it is ensured that the ratio of finite element diameter divided by the time step  $\Delta t$  to the velocities appearing is small enough to avoid those oscillations as described in section 3.4.

For all results and examples shown in this work, the Lundquist number  $S$  (proportional the inverse of the diffusion coefficient) used in the calculations never exceeds  $10^5$ . Together with the remaining normalization factors, that means a conductivity of the plasma of about  $10^3 - 10^4$ . As under these assumptions the dissipation of the plasma current can proceed on a faster time scale than the vertical instability, particularly when latter is strongly stabilized, the plasma current would decay significantly. The plasma would shrink and, due to the constancy of the external fields, move radially inward, making realistic statements about the growth rates impossible. To avoid the resistive decay of the plasma current a loop voltage simulating the action of the Ohmic transformer in the torus center is externally applied. The same mechanism is used in the experiment to control and maintain the current. The value of the loop voltage is, however, larger than in a realistic experiment due to the unrealistically small plasma conductivity. Because both dissipation and induction depend on  $\sigma$ , the current "refreshes" self-similarly, if the conductivity is chosen consistently with the initial current distribution, which is ensured by the procedure described in section 3.4.3. The time rate of change of flux (loop voltage) is prescribed as a further boundary condition (additional to the boundary condition described in section 3.4.2), its

value is given by the feedback condition

$$\ddot{\Psi}_{ind} = const. \cdot \dot{I}_{Plasma},$$

where dots denote temporal derivatives. The condition ensures that a stationary current results in a constant  $\dot{\Psi}$ , i.e. a constant loop voltage. The exact value of the constant is not important, as the system will converge to a value of  $\dot{\Psi}_{ind}$  that compensates exactly the loss of current. Because of the subsidiary condition for the PSL, they are unaffected by the change of flux.

# 4 Application and results

## 4.1 Testing and validation

The first step after the development of the code is to check if its results are physically reasonable. For the moment, only the general behavior of the code is examined based on relatively simple test cases (quantitative results are discussed in section 4.3). To minimize deviations from the well-understood current filament model, elliptical up-down-symmetric plasmas are used to show the basic phenomena. The degree of instability is varied by the ellipticity  $\kappa = b/a$  of the plasma where  $b$  and  $a$  are the major and minor axis of the ellipse, respectively. Figure 4.1 shows several plasma boundaries of equilibria that were created by successively increasing the currents in the shaping coils and with it the destabilizing force  $d_{curv}$  that acts on the plasma and is introduced in section 2.4. Another parameter that can be varied is the resistivity of the conducting structures around it, which determines the growth rates of potential instabilities. The plasma equilibria are calculated with the Garching Equilibrium Code ([42])

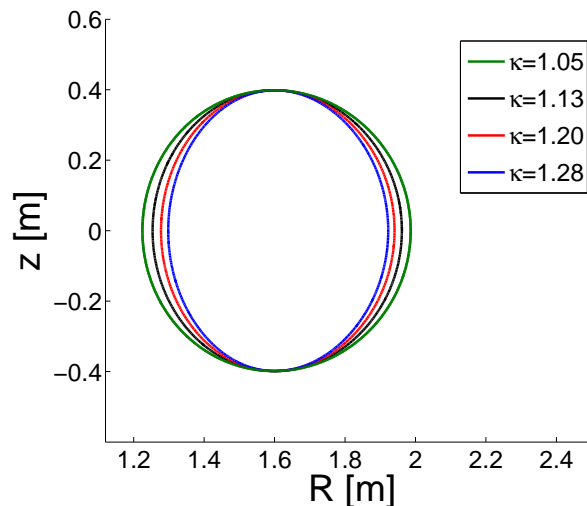


**Figure 4.1:** Degree of ellipticity

that gives the poloidal flux function in dependence on the desired plasma shape,

current,  $\beta_p$ , position of the magnetic axis and the current and pressure profiles. The currents in the poloidal field coils (see fig. 2.11) are adjusted by an iterative procedure to create a plasma governed by the Grad-Shafranov equation.

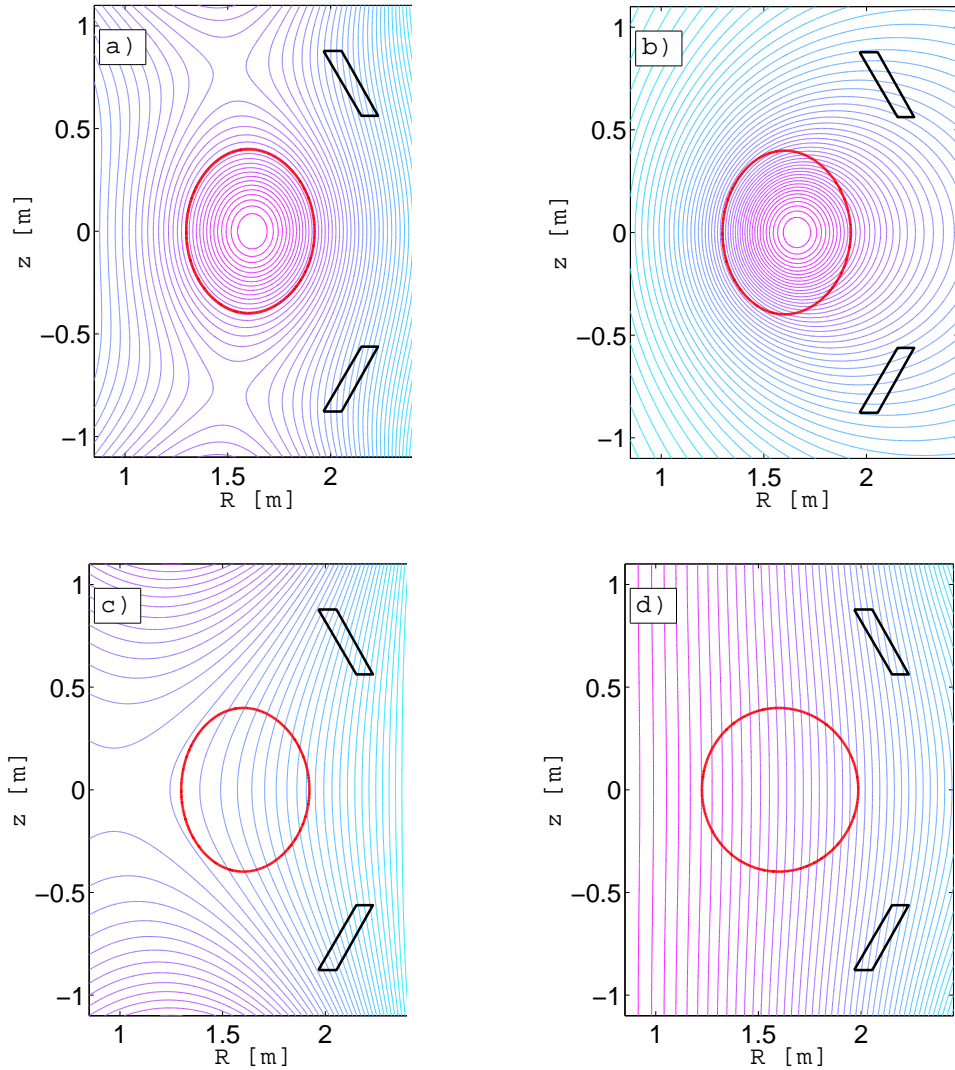


**Figure 4.2:** Poloidal fluxes for an equilibrium with  $\beta_p=0$  and  $l_i \approx 1$ .  
a) Total flux for ( $\kappa=1.33$ ) b)  $\Psi$  due to plasma current for  $\kappa=1.33$  c)  
 $\Psi$  due to external currents for  $\kappa=1.33$  d)  $\Psi$  due to external currents  
for  $\kappa=1.09$

Figure 4.2 a) shows  $\Psi$  contours of an example equilibrium which has like all the other equilibria in this section  $\beta_p=0$ , its magnetic axis at  $R = 1.62 \text{ m}$ ,  $z = 0 \text{ m}$  and a virtual limiter at  $z = 0.4 \text{ m}$  that determines the plasma boundary (highlighted in red). The plasma current is  $I_p = 1.2 \text{ MA}$ . Outside the plasma region, the conductivity is zero as described in section 3.4.3 except in the PSL,

where its value can be varied. The position of the PSL is almost identical to their position in ASDEX Upgrade, however, they are up-down symmetric as well in order to minimize sources of potential deviations from the simple model. Their boundaries are marked with black lines. Figure 4.2 b) shows the poloidal flux that is generated only by the plasma current. This figure also demonstrates the effect that leads to the hoop force: the magnetic pressure on the inside is larger than on the outside of the plasma torus (dense poloidal flux contours mean a stronger magnetic field). Figure 4.2 c) shows the contributions to the flux of the external conductors for the equilibrium with  $\kappa = 1.28$ . In contrast to figure d), which shows the contribution of the external conductors for the case with  $\kappa = 1.08$ , there is a strong destabilizing component  $d_{curv} \sim \frac{\partial B_R}{\partial z}$ .

### 4.1.1 Vertical movement

At first, the case with the highest ellipticity ( $\kappa = 1.28$ ) and without any stabilizing conductors (nor a conducting wall nor PSL) is discussed. As the plasma shape differs significantly from a circular form, a quite strong instability is expected. Figure 4.3 shows the position of current barycenter  $z_c^*$  in dependence on the time and the position of the plasma boundary at the beginning of the calculation and at  $t^* = 7$ . The coordinates of the current barycenter are calculated via

$$(z_c - z_0)I = \oint_{\partial\Omega} \mu_0^{-1} \left( -R \log \frac{R}{R_0} B_n + (z - z_0) B_s \right) ds, \quad (4.1)$$

$$(R_c^2 - R_0^2)I = \oint_{\partial\Omega} \mu_0^{-1} (2R(z - z_0)B_n + (R^2 - R_0^2)B_s) ds, \quad (4.2)$$

where quantities with index 0 refer to an in principle arbitrary reference point, which in the following is chosen as the equilibrium position. Quantities with index  $c$  to the position of the barycenter.  $R$  and  $z$  are the midpoints of line elements  $ds$  which lie on a curve enclosing the whole plasma (but no other currents like those in the PSL for the case with conductors, see [40]).  $B_n$  and  $B_s$  are the magnetic field components which are perpendicular and tangential to  $ds$ .

As expected, the  $z$  position shows an exponential behavior,

$$(z_c^*(t^*) - z_0^*) = z_a^* \cdot e^{\gamma^*(t^*)}, \quad (4.3)$$

where  $z_0^*$  denotes the equilibrium position (in these examples  $z_0^* = 0$ ) and  $z_a^*$  is a small but non-zero initial displacement from the equilibrium. Due to the up-down-symmetry of the equilibrium, it is impossible to predict whether the

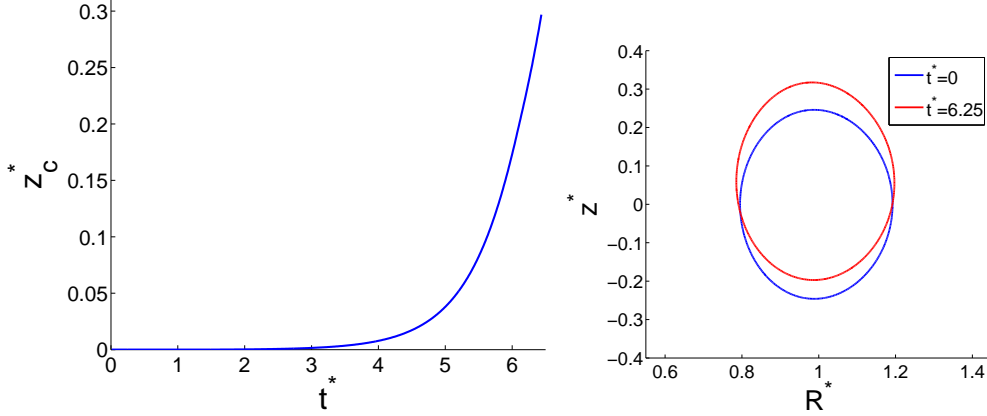


**Figure 4.3:** *Left:* Z position of the magnetic axis vs. time (note that the instability proceeds on Alfvénic time scale). *Right:* Plasma boundary at the beginning and at  $t^* = 7$ .

instability grows upwards or downwards. The initial perturbation here results from the asymmetry of the finite element mesh. For convenience, all shown z-positions of the plasma are positive. The linear growth rate is obtained by taking the logarithm of eq. (4.3), leading to

$$\ln(z_c^*(t^*)) = \log(z_a^*) + \gamma^*(t^*). \quad (4.4)$$

If  $z_0^*$  is not zero at the beginning, another method described in section 4.4 is used. Figure 4.4 shows the logarithm of  $z_c^*$  for three cases with different elongations ( $z_0^* = 0$ ).

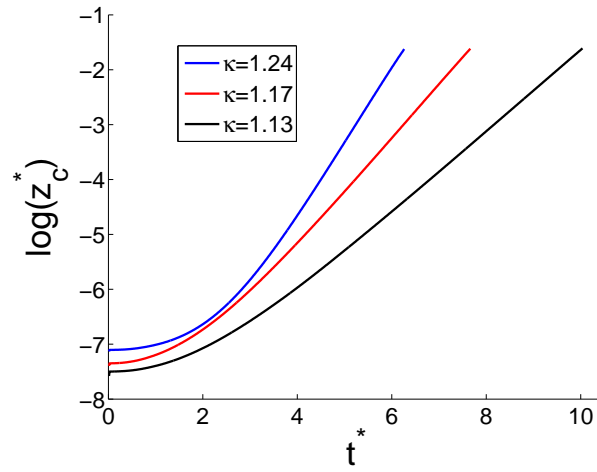
The phase of linear growth begins after short time (about two time units normalized to Alfvén times after the most unstable mode has manifested) and ends approximately at  $z_c^* = 0.1$  for these cases.

Figure 4.5 shows isocontours of the stream function  $\eta$  for an undamped axisymmetric instability.

## 4.1.2 Passive conductors

### 1. Slowed growth

The most important quality of the passive conductors is that they slow down the growth of an instability. Figure 4.6 shows an example of a plasma which would be stabilized by ideal conductors. It shows the z-position of



**Figure 4.4:** Logarithm of the  $z$  position for three different elongations. Blue:  $\kappa = 1.24$ , red:  $\kappa = 1.17$ , black:  $\kappa = 1.13$

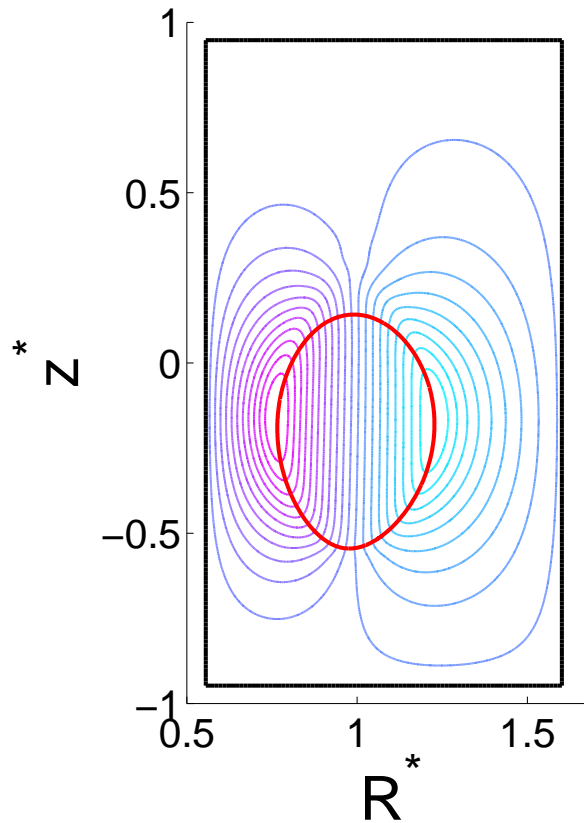


**Figure 4.5:** Stream function  $\eta$  for an undamped axisymmetric instability.

the current barycenter for the case of no conductors (blue line) and resistive PSL (red line). A detailed examination of their influence on growth rates

is done in section 4.3.

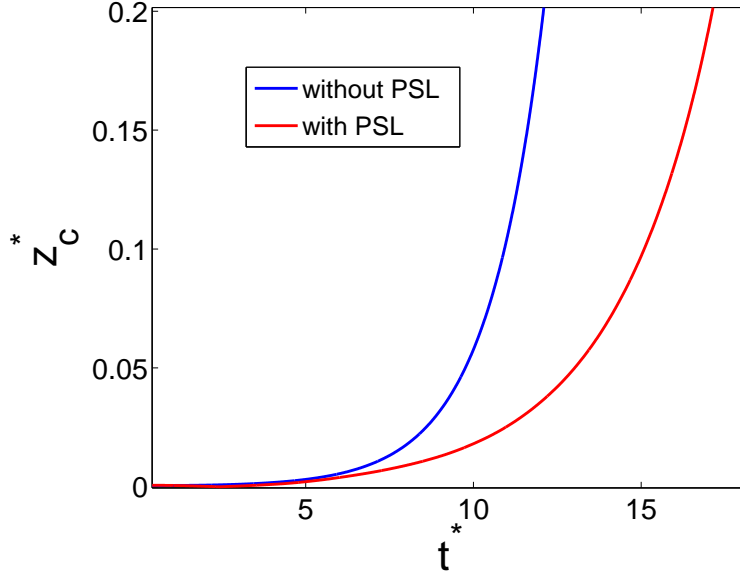


**Figure 4.6:** Effect of conductors on the growth rate.

## 2. Equality of currents

The test cases with elliptical equilibria are also suitable to examine the behavior of the PSL. The most simple and obvious test is to check whether the currents in the upper and lower PSL are equal but of opposite sign. Figure 4.7 shows that this condition is fulfilled exactly. It shows the PSL currents versus time for the case with  $\kappa = 1.28$  and  $\sigma_{PSL} = 0.01$ , but the condition holds for any case. As the equality is enforced via an additional equation, the perfect match is not surprising. As the currents are always the same in amount, in the further work only the positive current is shown. Figure 4.7 also shows that the current grows exponentially similar to the vertical position of the plasma.

## 3. Compensating voltage $\delta\phi$

Due to the coupling of the PSL, there should be no currents due to symmetric changes of the flux, i.e. a change of flux  $\frac{d\Psi}{dt}$  at the upper PSL does not lead to a current induction inside of it, if the same change of flux occurs at the lower PSL, because the currents would have the same toroidal direction and cancel each other as described in section 3.4.1. Symmetric changes of the flux can occur for homogeneous dissipation of the plasma or a radial movement. A vertical movement will result in an asymmetric change and leads to opposed currents in the PSL. Figure 4.8 shows the values of the poloidal flux versus time at two points close to the inner side of the upper

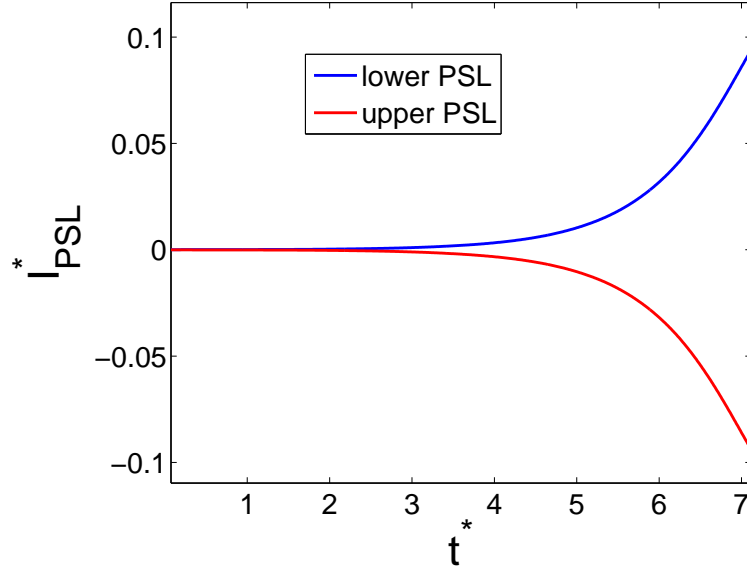


**Figure 4.7:** Currents in the upper (red) and lower (blue) PSL.

and lower PSL, respectively. At both points,  $\Psi$  decreases monotonically

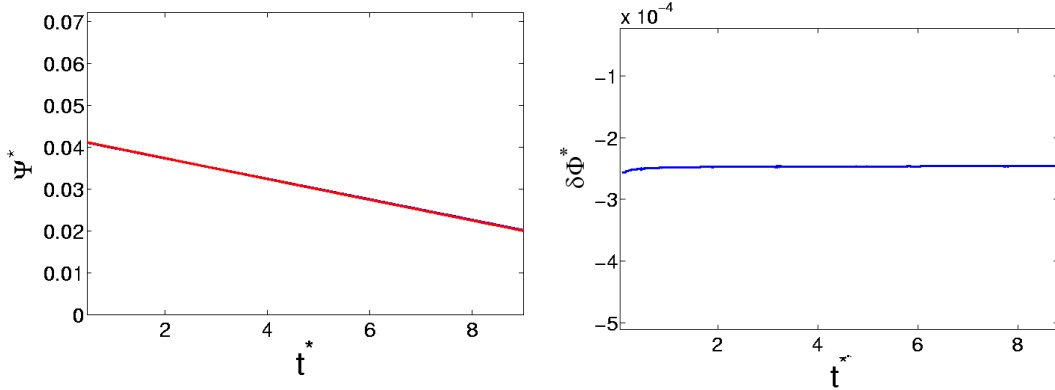


**Figure 4.8:** Left:  $\frac{\partial \Psi}{\partial t^*}$  for upper (red) and lower (blue) PSL Right:  $\delta \phi$

due the compensating flux that maintains the plasma current (as the decrease is symmetric, the lines are almost indistinguishable). No current exists in the PSL. Equation 3.29 states, that the change of flux in time must be compensated by the voltage  $\delta \phi$  to guarantee equality of currents. Indeed,  $\frac{\partial \Psi^*}{\partial t^*} \approx -2.4 \cdot 10^{-4}$  equals the value for  $\delta \phi$  as shown in figure 4.8. If now, for the same parameters, movement is allowed and the typical vertical displacement occurs, a different situation can be observed. The left picture in figure 4.9 shows the change of flux at both PSL less the flux due to ohmic heating discussed in the figure above. In this way, only the

asymmetric change of flux is considered. While the divergence of  $\Psi$  at

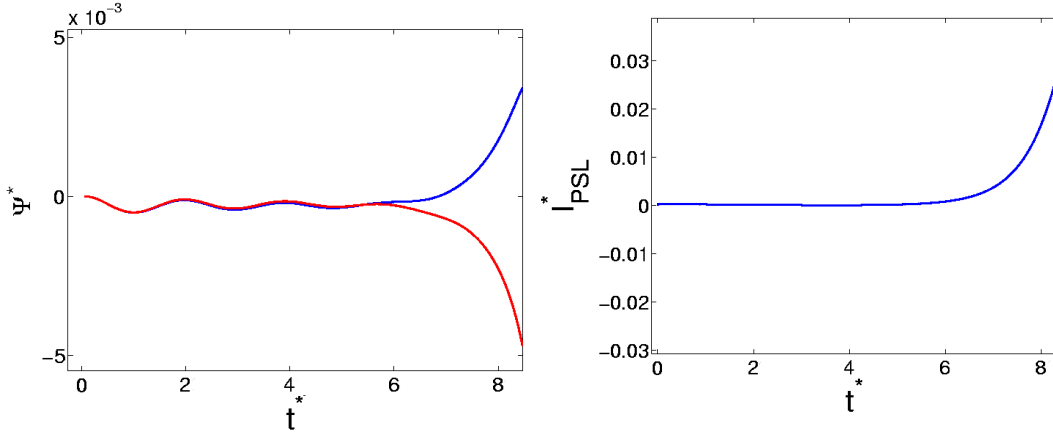


**Figure 4.9:** Left:  $\frac{\partial \Psi}{\partial t}$  for upper (red) and lower (blue) PSL Right:  $\delta \phi$

the end of the curve leads to the expected current increase (right picture in the same figure), the oscillation at its beginning is not reflected. The reason is that the oscillation of the flux reflects a radial oscillation of the plasma position. It is a relatively small, damped movement because the finite resolution of the mesh doesn't resolve exactly the initial equilibrium. The radial position of the plasma center and the voltage  $\delta \phi$  are depicted in figure 4.10. As can be seen, the change of flux due to radial movements is caught by  $\delta \phi$ . A purely vertical rigid shift leads to  $\delta \phi = 0$ .

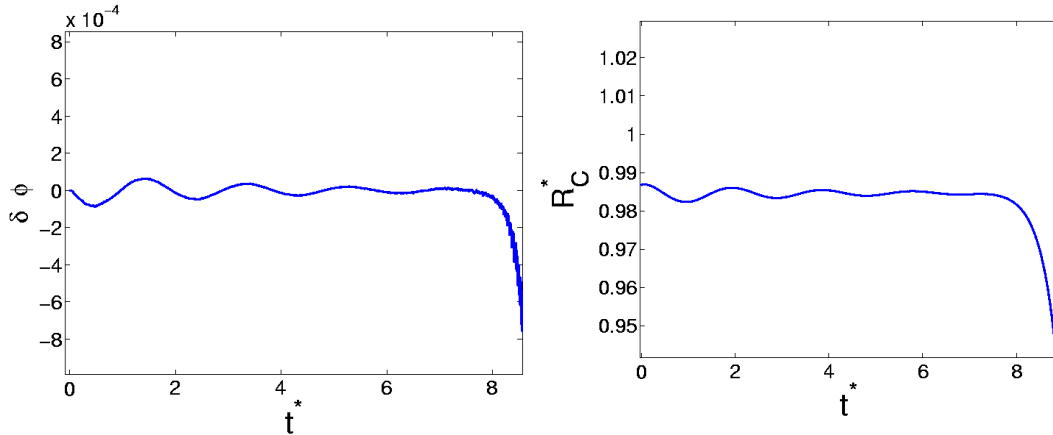


**Figure 4.10:** Left:  $\delta \phi$  Right: Radial position  $R_c$  of the plasma barycenter

#### 4. Skin effect

As the PSL have a finite extension, it is expected that the current distribution inside differs from homogeneity for high growth rates and conductivities, according to eq.(2.34) and described in section 3.2. This is one effect suspected to lead to differences between experimentally observed and computed growth rates, particularly close to the limit of marginal stabilization by infinitely conducting PSL. It can be illustrated when comparing the current distributions in the PSL for two cases with different  $d_{curv}$ , i.e. different degrees of instability, but with similar growth rates and at the same plasma position. In both cases, the total PSL current is roughly the same, but their conductivity differs by a factor of 100.

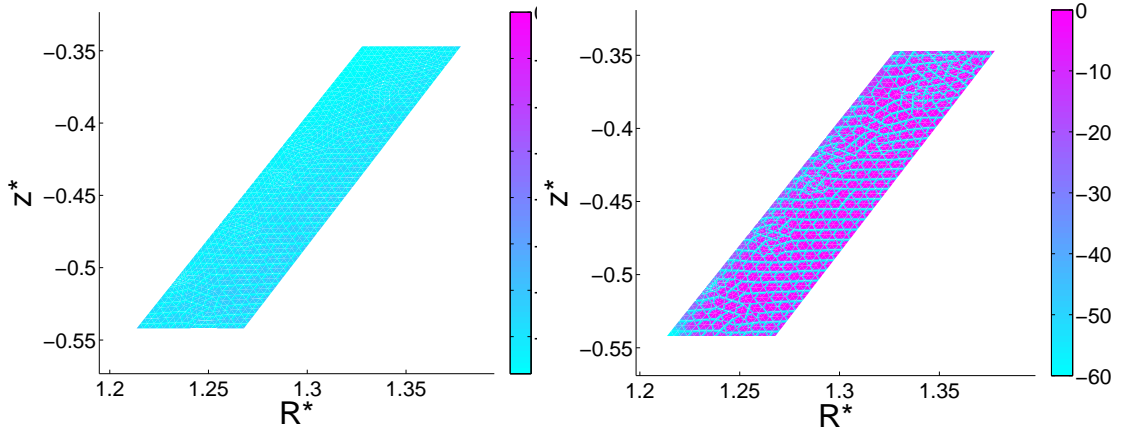


**Figure 4.11:** *Left:* low PSL conductivity *Right:* high PSL conductivity

As expected, in the case of high conductivity, the current flows in a thin layer, whereas it is almost homogeneous if the conductivity is low. This can be quantified by calculating the effective internal inductance  $l_i$  (which was defined for the plasma in section 2.3) of the PSL. For an circular wire with infinite aspect ratio,  $l_i$  is zero, when the current flows only on the boundary,  $l_i=0.5$  for a flat current distribution and it's higher for peaked current profiles. The PSL are not circular and have no infinite aspect ratio leading to deviations from the known model, that can be calculated with Green's function for toroidal currents (see 3.4.2). A surface current leads then to a value of  $l_i \approx 0.16$  and a flat current distribution to  $l_i \approx 0.65$ .

Figure 4.12 shows the internal inductances against the vertical displacement  $z_c^*$ . The first values of  $z_c^*$  are omitted, because small oscillations in the first phase of the motion including zero-crossings in the PSL current lead to extremely high values for the internal inductance. The dashed lines show the inductance for the PSL, the plasma moves towards, the solid lines

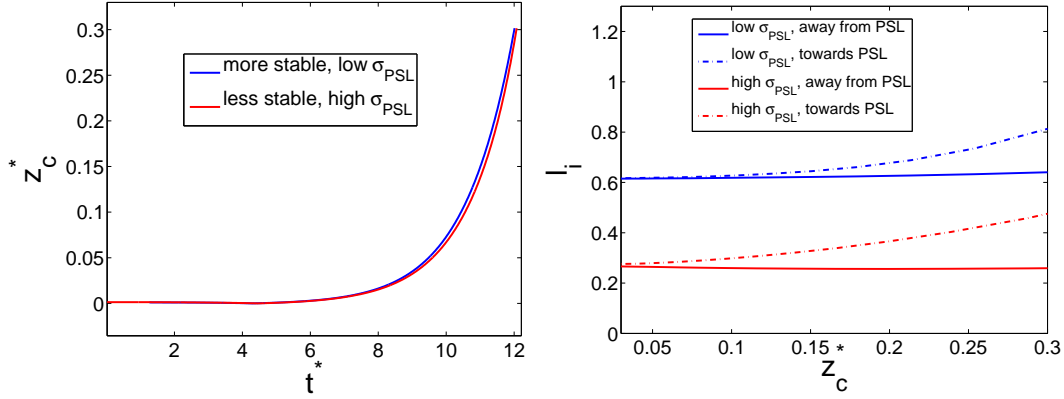


**Figure 4.12:** *Left:*  $z$ -position of the current barycenter for a relatively stable case with low conductivity in the PSL and a relatively unstable case with high conductivity in the PSL. The growth rates are almost the same. *Right:* Effective internal inductance inside the PSL. Solid lines belong to the PSL from which the plasma moves away, dashed lines to the other.

those for the PSL from which the plasma moves away. The latter remain approximately constant during the displacement, while the former increases. That occurs because the plasma "overtakes" the PSL partly and a current of opposed direction is induced to hold the plasma back, whereas the current direction in the other PSL stays the same. Note that the plasma motion is followed deep into the non-linear regime, where the growth rate cannot be considered as constant anymore. For the case of low conductivity and flat current distribution (blue lines), the value of  $li = 0.65$  is matched very well for both PSL after a small displacement. The case with high conductivity exhibits a deviation from the value of 0.16, because the current layer is neither homogeneously distributed on the surface nor infinitely thin. It's worth mentioning, that even if the internal inductance for the "towards"-PSL in this case reaches a value of about 0.5, it does not mean that the current distribution gets flat. Instead, the current begins to peak on the surface and it is impossible to draw conclusions on the exact contributions.

## 5. Current decay time of the conductors

The nominal current decay time  $L/R$  can be calculated using the equations (A.21) and (A.22) in section A.5 or determined "experimentally" by the code when the initial poloidal flux corresponds to homogeneous currents in the PSL as it is shown in figure 4.13 on the left.  $\Psi$  can be calculated with Green's function introduced in section 3.4.2. The currents are equal but of opposite direction, so no compensating currents to enforce this condition

are necessary and  $\delta\phi$  is zero. The right picture shows the value of the

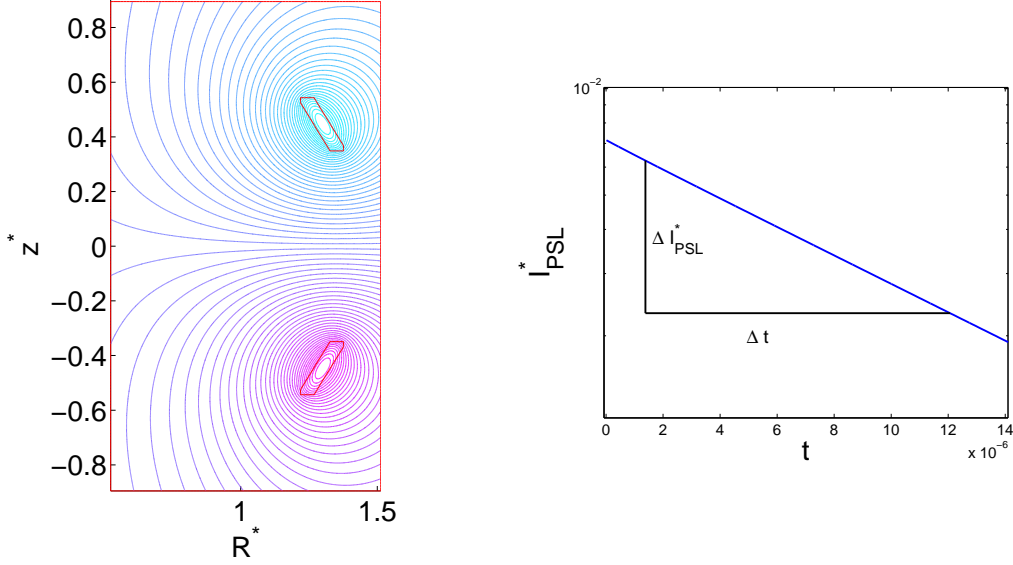


**Figure 4.13:** *Left:*  $\Psi$  distribution for test  $R_c$  *Right:* Current decay in the PSL, resistive time  $L/R$

normalized current in the PSL (logarithmic scale) versus time in seconds for a resistance  $\mathcal{R} = 0.96\Omega$ . The decay time can be determined by measuring the time it takes until the current reaches  $1/e$  of its initial value  $I_0$ , as the decay law reads

$$I(t) = I_0 \cdot e^{-\frac{t}{L/\mathcal{R}}}.$$

Alternatively, the slope of the curve can be calculated. The result of the analytical calculation is  $L_a \approx 1.3 \cdot 10^{-5}H$ , the code yields  $L_c = 1.296 \cdot 10^{-5}H$ . This value agrees with the specifications written down in the technical documentation of ASDEX Upgrade [24].

### 4.1.3 Plasma pressure

Until now, only equilibria with  $\beta = 0$  were used for the calculations. Before dealing with the effects of finite pressure, a comparison of the results of both code versions (the first one with the Slip Motion ansatz, the second without it) is done. Figure 4.14 shows the motion of the current barycenters for two different ellipticities calculated with both code versions. The first case is very unstable and the growth is inertia dominated whereas the second one is stable with ideal conductors and evolves on the resistive time scale. Both cases have the same mass but different density profiles. Picture a) corresponds to the first case and

shows the growth versus time. The dependence on the density profile is obvious. Picture b) shows that if the growth depends exclusively on the resistivity of the conductors and not on inertia both code versions yield the same result. This situation corresponds to the one we are interested in our practical applications.

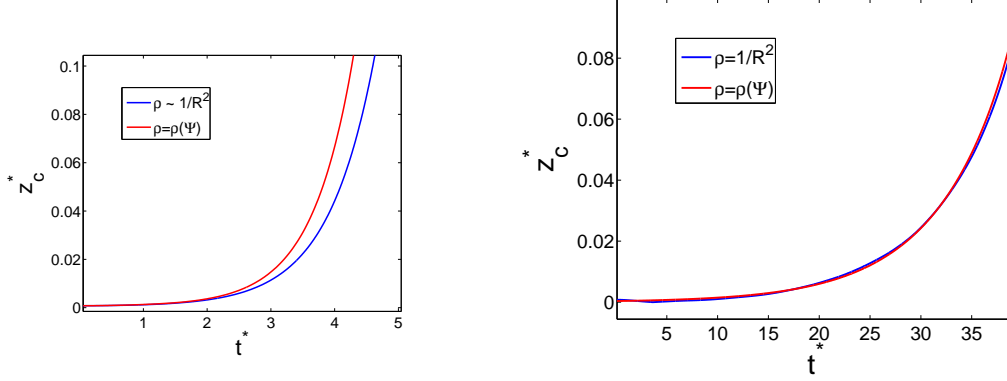


**Figure 4.14:** *Left:* Growth for an unstable plasma. The blue curve is the result of the code version with the Slip Motion condition ( $\rho = 1/R^2$ ), the red curve is the result of the other code version with  $\rho = \rho(\psi)$ . *Right:* Stabilized plasma with growth on the resistive time scale.

Now a set of three equilibria (stable for ideal conductors) with different values for  $\beta$  ( $\beta=0, 0.5$  and  $1.0$ ) is generated. All other characteristics like ellipticity, total current and so on are kept constant (to obtain plasmas with the same ellipticity but different values for  $\beta$ , the external currents to generate an equilibrium must be adjusted). Figure 4.15 shows radial cross sections at  $z = 0$  for the normalized poloidal flux  $\hat{\Psi}$  (left picture) and the function  $R \cdot J_\phi$ . With increasing plasma pressure both magnetic axis and current barycenter are shifted outwards.

As the current barycenter is closer to the PSL for higher  $\beta$ -values, the better inductive coupling leads to decreased growth rates for such cases as figure 4.16 shows for the case of  $\gamma_w = 0.1$ .

Figure 4.17 shows some typical profiles of the  $\beta = 0.5$  case, figure 4.18 shows the evolution of volume, density and total mass for the same case.

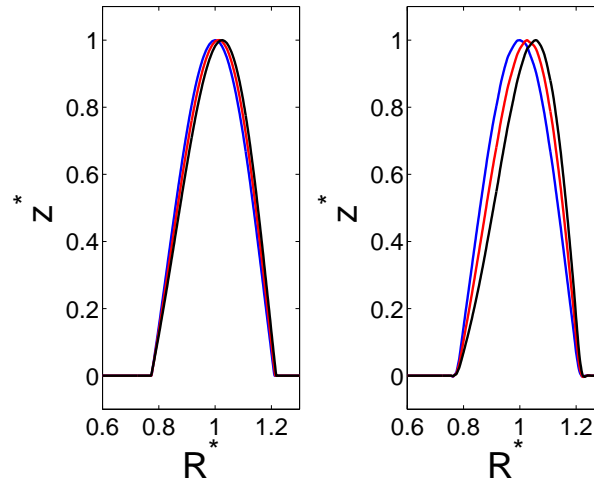


**Figure 4.15:** a) Cross section of the normalized poloidal flux  $\hat{\Psi}$  for an elliptical plasma along the  $z=0$  axis. The blue line corresponds to  $\beta = 0$ , red to  $\beta = 0.5$ , and black to  $\beta = 1$ . b) Profiles for the function  $R \cdot J_\phi$  with the same color code.

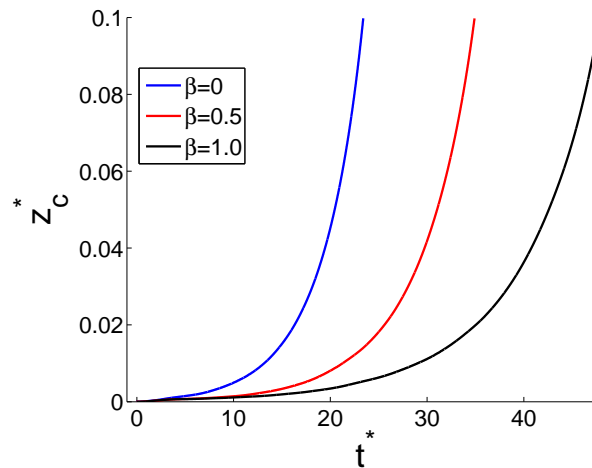


**Figure 4.16:**  $z$ -position of the current barycenter for  $\beta = 0$ ,  $\beta = 0.5$  and  $\beta = 1$ .

## 4.2 Effect of boundary conditions

The influence of the boundary conditions is now examined. First of all, the stabilizing effect of an ideally conducting wall boundary condition is demonstrated. Figure 4.19 shows an elliptical plasma with  $\kappa = 1.2$  and  $\beta = 0$ . Calculations are done with different positions of the computational boundaries. The configuration with the more distant boundary is called grid A, the other grid B. On the right, the current barycenter of the plasma versus time is shown. The blue line (almost

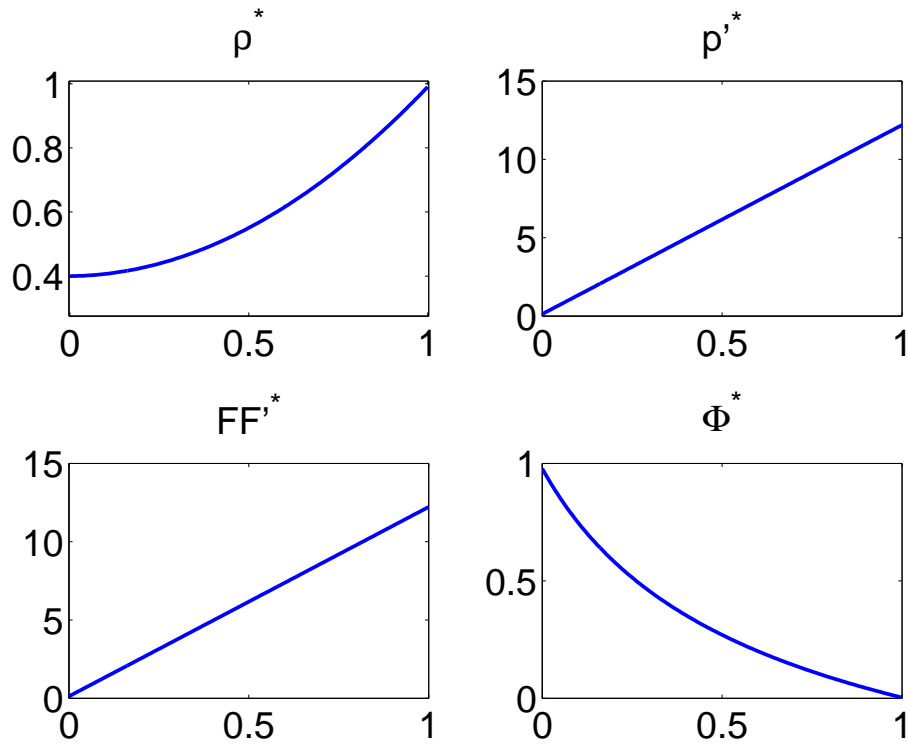


**Figure 4.17:** Normalized values for density  $\rho$ ,  $p'(\Psi)$ ,  $FF'(\Psi)$ , and the toroidal flux  $\Phi(\Psi)$  versus normalized poloidal flux  $\hat{\Psi}$  for an equilibrium with  $\beta=0.5$ .

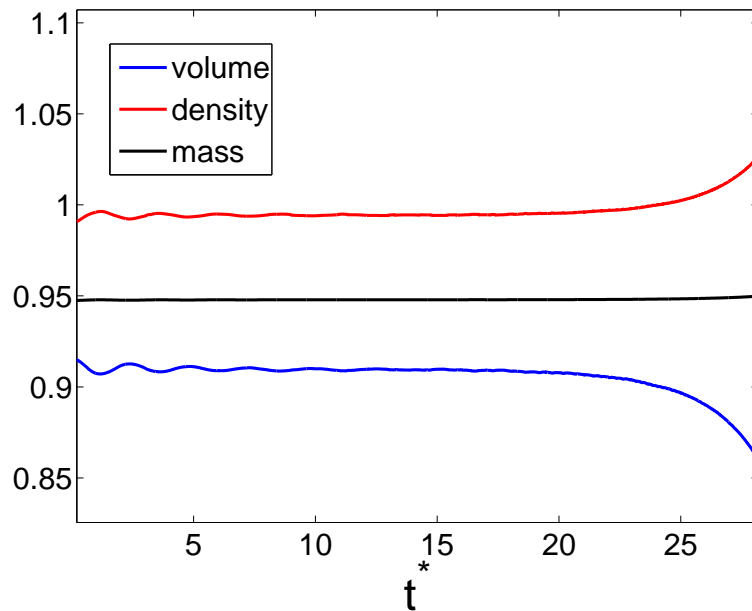


**Figure 4.18:** Normalized volume, density and mass versus time.

completely covered by the green line) shows the growth with the implemented condition  $\Psi(R = \infty) = 0$  on grid A. The red and black lines show the growth in presence of a more distant and a closer ideal wall, respectively. The stabilizing effect (the growth rate for the configuration with an ideal wall on grid A corresponds approximately to a configuration without ideal wall but with PSL and  $\gamma^* = 0.05$ ) and the dependence on the distance is clearly seen. The green line corresponds to the same condition as the blue one, but on grid B. Obviously, the position of the computational domain is not important for the calculation of the growth rates, as they show almost identical behavior.

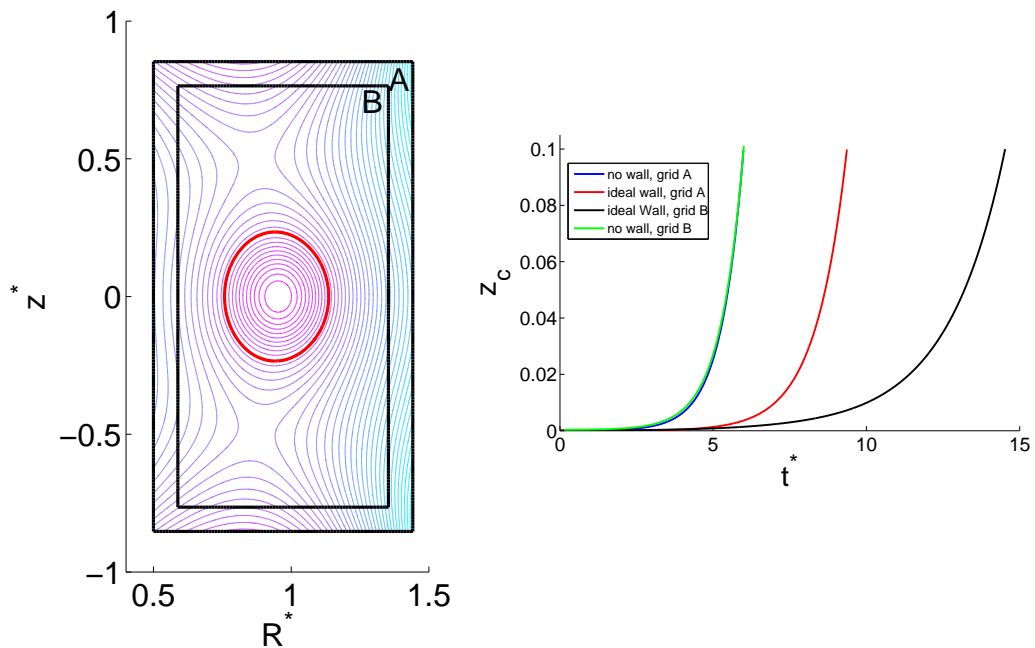


**Figure 4.19:** *Left:*  $\Psi$  contours of an elliptical equilibrium. The red line denotes the plasma boundary. The black lines mark the computational boundaries for the larger grid A and the smaller grid B. *Right:*  $z$ -position of the current barycenters for the case of Dirichlet boundary condition corresponding to an ideal wall on grid A (red) and ideal wall on grid B (black), and no wall boundary condition (like described in section 3.4.2) on grid A and grid B (green), respectively. The result for the blue and green cases are indistinguishable on the scale of this plot.

As the wall geometry is not modeled appropriately and the stabilizing influence in experiments is considered to be small on the present ASDEX Upgrade as described in section 3.4.2, the choice of magnetically permeable walls is indicated. Independent of the choice of boundary conditions, an spatially constant external flux is impressed at the computational boundary, whose time variation simulates the effect of an applied loop voltage as described in 3.4.2. Figure 4.20 shows the evolution of the plasma current of an ideally stable plasma equilibrium for the

case with (blue) and without (red) applied loop voltage to maintain the current. In the absence of an applied loop voltage, the current decreases monotonically.

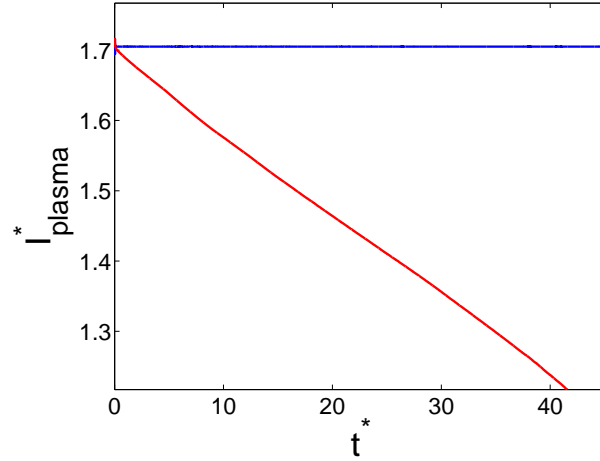


**Figure 4.20:** Plasma current with (blue) and without (red) applied loop voltage.

As a consequence, the lower current leads to an inward shift (shown in figure 4.21), as the currents in the external shaping coils do not change. Due to the greater distance between plasma current and passive conductors, the inductive coupling decreases, leading to axisymmetric instability (at a later stage).

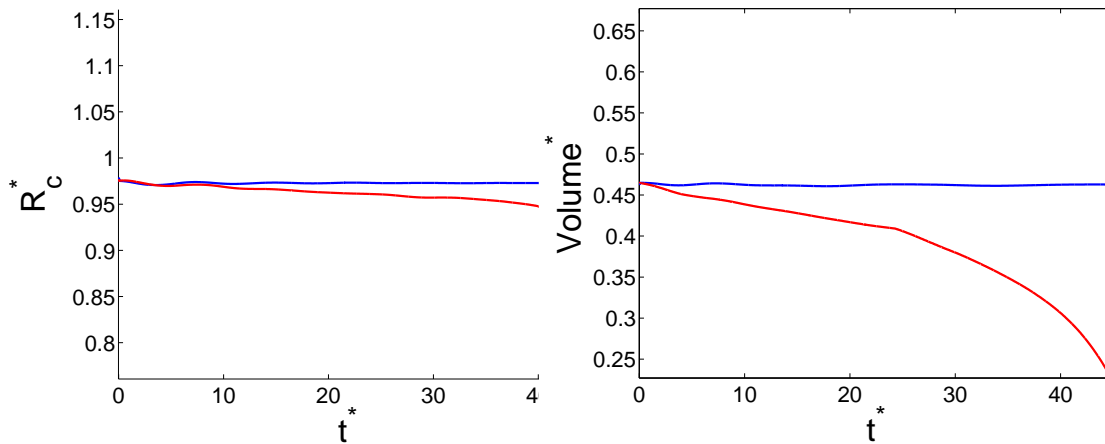


**Figure 4.21:** Left: Radial position of the current barycenter  $R_c$  Right: Plasma volume

That additionally to the total current the current profile remains the same despite the applied voltage is shown in figure 4.22 (the reason is the choice of the conductivity profile described in section 3.4.3). A cut at the  $z = 0$  axis in radial

direction shows the current density profile ( $\beta = 0$ ) at the beginning (blue) and after 40 Alfvén times (red).

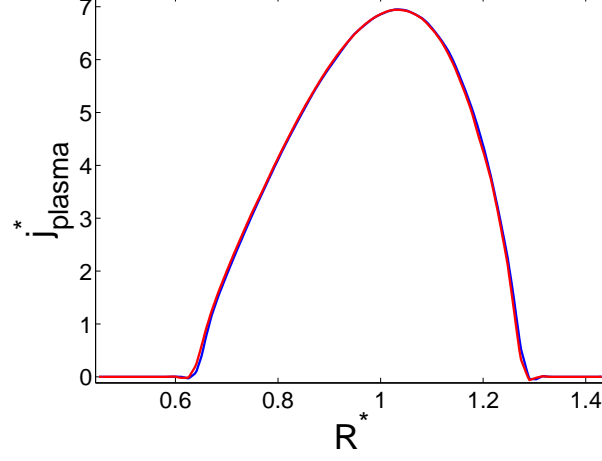


**Figure 4.22:** Current profile, cut at  $z = 0$  for  $t^* = 0$  (blue) and  $t^* = 40$  (red).

### 4.3 Comparison with current filament model

After the testing procedures of the last chapter that served to show the qualitative behavior of the code, the focus is now on concrete results. Therefore, growth rates are calculated and compared to the results of the current filament model. For this an experimental situation is chosen for which a good qualitative approximation of the filament model is expected. To determine parameters appearing in the filament model, full simulations with our model are carried out, using only the linear stage of the development, and the equivalent values are calculated.

As first parameter, the effective value of the normalized destabilizing force  $d_{curv}$  is determined for each configuration of the set of elongated plasma presented in the last chapter. For the moment, it is assumed that no stabilizing conductors exist that influence the growth of the instability. The movement is then governed by inertia and  $\gamma_w^*$  in eq. (2.32) can be treated as infinite.  $d_{curv}$  can then be calculated for each case via

$$\gamma_{undamped}^{*2} + s_{cond} \cdot \frac{\gamma_{undamped}^*}{\gamma_{undamped}^* + \gamma_w^*} - d_{curv} \Rightarrow \gamma_{undamped}^{*2} = d_{curv} \quad (4.5)$$

where the growth rates are determined by the like described in the preceding section. The blue curve in 4.23 shows the expected increase of  $d_{curv}$  with the

elongation  $\kappa$ . It can be seen that for the aspect ratio and the current distribution

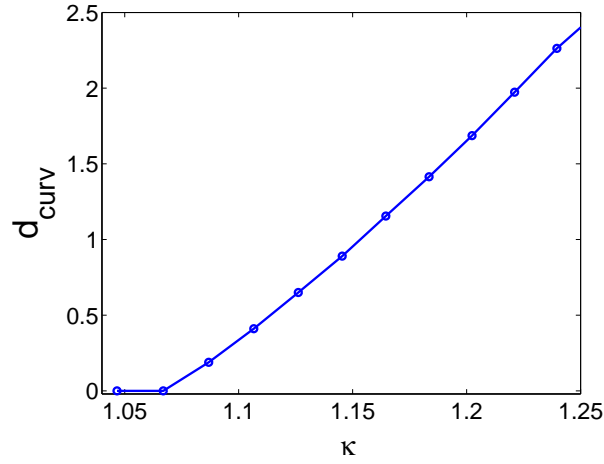


**Figure 4.23:** Normalized destabilizing force  $d_{curv}$  versus ellipticity  $\kappa$

used a plasma with an ellipticity smaller than about  $\kappa = 1.07$  is stable even in the absence of conducting structures. This agrees with former results (e.g. [44],[13]) and is caused by the stabilizing effect toroidicity has on vertical stability.

Now, the effect of resistive conductors is included. When the conductivity is very high (ideal conductor), the plasma is stable until  $d_{curv}$  is larger than  $s_{cond}$ . Beyond that point, the plasma is unstable despite the ideal conductors and the resulting instability is inertia dominated. The calculated growth rates  $\gamma_{damped}^*$  are shown in figure 4.24.

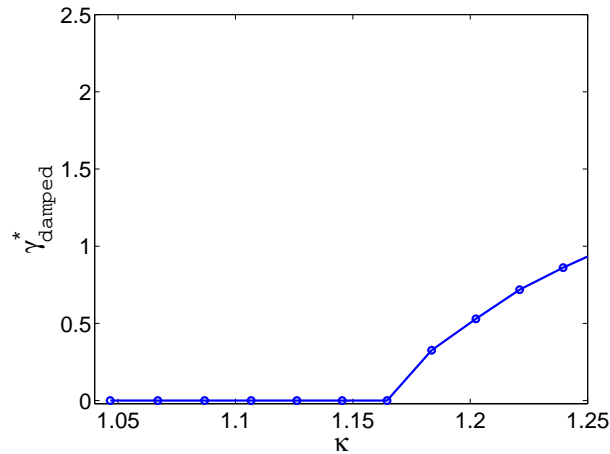


**Figure 4.24:** Normalized growth rate  $\gamma_{damped}^*$  versus ellipticity  $\kappa$

For high conductivities  $\gamma_w^* = \frac{R/L}{\gamma_0}$  is very small compared to the growth rate

$\gamma_{damped}^*$  and hence

$$\gamma_{damped}^{*2} + s_{cond} \cdot \frac{\gamma_{damped}^*}{\gamma_{damped}^* + \gamma_w^*} - d_{curv} = 0 \Rightarrow \gamma_{damped}^{*2} = d_{curv} - s_{cond} \quad (4.6)$$

As  $d_{curv}$  is known from the analysis without conductors,  $s_{cond}$  can be calculated from eq. (4.6). Figure 4.25 shows the resulting values for  $s_{cond}$ . In the current filament model, it is expected that  $s_{cond}$  is constant for all configurations, as the position of the conductors is fixed and deviations in mass and mutual inductance for the equilibrium configurations are considered to be negligible. Figure 4.25 shows that  $s_{cond}$  is not completely constant, but decreases towards lower values of  $\kappa$ . The reason behind this is that the plasma has, contrary to a filament, an extension and its movement is not restricted to a rigid vertical shift. As stated in section 3.1, the movement has a radial component as well that causes a movement away from the conductors and hence lowering their stabilizing influence. The closer the configuration is to marginal stability (no restoring or enhancing forces as reaction on a displacement), the stronger is the deviation from the rigid shift towards a radial curving. A more detailed examination of these effects follow in section 4.4.

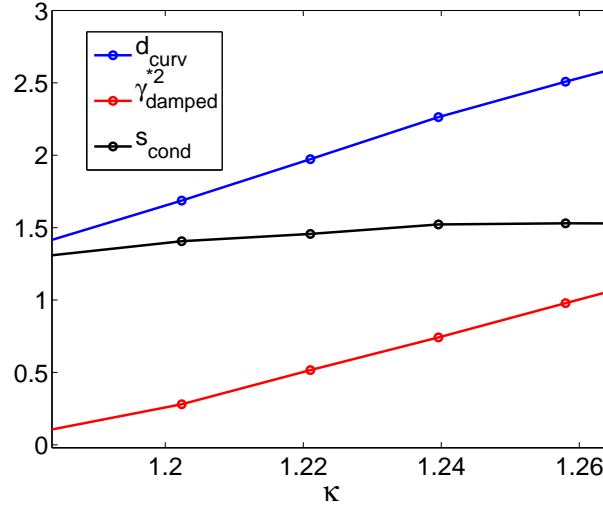


**Figure 4.25:**  $d_{curv}$  and  $s_{cond}$

The knowledge of  $s_{cond}$  and  $d_{curv}$  allow for the reconstruction of figure 2.13 in chapter 2.4. The parameter  $\gamma_w^* = \frac{R}{L}/\gamma_0$  is varied by changing the value of the PSL conductivity  $\sigma_{PSL}$ , leading to different values for their resistivity  $\mathcal{R}$ . The normalized growth rates against the ratio  $d_{curv}/s_{cond}$  and  $\gamma_w^*$  as parameter is shown in figure 4.26.

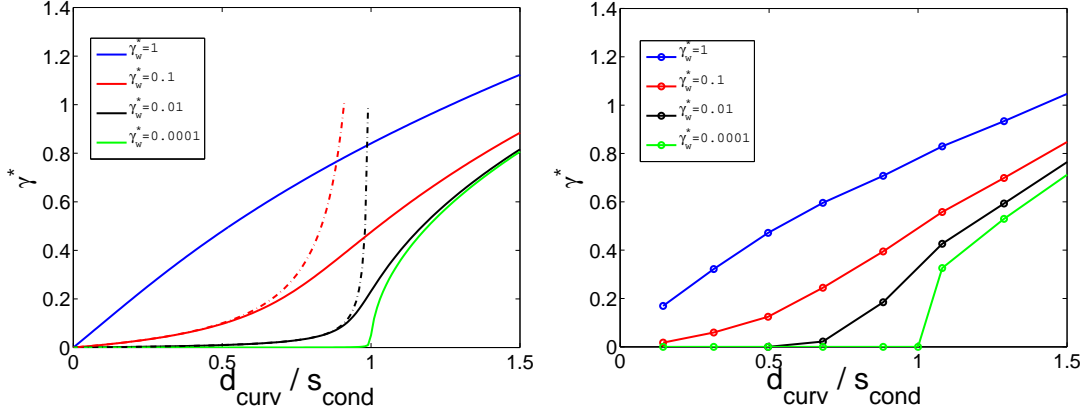


**Figure 4.26:** Analytical (left) and numerical (right) growth rates with  $\gamma_w$  as parameter.

$s_{cond}$  is assumed to be constant, because it is known only for the cases of ideally unstable plasmas. In this representation, this leads to small deviations in the normalized growth rates compared to the analytical model. Nevertheless, the code results can be fitted very well to the expected values. Note that for the purpose of comparison the growth rates are determined in a region where they can be treated as linear growth rates.

### 4.3.1 Resistive growth

To distinguish resistance and inertia dominated regimes, the growth rates for the case  $\frac{d_{curv}}{s_{cond}} = 0.5$  in dependence on the PSL conductivity  $\sigma_{PSL}^*$  are examined. This corresponds to a vertical cut in figure 4.26. The analytical prediction and the numerical result is shown in figure 4.27 on the left. Until  $\gamma_w \approx 0.1$  the growth rate increases linearly with the resistance of the passive conductors which is typical for resistive wall modes. The value of  $\gamma_w$  until which this linear relation holds is dependent on the value of  $\frac{d_{curv}}{s_{cond}}$ : the more unstable a configuration is, the smaller is this limiting value of  $\gamma_w$ .

The right picture in the figure shows the  $z$ -positions of the current barycenter for increasing values of  $\sigma_{PSL}$ . The time on the abscissa is normalized to the resistive time  $t_R = L/R$  of each case. This leads to an universal curve for the growth of vertical instabilities if it is determined only by the resistance of the passive conductors.

This behavior is reflected as well when plotting the currents in the PSL versus the  $z$ -position of the plasma as shown in figure 4.28. In the regime of resistive

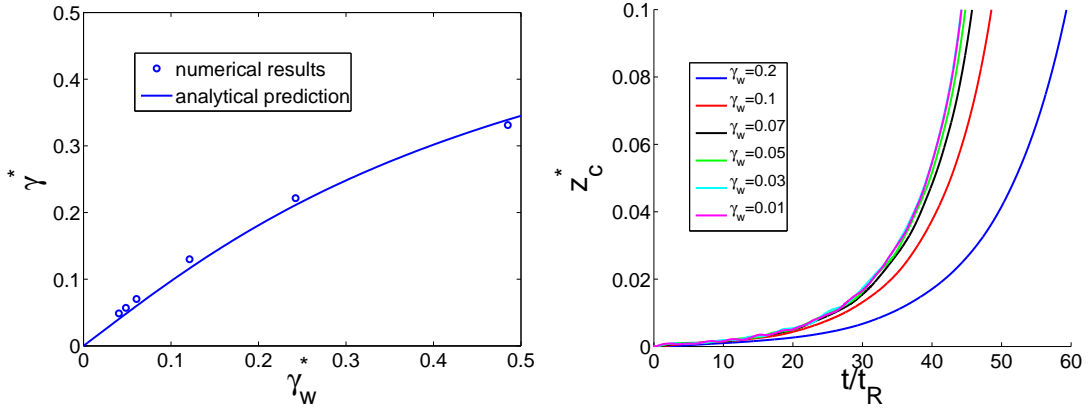


**Figure 4.27:** Left: analytical predictions and numerical results for the normalized growth rates  $\gamma^*$  versus the normalized resistive growth rate  $\gamma_w^*$ . Right: z position of the current barycenter for different values of  $\gamma_w$  normalized to the resistive decay time  $t_0/t_R$ .

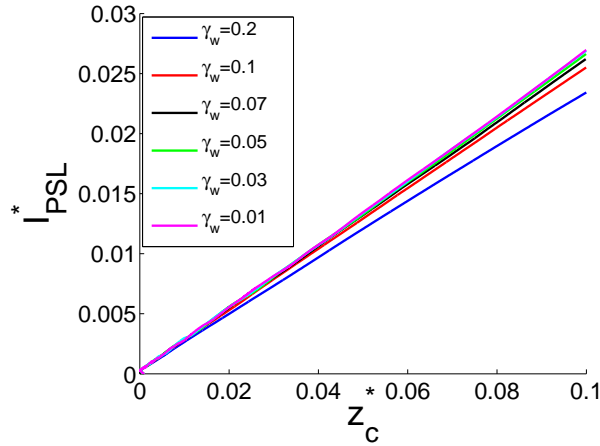


**Figure 4.28:** Current in the passive conductors versus z position of the plasma current barycenter

growth, the currents in the PSL depend only on the position of the plasma.

It remains to show that the growth rates does not depend on the value of S but on the value of  $\gamma_w \sim \frac{1}{S \sigma_{PSL}^*}$  as outlined in section 3.3.3. Figure 4.29 shows the time evolution of the plasma current barycenter for three cases which have all  $\gamma_w = 0.1$ . The red line corresponds to the reference case with  $S_{ref} \approx 3000$  and  $\sigma_{PSL,ref}^* = 0.825$ . The blue line has its value for S decreased by a factor of five, whereas the conductivity in the PSL is increased by the same factor. These parameters are reversed for the black line. The resulting growth rates are the same.

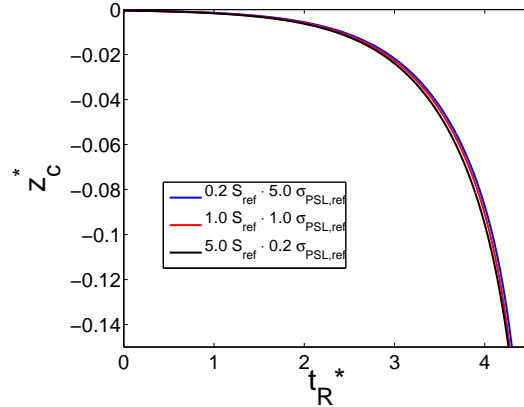


**Figure 4.29:** Current barycenter of the plasma versus time

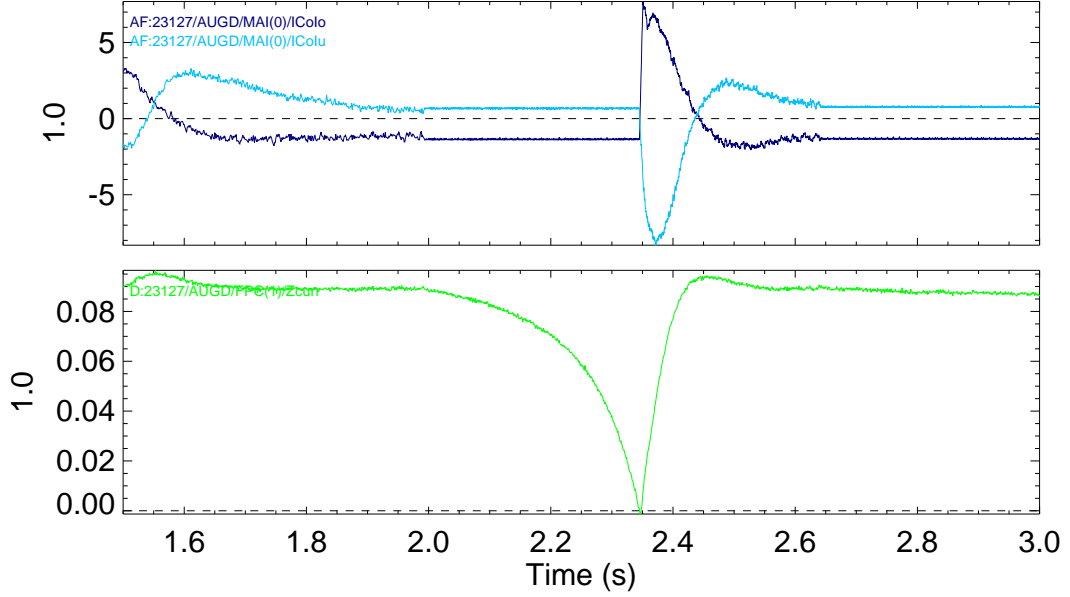
## 4.4 Application to realistic plasma configurations at ASDEX Upgrade

After the last sections showed that the code reproduces all expected phenomena properly, it shall now be applied to realistic configurations as they appear in the tokamak ASDEX Upgrade. In the past, several plasma discharges were created exclusively to examine vertical displacement events and the code is run to check whether the observed growth rates can be reproduced. For this purpose, for all following results the PSL are positioned like they are in ASDEX Upgrade and the boundary condition for the poloidal flux is  $\Psi = 0$  at infinity.

### 4.4.1 Moderately unstable cases

The first comparison between the behavior of an experimental plasma and the results of the developed code is done with the plasma discharges # 23127 and # 23124 which originate from a series of experiments to examine vertical displacement events. At first, the plasma with shot number # 23127 is examined. It is moderately elongated ( $\kappa=1.61$ , defined on the flux surface with  $\Psi_{norm} = 95\%$ ), the current is  $0.8\text{ MA}$  and the poloidal  $\beta_p$  is  $0.26$ . Active feedback is switched off at  $t = 2.0\text{ s}$  so the plasma is allowed to move vertically. Figure 4.30 shows the current of the upper and lower control coils (CoIo and CoIu) and the observed position of the plasma barycenter versus time. The plasma current barycenter is calculated with the same formula (4.1) used in this code.

As initial configuration, for our simulation an equilibrium at  $t = 2.0\text{ s}$  is cal-



cviver (gdc) v3.59 - User: cwigger - Tue Nov 30 10:26:09 2010 cwigger/cviver/StdSet/currents.cvs : 23127

**Figure 4.30:** *Upper box:* Currents in the poloidal field coils for position control *CoIo* and *CoIu*. *Lower box:* *z* position of the current barycenter measured in the experiment.

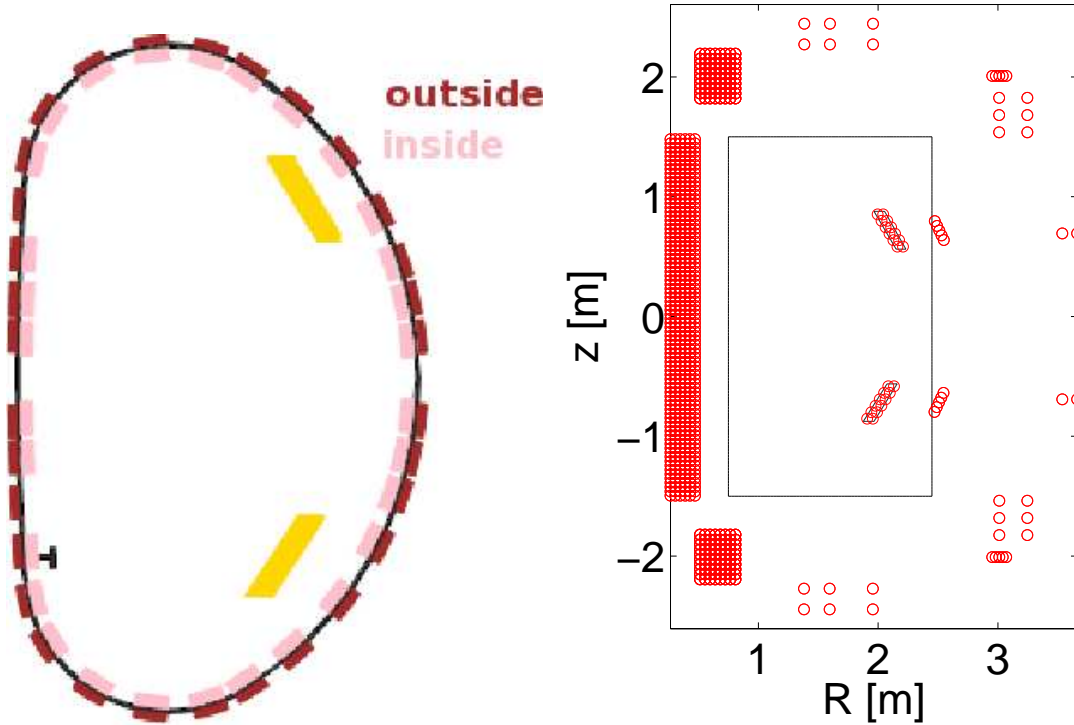
culated by the CLISTE code[43]. CLISTE uses data of experimental magnetic fields measured by field probes outside the plasma and the external currents including the PSL (see figure 4.31) to find an optimal match with the experimental situation by changing iteratively the profiles for  $p'$  and  $FF'$ .

Figure 4.32 shows the poloidal flux contours calculated by CLISTE. The red line marks the separatrix, which defines the plasma boundary.

Both CLISTE and the GEC provide an utility that calculates the stabilizing (with current filaments approximating the conducting structures) and destabilizing forces for a rigid shift. The linear growth rate is determined applying the formula [48]

$$\gamma = \left( \frac{F_{stab}}{F_{destab}} - 1 \right)^{-1} \gamma_w, \quad (4.7)$$

which is identical with eq. (2.33). However, the calculated forces take into account only contributions from the volume force of the plasma and neglect contributions from surface currents which also appear in a rigid displacement model [44]. This procedure, which has been followed always on ASDEX Upgrade, was justified by the assumption that in a more realistic situation the plasma shape



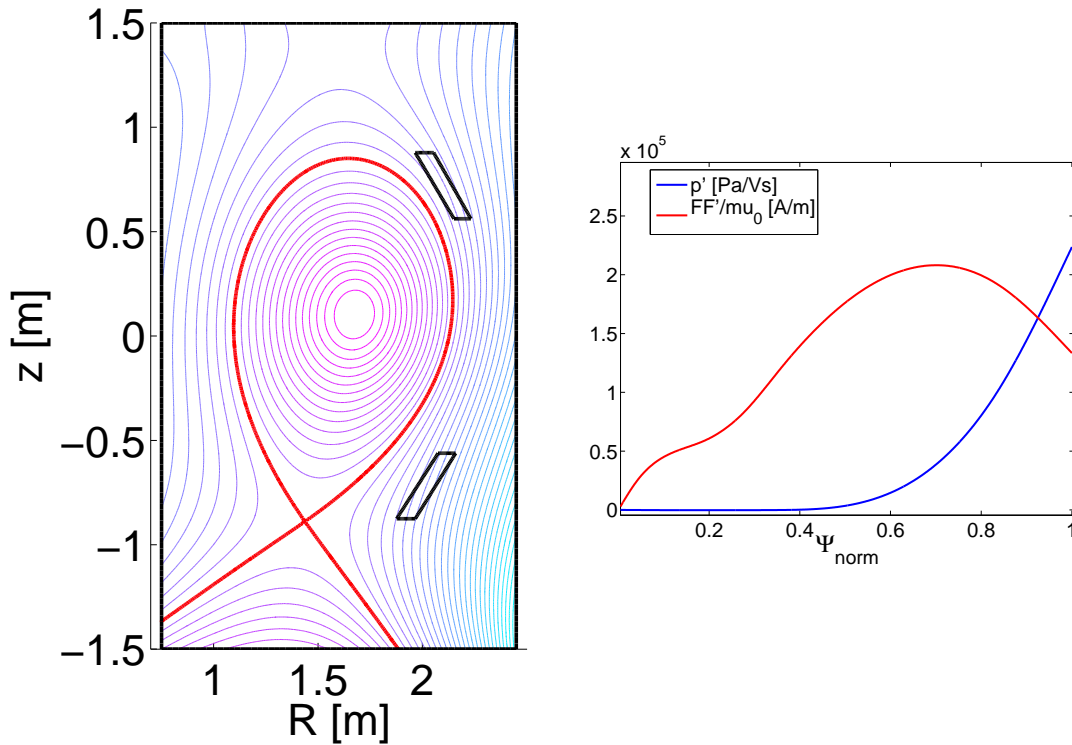
**Figure 4.31:** *Left:* Positions of the Mirnov coils measuring the magnetic field . *Right:* Filament representation of the poloidal field coils used by CLISTE (see also figure 2.11). Red circles denote a single filament which represents several windings of a coil.

would deform in a way that would eliminate these contributions. Note that any constraint on unstable displacements (like the restriction to rigid displacements) will lead to an underestimate of growth rates, and the neglect of stabilizing surface currents increases the expected growth rate. This is an assumption that cannot be verified with a model that restricts the plasma movement to a pure vertical shift (see section 4.4.3 for a more detailed discussion of this issue). For the equilibrium # 23127 formula (4.7) predicts a linear growth rate of about  $6 \text{ s}^{-1}$ .

The growth rates of the experiment and the code are determined by an exponential fit [26] which takes the form

$$z(t) = z_0 + \delta z e^{\gamma(t-t_0)}, \quad (4.8)$$

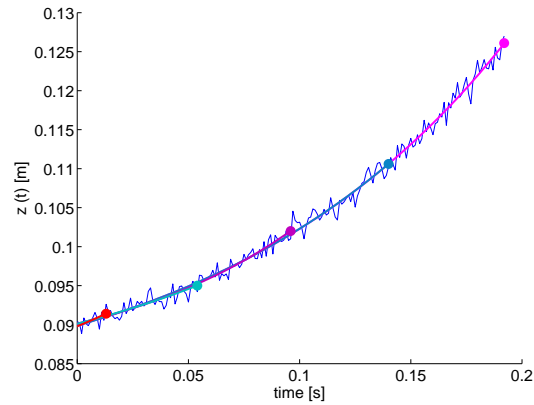
where the equilibrium position  $z_0$ , the amplitude of the perturbation  $\delta z$  are free parameters and the growth rate  $\gamma$  is the independent variable. In the time interval  $t - t_0$ ,  $t_0$  is the point of time at which active feedback is switched off



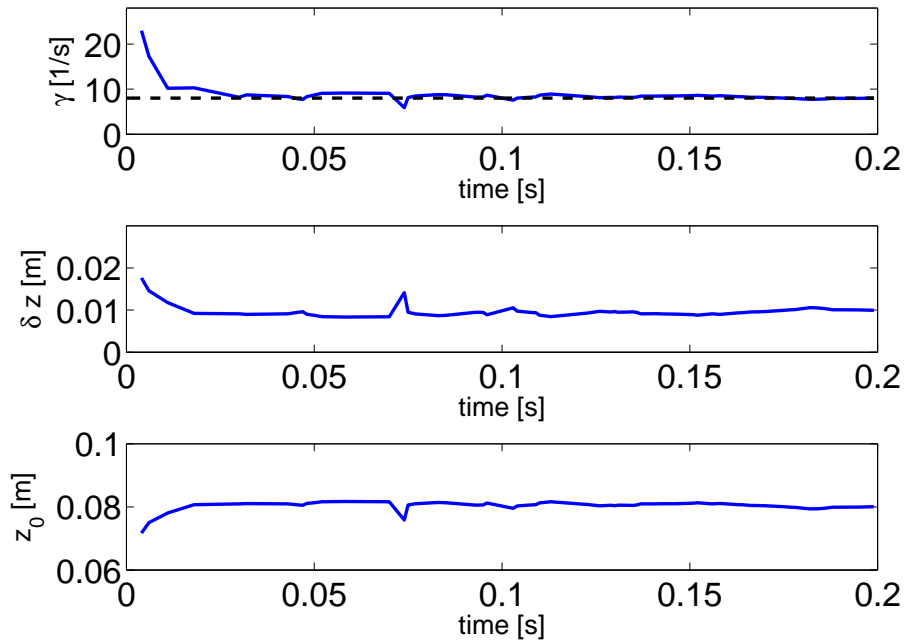
**Figure 4.32:** Left: poloidal flux  $\Psi$  as result of the CLISTE equilibrium reconstruction for shot # 23127. Right:  $p'(\Psi_{norm})$  and  $FF'(\Psi_{norm})$  profiles of the equilibrium.

(in case of the experimental curve) or the beginning of the simulation (in case of code results). The initial values of  $z_0$  and  $\delta z$  are not known and a fit described by equation (4.8) can yield growth that deviate from the real one if the time interval is too short. That's why the time interval is gradually enlarged until the effect of potentially wrong values of  $z_0$  and  $\delta z$  gets small enough. However, as the growth rate in the experiment or a nonlinear simulation will change in time, this procedure will approach a constant asymptotic value only over a part of the unstable event. Figures 4.33 and 4.34 show this procedure for an analytical curve with  $z_0 = 0.08 m$ ,  $\delta z = 0.01 m$ , and  $\gamma = 8 s^{-1}$ , superimposed by a noise function. The black dashed line in the upper plot shows the prescribed growth rate, the blue line the result of the fit. The accuracy of the method increases for larger time intervals, leading (in this case) to reliable results for  $t > 0.13 s$ .

If the growth rate changes with time, the fit yields an average growth rate which does not necessarily match the instantaneous growth rate well. But nevertheless an approximate initial growth rate can be obtained. Figure 4.35 shows the fit result for a function with time-dependent growth rate, again superimposed by a noise function. The initial growth rate is reproduced quite well, its accuracy getting worse with time, as expected.



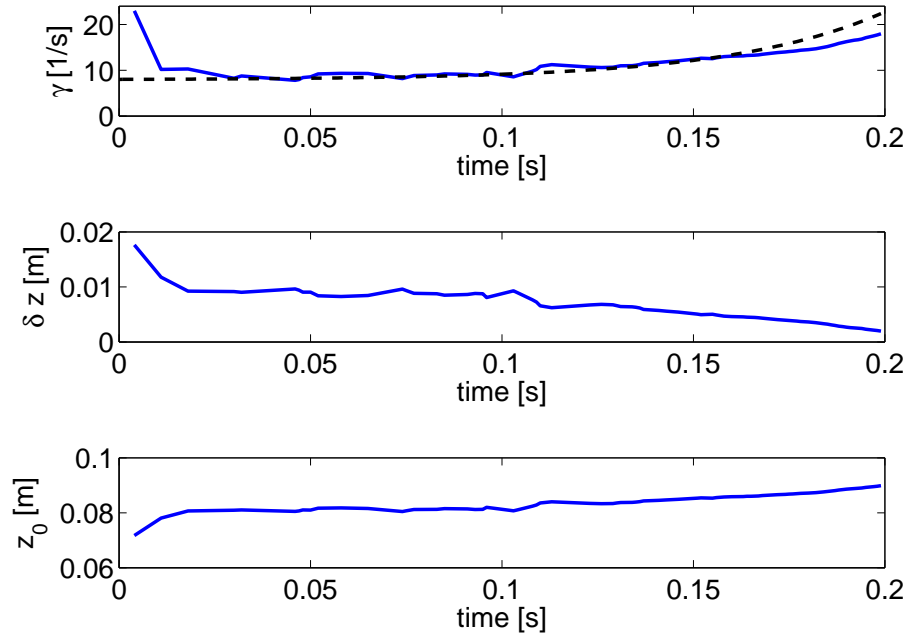
**Figure 4.33:** Original values of  $z(t)$  versus time (blue line) and several exponential fits with variable interval borders (marked with dots).



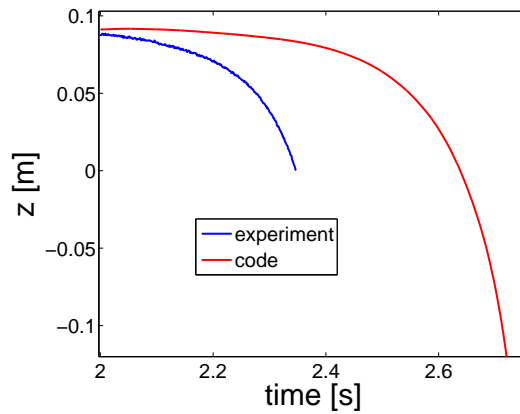
**Figure 4.34:** Resulting values for the growth rate  $\gamma$  (the prescribed analytical growth rate is shown as dashed black line), the amplitude of the perturbation  $\delta z$  and the equilibrium position  $z_0$  in dependence on the time interval border for a test case with constant growth rate.

This method can now be applied to  $z$ -position of the current barycenter  $z_c$  as it is measured in the experiment and as result of the code, shown in figure 4.36. The vertical movement of the experimental plasma stops at  $z \approx 0$  because active feedback is switched on again to stabilize the plasma (see figure 4.30).

Figure 4.37 shows the growth rate  $\gamma$  against  $z_c$ . The reason for using  $z_c$  rather than time as abscissa is that the initial amplitude of the perturbation is unknown

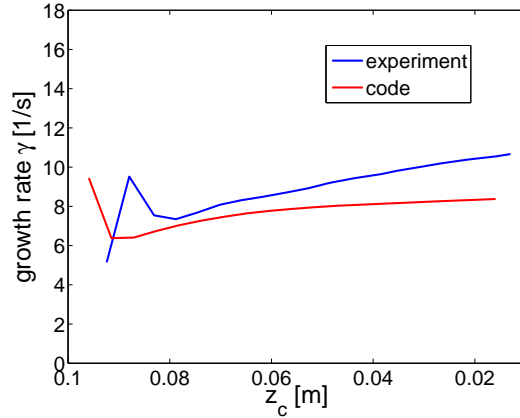


**Figure 4.35:** Resulting values for the growth rate  $\gamma$  (the prescribed analytical growth rate is shown as dashed black line), the amplitude of the perturbation  $\delta z$  and the equilibrium position  $z_0$  in dependence on the time interval border for a test case with time-dependent growth rate.



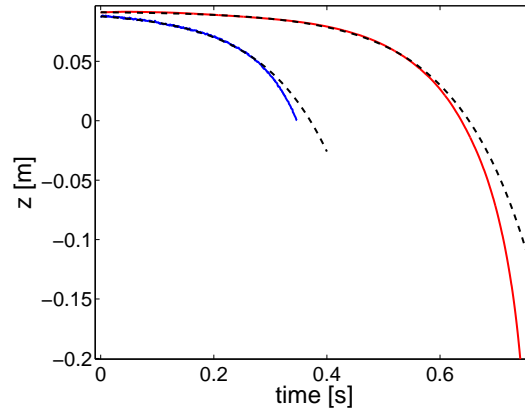
**Figure 4.36:**  $z_c$  of the experimental plasma (blue) and as code result (red) for shot #23127.

and generally not the same for code and experimental plasmas, so that in a plot with the same growth rate experiment and code result would show a different temporal behavior. As resistive wall modes describe a sequence of equilibria, the growth rate depends on the position of the plasma and the currents in the PSL rather than the time. Indeed, both experiment and code result yield good agreement with the growth rate predicted by eq. (4.7) at the beginning (prediction



**Figure 4.37:** Resulting values for the growth rate  $\gamma$  for shot # 23127. The blue line corresponds to the experiment, the red line to code results.

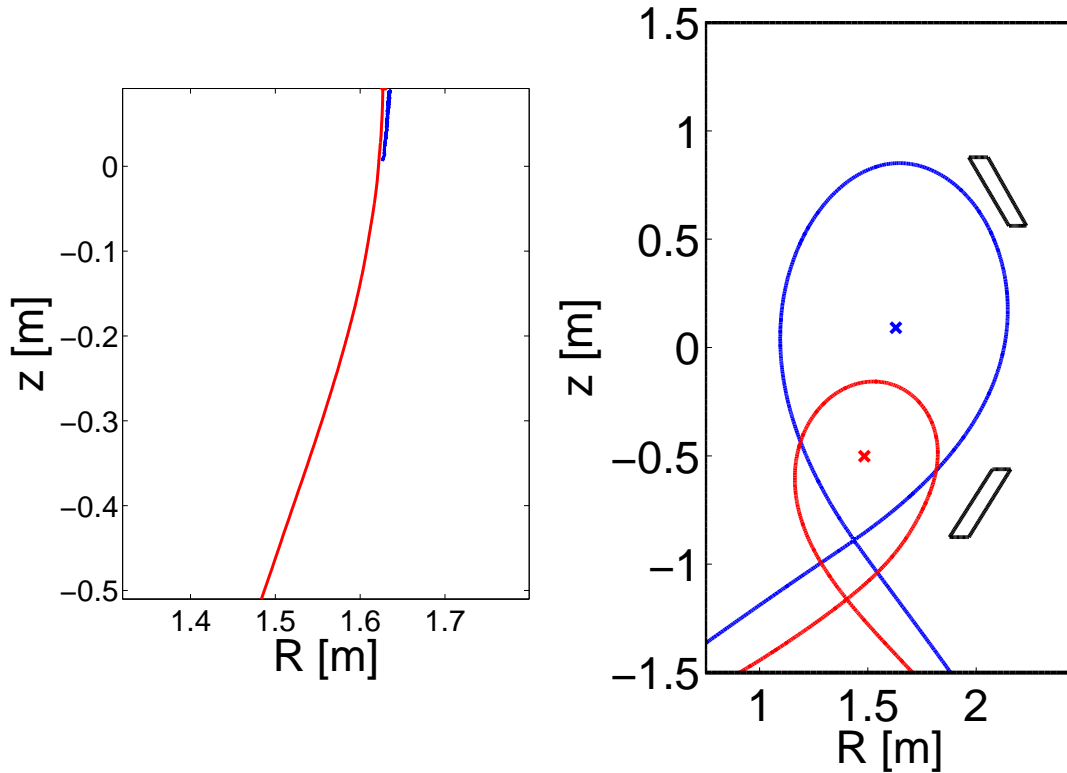
of formula:  $\approx 7.25 \text{ s}^{-1}$ , initial growth rate of experiment:  $\approx 7.5 \text{ s}^{-1}$ , initial growth rate of the code:  $\approx 7 \text{ s}^{-1}$ ). However, the growth rate increases during the vertical movement, which is reproduced the code. This is shown in figure 4.38.



**Figure 4.38:** Same as figure 4.36. Additionally, fits are shown (dashed lines) with a constant growth rate as determined at  $z_c = 0.06$ . For both experiment and code results, the fit matches the data well until  $z_c = 0.06$ . Afterwards both grow faster than corresponding to a constant growth rate.

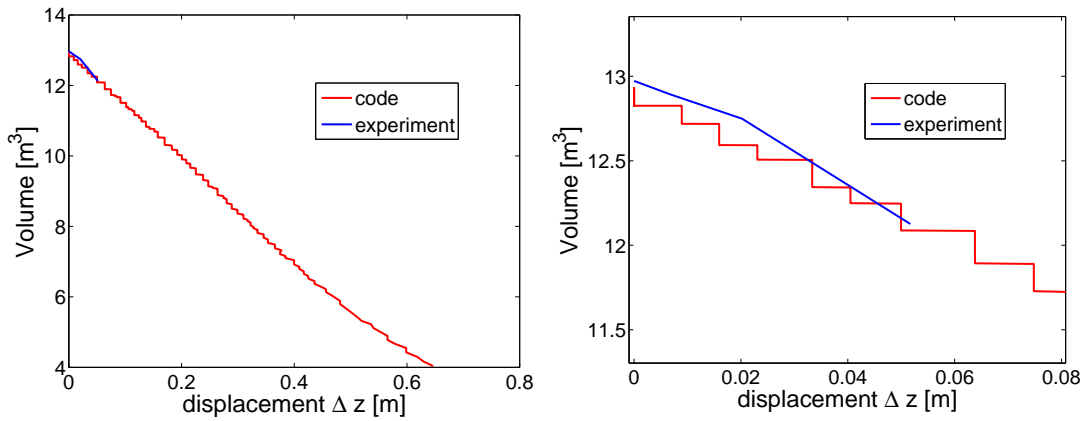
The plasma motion in the experiment is predominantly vertical, as figure 4.39 shows. The same behavior is reproduced by the code, but while the plasma is "caught" by active feedback in the experiment, it is allowed to continue its movement in the code, which makes potential threats in the further evolution of an instability visible. Now the radial component of the instability gets significant and the plasma shape adapts to the PSL, lowering the stabilizing influence of the

PSL. This effect is not observed for cases with no PSL where the growth is almost purely vertical. An example which shows the described effects more clearly can be found in section 4.4.3.

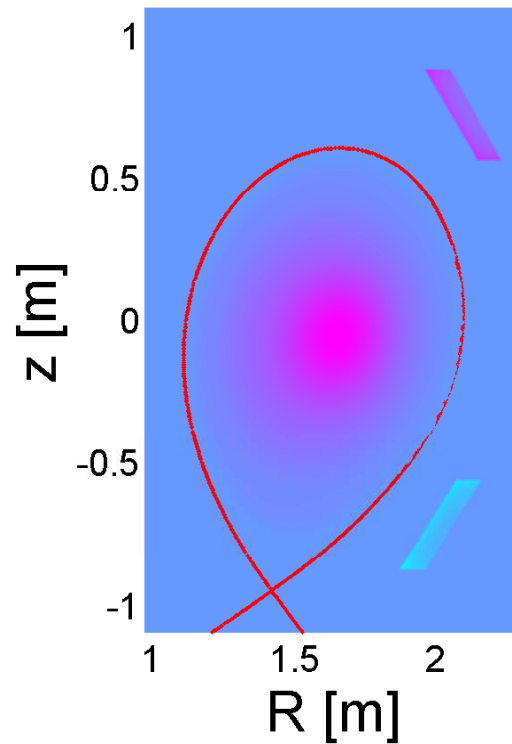


**Figure 4.39:** *Left:* traces of the current barycenter of shot # 23127 in the experiment (blue) and as results of the code (red). *Right:* plasma shape and current barycenter at the beginning (blue) and at the end (red) of the calculation.

The shape of the separatrices at the beginning and at the end show that the plasma volume (with the separatrix as plasma boundary) decreases. The volume versus the displacement of the magnetic axis is shown in figure 4.41 on the left for both experiment and code result. Obviously the code reproduces the shrinking well. The plasma shrinks because it moves towards the x-point, whose position is defined by the superposition of magnetic fields from external and plasma currents. As the position of the x-point is relatively stiff, plasma is scraped off. The right picture of figure 4.41 shows the current distribution of the plasma and inside the PSL. The inhomogeneous current distribution inside the PSL is clearly recognizable.



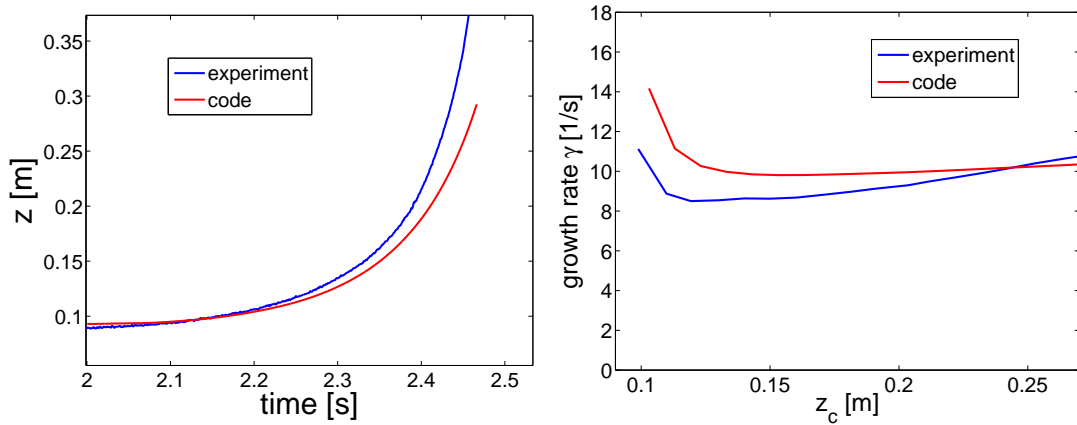
**Figure 4.40:** *Left:* Volume versus the  $z$  position of the magnetic axis for the experiment (blue) and as result of the code (red). The code results are piecewise constant because the position of the magnetic axis is obtained only with an accuracy determined the element diameter. *Right:* same plot, magnified to the range of the experiment.



**Figure 4.41:** Current distribution in the plasma and inside the PSL at  $\Delta z = 0.16$  m.

A second example of an experiment with a VDE is the plasma # 23124. It has similar parameters and profiles as shot # 23127 and active feedback is switched off again at  $t = 2.0$  s. However, the instability grows in upward direction for both experiment and code result. Note that there is no preferred direction for

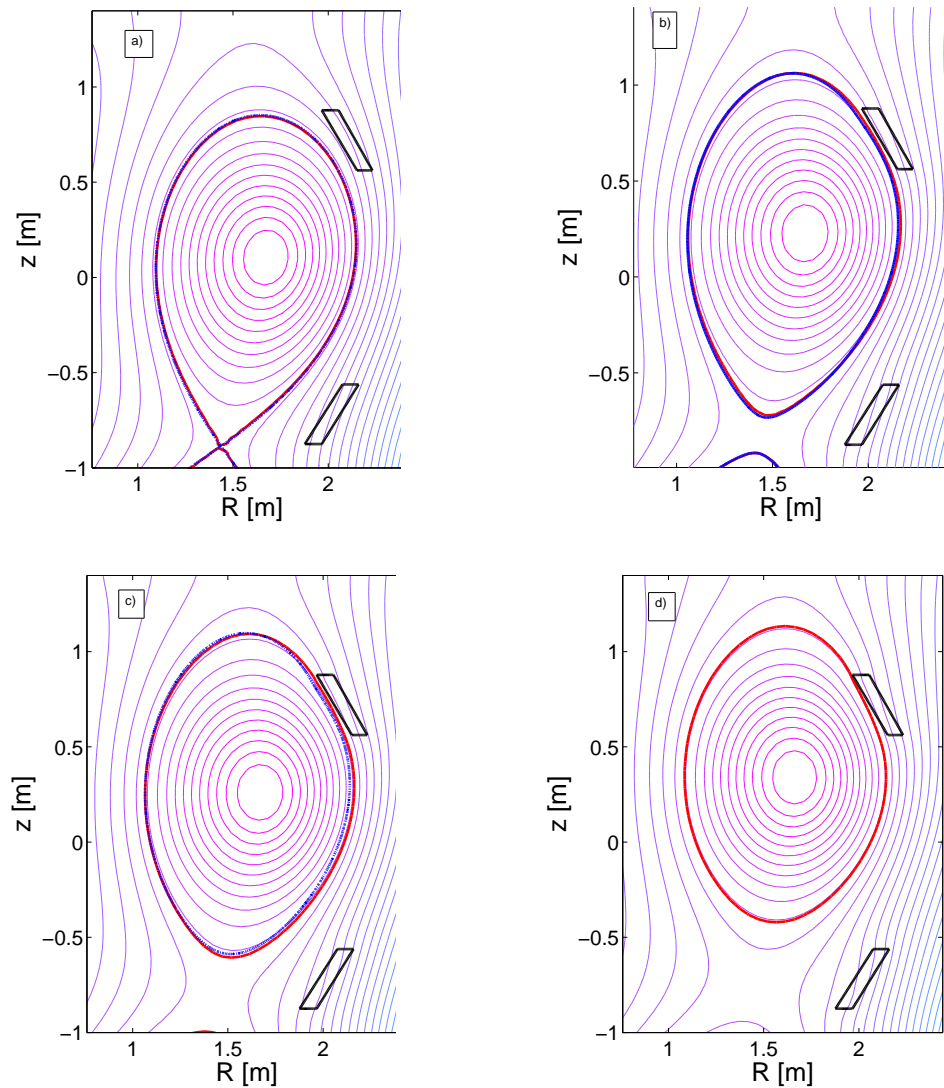
the growth of an unstable equilibrium, it depends on the initial perturbation including induced currents in the passive structures. The further evolution of an instability, however, is different because both plasma and passive conductors are not symmetric. Figure 4.42 shows  $z_c$  and the growth rates for both experiment and code results.



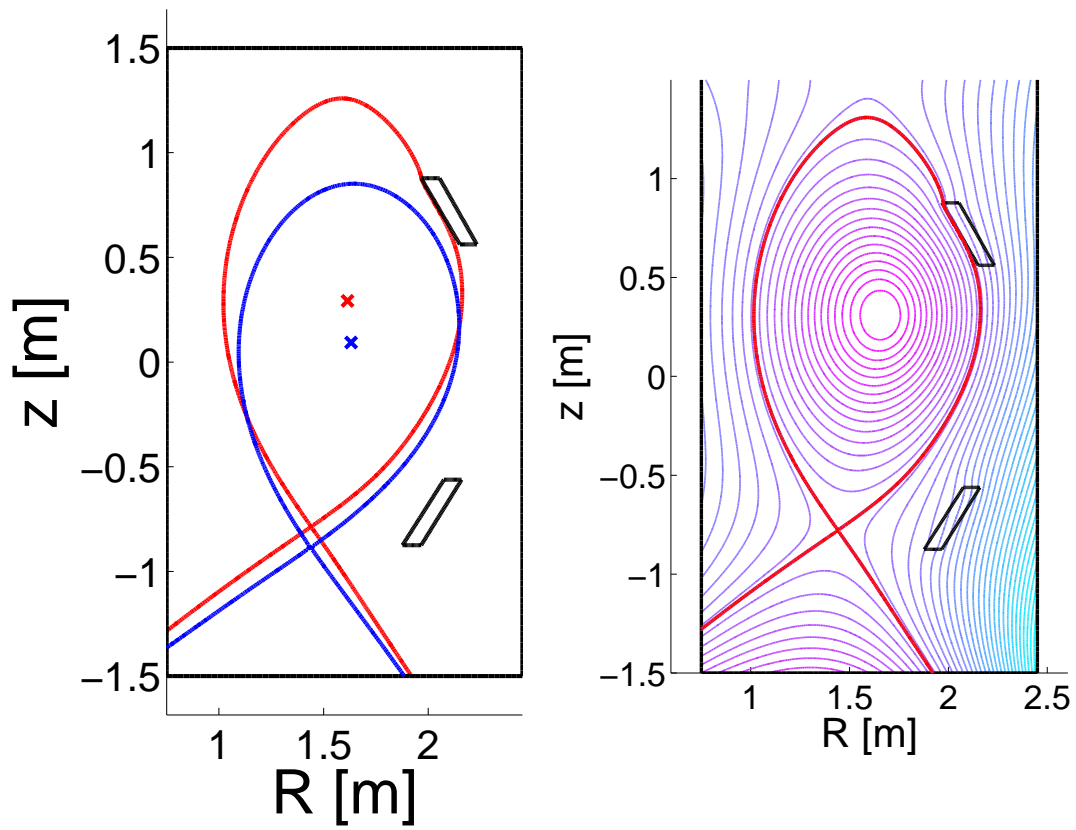
**Figure 4.42:** *Left:*  $z_c$  of the experimental plasma (blue) and as code result (red) for shot # 23124. *Right:* resulting values for the growth rate  $\gamma$  for shot # 23124. The blue line corresponds to the experiment, the red line to code results.

Again, the growth rate is reproduced well (prediction of formula (4.7):  $\approx 7 \text{ s}^{-1}$ , code result:  $10 \text{ s}^{-1}$ , experiment  $\approx 8.5 \text{ s}^{-1}$ ). In this case, the code terminates before the position at which active feedback is switched on again in the experiment is reached. The reason is that the plasma collides with the PSL at this position for the current barycenter, leading to abortion in several routines. Not only the growth rate is reproduced well, also the deformation of the plasma is matched as a comparison of code results and CLISTE reconstructions at different points of time shows. Figure 4.43 documents the evolution of the plasma at four different points of time. The plasma boundary, here defined as first flux surface (counted from the magnetic axis) that contains the whole plasma current, is marked for both experimental reconstruction with CLISTE and as result of the code. The non-linear behavior of the plasma topology is matched well, the influence on the plasma shape is even more obvious for the separatrix (see figure 4.44).

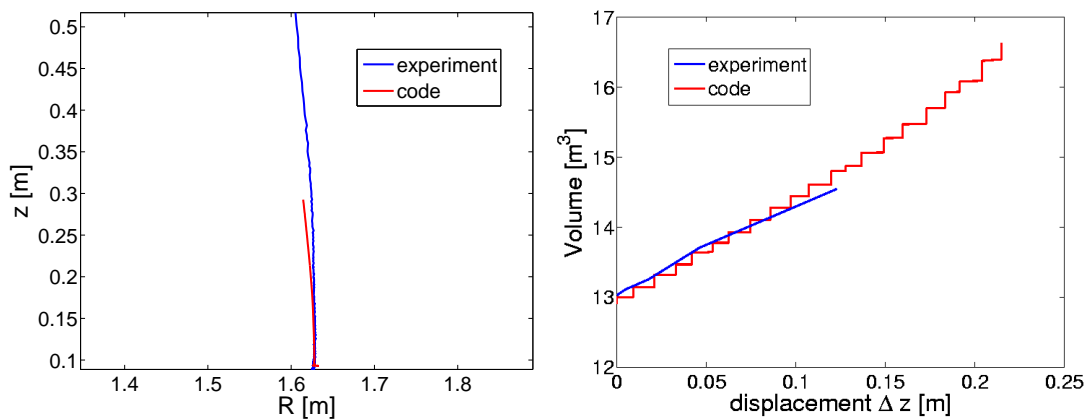
This time the volume inside the separatrix increases (shown in figure 4.45 on the right) in both cases. The values for the CLISTE reconstruction are shown only until the plasma boundary is not the separatrix anymore but defined as the last closed flux surface (with the PSL acting as limiter).



**Figure 4.43:** Comparison of CLISTE reconstruction (flux surfaces and red plasma boundary) of measured data and code results (blue plasma boundary). CLISTE reconstructions and code results are taken at the same vertical position of the plasma. The poloidal flux, the plasma boundaries and PSL positions for shot # 23124 of the experiment are shown. Here, the plasma boundary is defined as the first flux surface (counted from the magnetic axis) that contains the whole plasma current. Time points: a)  $t = 2.0$  s, b)  $t = 2.40$  s, c)  $t = 2.42$  s, d)  $t = 2.45$  s (no code result anymore).



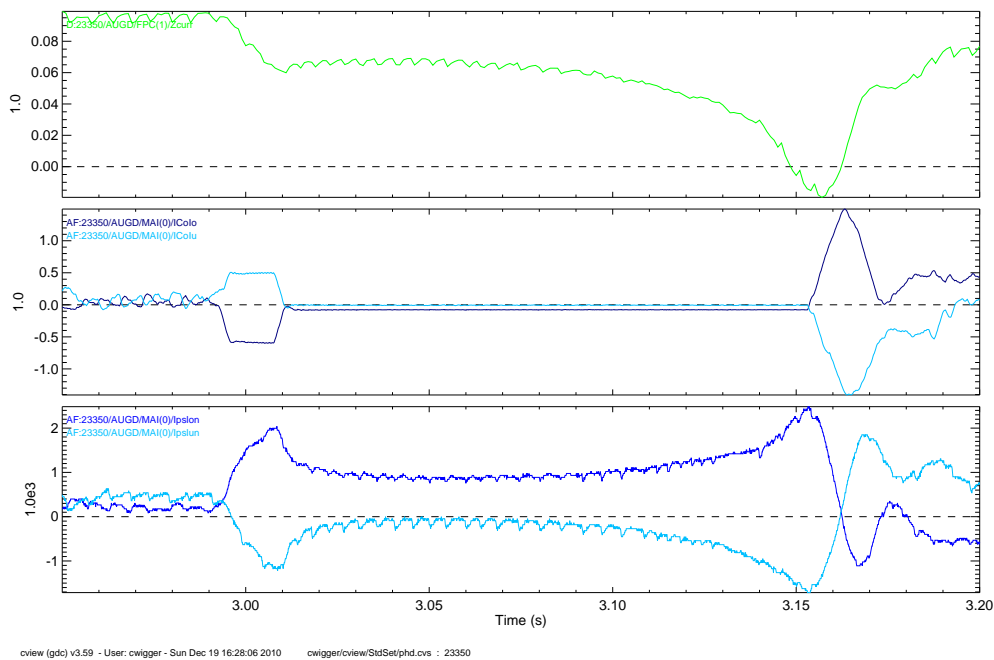
**Figure 4.44:** *Left:* Separatrices and current barycenters of shot # 23124 at the beginning (blue) and at the end (red) of the calculation. *Right:*  $\Psi$ -contour plot of shot # 23124 at the end of the calculation.



**Figure 4.45:** *Left:* traces of the current barycenter in the experiment (blue) and as results of the code (red) for shot # 23124. *Right:* Volume enclosed inside the separatrix versus the  $z$  position of the magnetic axis for the experiment (blue) and as result of the code (red).

### 4.4.2 Strongly unstable cases

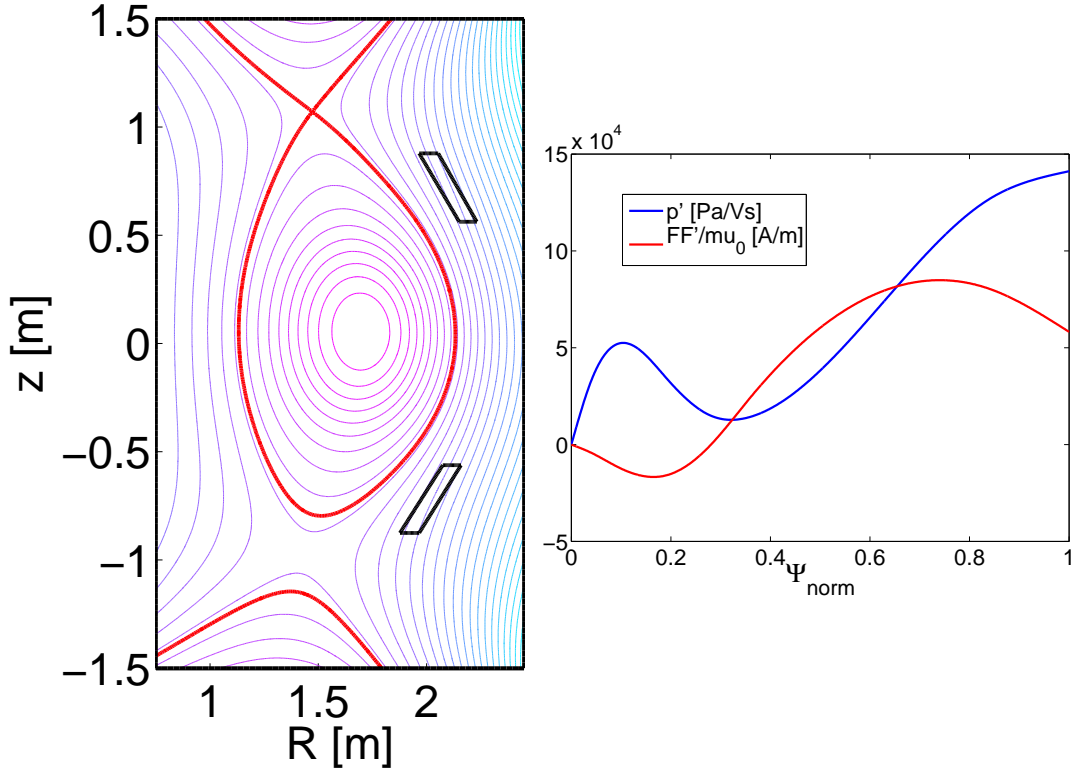
After the first series of experiments concerning VDEs was finished, another one followed in which the plasmas were more elongated ( $\kappa = 1.82$ ), leading to stronger instabilities. Their x-point is located above the magnetic axis and their poloidal  $\beta$  is approximately 0.96. One representative of this later series is shot # 23350. Contrary to the examples treated above, this time the plasma is given a "kick" by applied currents in the *Co*-coils (the coils labelled *CoIo* and *CoIu* in figure 2.11, used for fast control of the plasma position) in order to give the plasma an initial perturbation and to accelerate the growth of the instability to observable magnitude. Afterwards, active feedback is switched off.  $z_c$ , the current signal in the *Co*-coils and the signal of the PSL are shown in figure 4.46. The current in the *Co*-coils displace the plasma and induce a current in the PSL.



**Figure 4.46:**  $z_c$ , current signal in the *Co*-coils and in the PSL for shot # 23350.

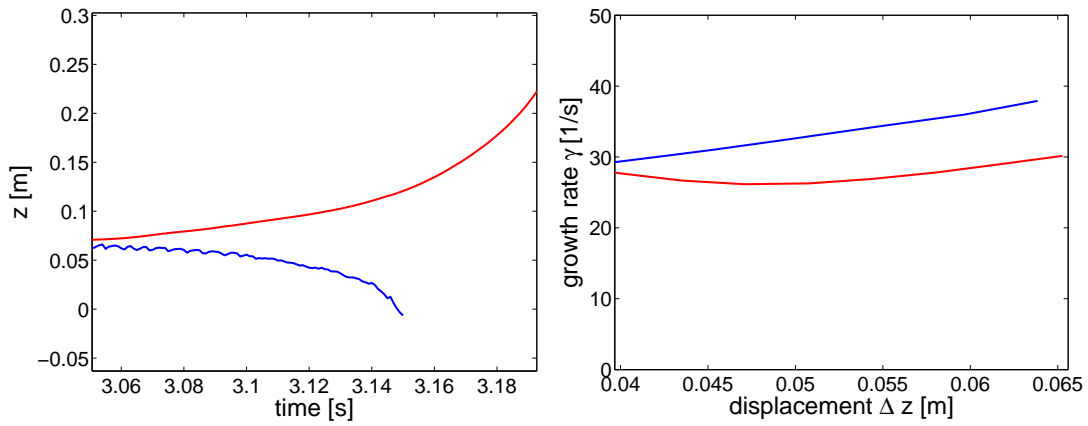
The equilibrium is calculated at  $t = 3.05$  s, i.e. after the "kick".  $\Psi$  contours and the profiles for  $p'$  and  $FF'$  for the first case are shown in figure 4.47.

Figure 4.48 shows the same plots for  $z_c$  and the growth rate as above. The direction of the instability evolves differently; while the experimental plasma moves downwards, it moves upwards in the code. The probable reason is that the initial current distribution in the PSL is not known and CLISTE approximates it only roughly by current filaments. Although the effect is small, it can be sufficient



**Figure 4.47:** Left: poloidal flux  $\Psi$  as result of the CLISTE calculation for shot # 23350. Right:  $p'(\Psi_{norm})$  and  $FF'(\Psi_{norm})$  profiles of the initial equilibrium.

to change the direction. Whereas the true amplitude of the initial perturbation and the direction of motion should depend on all initial conditions (including current distributions in passive elements, which are partly not measured) the growth rate should just depend on the equilibrium and be robust with respect to the excitation of the instability. In fact, our computed initial growth rate  $25 \text{ s}^{-1}$  is quite close to the experimentally measured one  $30 \text{ s}^{-1}$ . In particular, however, in this case - closer to the limits of controllability of the mode by passive elements - we observe a large difference between our code calculations and the results of the simplified formula (4.7) which would give a growth rate of about  $7 \text{ s}^{-1}$ . In the course of the instability, the growth rate increases like in the other cases. A more extensive comparison of growth rates predicted by formula (4.7) and as result of code calculation is given section 4.4.3. Figure 4.49 shows again the separatrices and current barycenters of the plasma #23350 at the beginning and at the end of the calculation. Note that the plasma in the experiment is caught again by active feedback, while the code continues the calculation until the plasma reaches the computational domain.



**Figure 4.48:** Left:  $z_c$  of the experimental plasma (blue) and as code result (red) for shot # 23350 Right: resulting values for the growth rate  $\gamma$  for shot # 23350. The blue line corresponds to the experiment, the red line to code results.

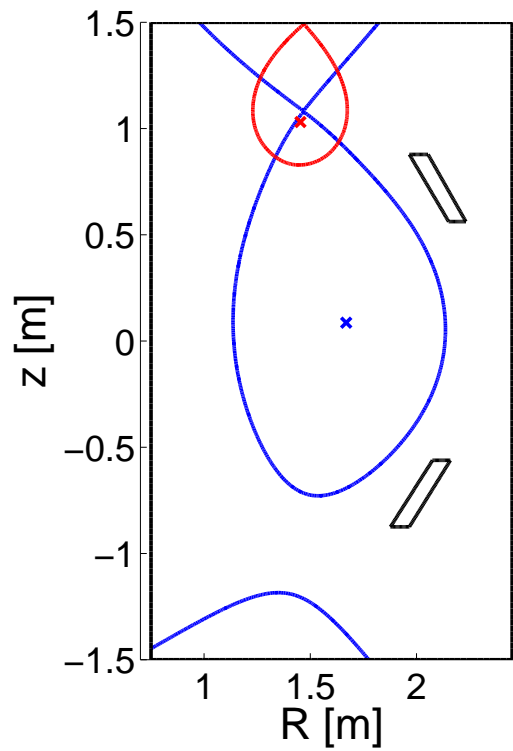


**Figure 4.49:** Separatrices and current barycenters of shot # 23350 at the beginning (blue) and at the end (red) of the calculation.

### 4.4.3 Approach to marginal stability

From the examination of the preceding examples we can draw two conclusions:

1. The neglect of the stabilizing surface currents in formula (4.7) is well-justified.
2. The applicability of this formula and the "modified rigid displacement model" is limited to plasmas that are far away from the point of marginal ideal stability.

The calculations reported in figure 4.50 substantiates these conclusions. They show the growth rates for a set of equilibria for which the currents in the PF-coils controlling the ellipticity (and with it the destabilizing forces) is successively increased by a factor. The blue line corresponds to the prediction of formula (4.7). The black line is the result of the formula, if the stabilizing surface contributions are taken into account. The red line shows the result of the code. Indeed, experimentalists at ASDEX Upgrade observe a discrepancy of predicted and observed growth rates, those of the experiment being systematically larger than the predicted ones [49].

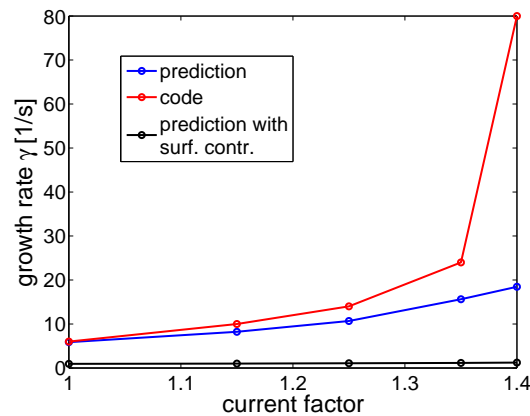


**Figure 4.50:** Growth rates predicted by formula (4.7) (blue) and as result of code calculation (red).

### Differences to rigid displacement model

One of the key issues of this work is to take into account the influence of the induced currents in conducting structures on the plasma movement. In order to

emphasize that important effect, the evolutions of an unstable plasma with and without PSL are compared. The plasma equilibrium is calculated by GEC, as it is not important to match experimental conditions for this purpose. Figure 4.51 shows the trajectories of the current barycenters for absent and present PSL (with  $\gamma_w^* = 0.01$ ).

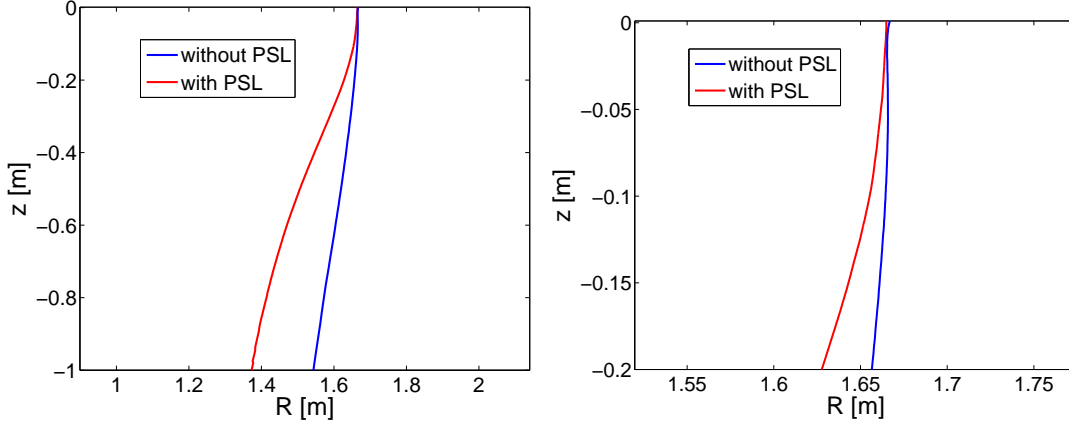


**Figure 4.51:** *Left:* traces of the current barycenter in the case of absent (blue) and present (red) PSL. *Right:* Magnified section from  $z = 0$  m to  $z = -0.2$  m of the same plot.

It is obvious that the plasma moves radially inward to minimize the stabilizing effect of the conductors, which leads to an enhanced growth rate compared to the case of a rigid shift. From the left picture it is clear that that this effect gets very large in particular during the later (nonlinear) phase of the instability, but a zoom (right picture of the same figure) reveals that an effect exists also during the linear phase. Both in the case with and without PSL, the unstable motion differs from the purely vertical displacement assumed in the model of rigid displacement [44] and formula (4.7). The radial movement is inevitable after a certain distance, as a purely vertical movement would lead to a collision with the PSL (like in the case of shot # 23124). Not only the trajectory of the plasma is changed, but also the plasma shape. Figure 4.52 shows the plasma boundaries if PSL are absent (left) and present (right) for several displacements  $\Delta z$ . Obviously, the plasma shape adapts to the shape of the PSL to minimize their stabilizing influence. Even after the plasma has passed the PSL, the shape remains deformed and exhibits a significant difference to the plasma without PSL influence.

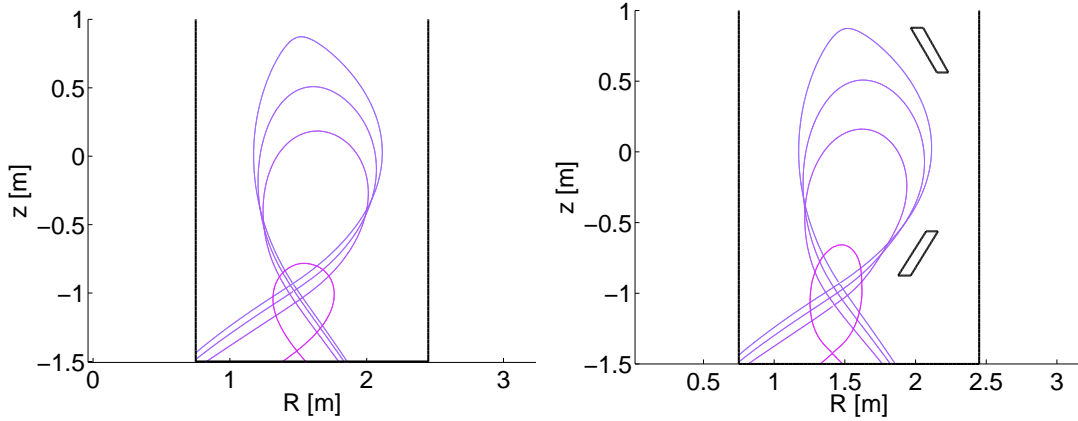


**Figure 4.52:** Plasma boundaries in case of absent (left) and present PSL (right) after displacements  $\Delta z$  of 0.25, 0.5 and 1.0 m.

#### 4.4.4 Stabilization by a continuous resistive wall

A future concept for ASDEX Upgrade is to remove the PSL and use the surrounding resistive wall to stabilize the plasma. This allows a much larger plasma current and plasma volume and the latter also increases the stabilizing coupling to the wall. As outlined before, the PSL were initially installed because they have a much longer  $L/R$ -time than the present wall. Since then, due to the advances in the sector of high performance computing the time to calculate the necessary voltages or currents in the control coils for active feedback decreased enormously, allowing for smaller resistive times in the passive conducting structures. With some small changes in our code, this wall can also be modeled. The subsidiary condition for the current in the wall is in principle the same as in the case of PSL: no net current shall exist, i.e. any induced current flowing locally in the wall must be canceled out by another current of opposite direction anywhere else in the wall (this refers to the case of a continuous wall, slitted once in toroidal direction; in the absence of such a slit, the subsidiary condition would be substituted by the trivial relation  $\delta\phi = 0$ ). As no closed contours encircling the wall can be defined, the condition is expressed as

$$\int_{wall} \mathbf{J}_\phi \, dA = 0,$$

where the integral includes the whole area of the wall in the poloidal plane. Figure 4.53 shows an GEC-equilibrium surrounded by the wall of ASDEX Upgrade (marked red). Nothing changes for the boundary conditions at the border of the computational domain (black lines).

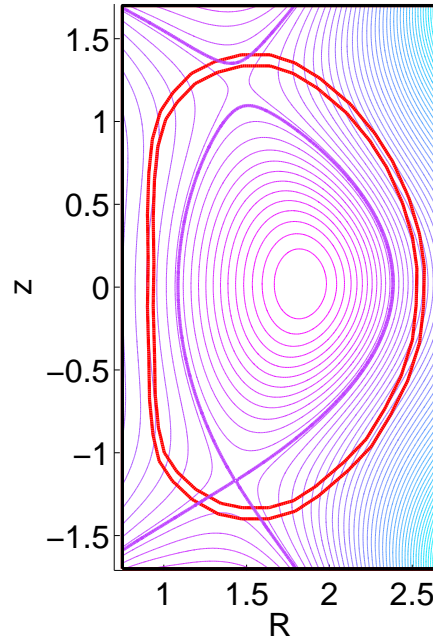


**Figure 4.53:**  $\Psi$  contours of an equilibrium inside a conducting wall. The contour belonging to the separatrix value is thick. Red lines denote the wall, black lines the computational boundary.

The resistance of the wall can be varied, either by changing the value of its conductivity, its thickness or both. The resistive time of the present wall is known from the experiment. It is about  $L/R \approx 10 \text{ ms}$  for the dominant wall current mode induced by a vertical shift of the plasma column. The current decay method presented in section 4.1.2 can be used here as well by prescribing such a current distribution in a in the wall. In this way,  $L$  can be determined to  $0.78 \mu\text{H}$  for a nominal conductivity and thickness of the wall  $\sigma_w = 3.5 \cdot 10^6 \text{ Sm}^{-1}$  and  $\Delta_w = 3.5 \text{ cm}$ .

Any movement of the plasma leads to a current induction in the walls that tries to stabilize it. Figure 4.54 shows current distribution inside the wall at  $z_c = -0.12\text{m}$  as result of plasma movement.

The equilibrium shown in figure 4.53 has a total current of  $I = 2.5\text{MA}$  and  $\beta_p = 0.83$ . The plasma current, magnetic fields and volume are much larger than current experimental plasmas in ASDEX Upgrade, but as outlined above the stabilizing effect of the wall is smaller compared to the situation with PSL as stabilizing conductors. Figure 4.55 shows the code's result for the z-position of the current barycenter. As the wall is relatively close to the plasma boundary, the column can move only about  $15 \text{ cm}$  before reaching the wall.

The prediction for the growth rate following formula (4.7) is approximately  $50 \text{ s}^{-1}$

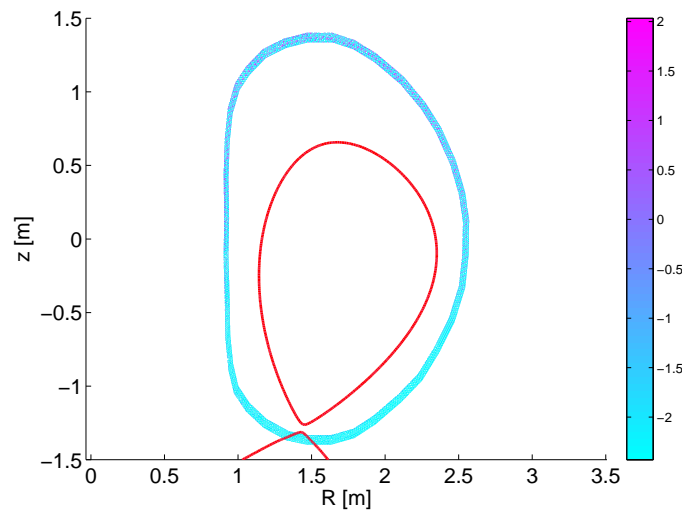


**Figure 4.54:** Current distribution inside the conducting wall as consequence of a vertical movement of the plasma at  $z_c = -0.12m$ .

compared to a linear growth rate determined by the code of about  $80 \text{ s}^{-1}$ . The non-linear evolution is shown on the right of figure 4.55.

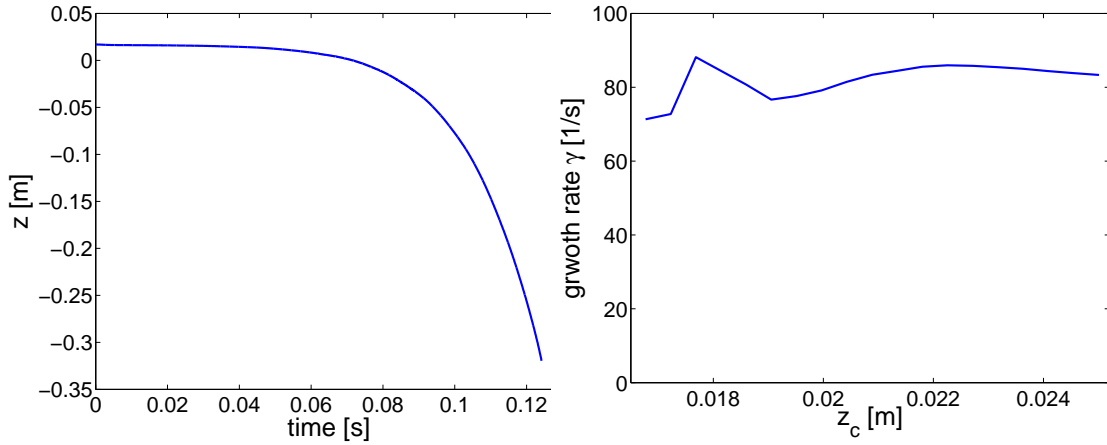


**Figure 4.55:** Left:  $z_c$  versus time. Right: growth rate  $\gamma$ .



## 5 Summary and Outlook

In this work, a finite element based code is developed and applied that solves the nonlinear, resistive, reduced MHD equations to simulate and understand axisymmetric instabilities in tokamaks. This kind of instability takes shape of a predominantly vertical shift of the whole plasma column, leading to the expression of vertical displacement event (VDE). Its origin lies in the shaping of the plasma cross section in order to improve several figures of merit, above all the economical efficiency of a fusion reactor serving as power plant. When not stabilized, VDEs exert due to the large currents and temperatures involved tremendous forces and heat loads on structural and first wall components that pose a threat for present and future fusion devices.

In the practically relevant regime of operation of all modern tokamaks, this instability takes the form of a resistive wall instability. This implies that it would be stabilized by induced mirror currents in infinitely conducting walls (or other structures), but grows for finite electrical resistance of the latter on the resistive time scale which is determined by the conductivity and geometry of the conductors. The growth rate of the instability is thereby slowed down from the Alfvénic time scale (of the order of  $\mu s$ ) to time scales of the order of  $ms$ . This gives the active feedback system the time to calculate and establish the necessary currents to completely stabilize the plasma movement.

In order to calculate the growth rate of an axisymmetric instability, as a first step a linear eigenvalue code for an ideal (infinitely conducting) plasma developed in the frame of a diploma thesis was extended to take into account the resistivity of the passive conductors. As the passive stabilization of experimental plasmas in ASDEX Upgrade (the experimental fusion device of the IPP in Garching) is achieved almost completely by massive copper loops (PSL) and not by the surrounding vessel wall, their geometry was taken into account for the calculations. For strongly unstable cases - which were the main motivation of this effort - the results of this approach deviated strongly from the growth rates observed in experiment, and indicated an important dependence on the conductivity of the plasma and in the passive conductors. Moreover, only a nonlinear code would be able to follow the plasma during the later stages, where experimental indications suggest a variation of the growth rate. Therefore the new code described in this

work was developed, including finite conductivities and non-linearities.

In fact, two code versions have been developed and are described here. One is restricted to plasmas with  $\beta = 0$  and an unrealistic initial density distribution. Under these constraints it allows formally to approach also the case of inertially limited plasma motion, although numerical constraints prevent using realistic plasma densities (and hence Lundquist numbers). The other version allows the inclusion of finite pressure, but yields valid results only in the resistive wall mode regime, i.e. on the resistive time scale. This is only a weak restriction, as the resistive time scale is the relevant one for experimental realities. In case of vanishing plasma pressure and in the resistive wall regime, both versions yield the same results. Except for the chapter describing the test cases, all shown results were obtained by the version which includes finite plasma pressure.

Passive stabilizing structures, whose accurate description is very important, are easy to model and modify due to the usage of triangular finite elements. Current distributions inside the plasma and the conductors can be treated very realistically. For the present applications, a constraint is implemented on the PSL that ensures the equality of the currents in the upper and lower leg due to their series connection. A great effort was made into implementing a boundary condition on the computational domain that simulates a vanishing poloidal perturbation flux at infinity (i.e. as if no wall would exist at all) using Green's function approach (which is a dynamic analogue to the approach of Lackner [8] and a two-dimensional modification of the approach used by Merkel [46]; Jardin [11] used a similar method). Indeed it was found, that this kind of treatment of the boundary is very important for movements including a net displacement of the plasma column (corresponding to an  $m = 1$  component), as other boundary conditions (e.g. Dirichlet) at the computational border would strongly influence (reduce) the growth rate, unless the computational domain was extended leading to an enormous increase in computation time.

The testing procedure of the code includes the comparison with a engineering model in which plasma and conductors are modeled with current filaments. This model is instructive to understand the role of wire (or plasma) inertia and the resistive response of the conductor, and in particular the transition from inertia limited motion (for strongly destabilizing equilibrium fields and insufficient coupling between the wire (plasma) and the stabilizing conductors) to one corresponding to a sequence of static equilibria changing with the resistive decay of the induced currents in the conductors.

A more quantitative, but still simplified engineering model used so far on ASDEX Upgrade to determine admissible plasma configurations and the settings of control parameters was based on results of a code testing the plasma against rigid vertical displacement, but omits stabilizing terms corresponding to surface

---

currents, which are deemed to be suppressed by deformations of the plasma. One of the motivations for the development of our code was to test the limits of validity of this ad-hoc model, which had performed satisfactorily during conservative operation of the device, staying relatively distant from limits to the stable regime. Closer to the "ideal" stability limit, the plasma movement becomes more complex and experimental results show a strongly increased growth rate (up to a factor of 10 in the range experimentally explored).

Dedicated VDE experiments had been carried out only under a limited number of cases, which were also studied with the code. These cases included two cases with both moderate growth rate, but unstable plasma displacements in different direction, and a strongly unstable situation, where the displacement was initiated by a vertical kick given to the plasma by an impulsive radial field. In all cases, the code reproduced well (within 20%) the experimentally observed growth rates. The ad-hoc expression used previously did comparably well in the moderately unstable cases, but gave - by a factor of 4 - smaller growth rates for the strongly unstable case. When the direction of the unstable plasma motion (which is sensitive to small differences in the initial conditions, e.g. the current distribution inside the PSL, which cannot be measured) agrees between code results and experiments, also the nonlinear stage and the deformation of the plasma in it are well reproduced. When the directions differ, the growth rates agree well in the linear regime (according to the theory), but differs, of course, at later stages. As experimental campaigns to measure growth rates in the strongly unstable situations are associated with significant danger to the device (as an intentional, temporary switching off of the feedback circuit can easily lead to an irrecoverable loss of control), a sequence of calculations was carried out pushing beyond the experimentally explored range of configurations and mapping the growing discrepancy between the ad-hoc formula prediction and the developed code.

The code was developed for the application to ASDEX Upgrade, but it can be easily adapted to other devices. The implementation of (rather unusual) dedicated passive conductors like the PSL is an even more demanding situation than the standard case with only conducting walls, as here no simplifying approximations like "thin walls", where a homogeneous current distribution across the thickness of a conducting structure is assumed, are possible. With small changes, the situation with a conducting wall (again without the thin wall approximation) instead of the PSL can be simulated, which is a possible future concept of ASDEX Upgrade and the standard scenario for ITER. The results are shown in section 4.4.4 and yield growth rates which would appear to be controllable by a suitably upgraded feedback system. If passive stabilization is accomplished in this way, the plasma has to be positioned much closer to the wall to increase the inductive

---

coupling and active feedback has to react very fast.

In its present form, the code can predict growth rates and limits of controllability for a variety of different configurations and allows to analyze a posteriori particularly interesting discharges. One immediately possible application would be the development of a data bank, in which growth rates of a broad class of equilibria are pre-calculated as it is already done with equilibria. This data bank could be subjected to a similar function parametrization technique as it is done for the equilibria, and the resulting fit-functions could be made available to experimentalists and engineers for the discharge planning and a fast analysis. An estimate of the required computing time is given in appendix section A.6, which shows that such a data base could be established with a modest effort requiring approximately 10000 CPU hours.

Of course, there is still potential in the code for extending the spectrum of its functionality. For example, an active feedback algorithm which calculates the necessary currents in the poloidal field coils to stabilize the axisymmetric motion could be included. Some of the simplifying assumptions made in the code, that are expected to have only weak influence on the plasma behavior in the linear phase of the evolution, could be dropped when focusing on later stages. That would require an increased amount of experimentally measured data in this stage to be in a position to compare experimental and code results. Relevant effects are the inclusion of transport models of particles and energy across flux surfaces, Ohmic heating and radiation losses. This would lead to a change of the equations that govern the temporal evolution of density, pressure and conductivity, while they continue to be flux surface averaged quantities. However, during the latest stages of an VDE, non-axisymmetric effects can get important or even dominant and it would have to be examined to what extent the code yields good agreement.

In recent years, large international effort has been made to develop a three-dimensional non-linear stability code. The Max-Planck-Institut für Plasmaphysik is part of that collaboration and contributes the adaption to boundary conditions at infinity and the inclusion of axisymmetric ( $n = 0$ ) components of the perturbation. Results of the code presented in this work and possible further runs in the future can serve as benchmark of this more general code during the axisymmetric phases.

# A Appendix

## A.1 Finite element method

The way we chose to solve our equations is the finite element method (FEM). It's origin lies already 150 ago when it was developed to solve minimization problems, but first with the development of computers it's popularity began to grow quickly. Today it's widely used for a large number of problems encountered in all areas of science and industrial applications, but the idea is the same as at it's beginning: discretize a domain into elements to solve the problem there approximately.

### A.1.1 Shape functions

When using the finite element method, one always looks for an approximate solution on a discretized domain (grid) composed of smaller subdomains (finite elements), mostly triangles or rectangles. If  $u$  is the real solution, one can find in each element an approximate solution  $u_h = \sum_i N_i u_i$ , where the  $N_i$  and  $u_i$  are the so-called shape functions and the values of the approximate solution on a grid point  $i$ . First of all it is necessary to understand how quantities are represented. Therefore the shape functions are of fundamental importance. The form of the shape functions depends on the problem and its discretization. In the vast majority of applications, polynomials are used, but e.g. trigonometric functions are possible as well. The form of the polynomials for a triangle finite element differ from those of a rectangle. As only triangles are used in the code, the presentation of shape functions is limited to these shape functions. The linear triangular element has straight sides and a node on each of it's three corners i,j and k. A scalar quantity can be interpolated with

$$\phi = \alpha_1 + \alpha_2 x + \alpha_3 y,$$

which is complete as it contains one constant and every possible linear term. The nodal conditions are:

$$\phi = \Phi_i \text{ at } x = X_i, y = Y_i$$

$$\phi = \Phi_j \text{ at } x = X_j, y = Y_j$$

$$\phi = \Phi_k \text{ at } x = X_k, y = Y_k$$

which yields combined the system of equations:

$$\Phi_i = \alpha_1 + \alpha_2 X_i + \alpha_3 Y_i$$

$$\Phi_j = \alpha_1 + \alpha_2 X_j + \alpha_3 Y_j$$

$$\Phi_k = \alpha_1 + \alpha_2 X_k + \alpha_3 Y_k$$

that again can be solved for  $\alpha_1, \alpha_2$  and  $\alpha_3$ .

Inserting in the original interpolation equations leads to:

$$\phi = N_i \Phi_i + N_j \Phi_j + N_k \Phi_k.$$

where the  $N$  are now the shape function for the respective node:

$$N_i = \frac{1}{2A_\Delta} [a_i + b_i x + c_i y] \quad (\text{A.1})$$

$$N_j = \frac{1}{2A_\Delta} [a_j + b_j x + c_j y] \quad (\text{A.2})$$

$$N_k = \frac{1}{2A_\Delta} [a_k + b_k x + c_k y] \quad (\text{A.3})$$

with

$$\begin{aligned} a_i &= X_j Y_k - X_k Y_j, & b_i &= Y_j - Y_k, & c_i &= X_k - X_j \\ a_j &= X_k Y_i - X_i Y_k, & b_j &= Y_k - Y_i, & c_j &= X_i - X_k \\ a_k &= X_i Y_j - X_j Y_i, & b_k &= Y_i - Y_j, & c_k &= X_j - X_i \end{aligned}$$

and  $A_\Delta$  the area of the triangle.

Some remarks to the shape functions: At each point in an element, the sum of the values of the shape functions is one. Hence, the value of each shape function on its own node is one, while it's zero at each other node of the element (leading to very sparse matrices describing the operators, as shown later). Between these nodes the function interpolates linearly. Figure A.1 shows the value of the basis function connected to the first node over the triangle.

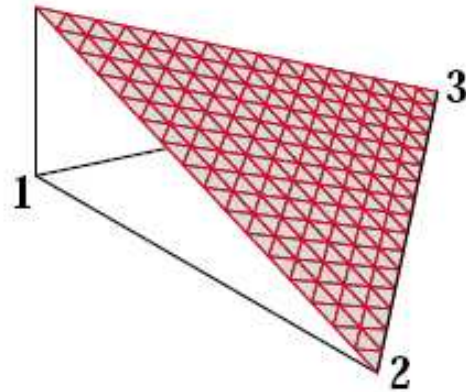


**Figure A.1:** Value of the basis function of the first node over the triangle, taken from [41]

This representation of the shape functions is also called 'area coordinates', because their values give the ratio of the area of a subtriangular region to the area of the complete triangle (see figure A.2). The area coordinate  $L_1$  is the ratio of the shaded area to the total area:

$$L_1 = \frac{A_1}{A_\Delta}$$

The same applies for the areas  $A_2$  and  $A_3$ , leading to  $L_1 = N_1$ ,  $L_2 = N_2$  and  $L_3 = N_3$ .

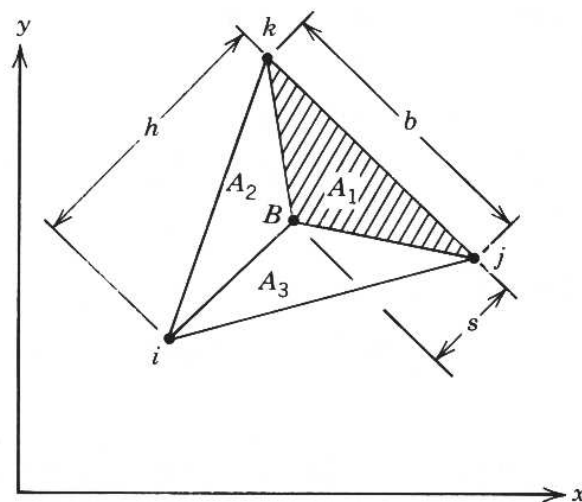


**Figure A.2:** Area coordinates, taken from [21].

For the derivatives of  $\phi$  holds

$$\frac{\partial \phi}{\partial x} = \frac{\partial N_i}{\partial x} \Phi_i + \frac{\partial N_j}{\partial x} \Phi_j + \frac{\partial N_k}{\partial x} \Phi_k \quad (\text{A.4})$$

$$\frac{\partial \phi}{\partial y} = \frac{\partial N_i}{\partial y} \Phi_i + \frac{\partial N_j}{\partial y} \Phi_j + \frac{\partial N_k}{\partial y} \Phi_k. \quad (\text{A.5})$$

The partial derivatives in global coordinates can be expressed by

$$\begin{pmatrix} \frac{\partial N^i}{\partial x} \\ \frac{\partial N^i}{\partial y} \end{pmatrix} = J^{-1} \begin{pmatrix} \frac{\partial N^i}{\partial L_1} \\ \frac{\partial N^i}{\partial L_2} \end{pmatrix} \quad (\text{A.6})$$

$$\text{with } J = \begin{pmatrix} \frac{\partial x}{\partial L_1} & \frac{\partial y}{\partial L_1} \\ \frac{\partial x}{\partial L_2} & \frac{\partial y}{\partial L_2} \end{pmatrix}.$$

The third coordinate  $L_3$  does not appear because it is not independent of the others:  $L_3 = 1 - L_2 - L_1$ . In such a triangle, the Jacobian is constant and reads

$$J = \begin{pmatrix} c_j & -b_j \\ -c_i & b_i \end{pmatrix}$$

with  $\det J = 2A_\Delta$ .

The derivatives with respect to  $x$  and  $y$  read

$$\frac{\partial N_\beta}{\partial x} = \frac{b_\beta}{2A_\Delta}, \quad \frac{\partial N_\beta}{\partial y} = \frac{c_\beta}{2A_\Delta}, \quad \beta = i, j, k \quad (\text{A.7})$$

Equation A.7 shows, that the representation of a derivative is one polynomial degree smaller than the representation of the quantity itself. As second order derivatives appear in the problem formulation, the need for approximations of second order arises. The second derivative is then constant in an element (zeroth order representation).

A second-order triangle (also called quadratic triangle) has six nodes instead of three: additionally to the three vertex nodes, three nodes on the midpoints of the edges get own shape functions and values for the solution  $u_h$ . Figure A.3 shows both kinds of shape functions.

The shape functions of the quadratic triangle fulfill the same conditions as these for the linear one, but the interpolation inside an element is now quadratically. In the code, all the triangular elements have straight edges, although this is not

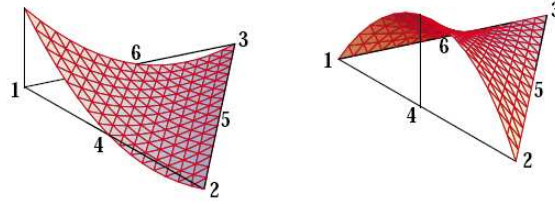


**Figure A.3:** Basis functions in the quadratic triangle, taken from [41]

mandatory. Indeed, it is possible to use triangles with curved boundaries to match better to the geometry if necessary. The only difficulty arising is that the determinant of the Jacobian connected with the mapping to the coordinate system of the finite element is not constant anymore.

The shape functions read:

$$N_1 = L_1(2L_1 - 1) \quad (\text{A.8})$$

$$N_2 = 4L_1L_2 \quad (\text{A.9})$$

$$N_3 = L_2(2L_2 - 1) \quad (\text{A.10})$$

$$N_4 = 4L_2L_3 \quad (\text{A.11})$$

$$N_5 = L_3(2L_3 - 1) \quad (\text{A.12})$$

$$N_6 = 4L_3L_1 \quad (\text{A.13})$$

The derivatives of the shape functions can be computed with the same relation as above.

### A.1.2 Solving partial differential equations

One approach to solve a partial differential equation with the FEM is the weighted residual method. Consider the equation below (which is similar to those equations appearing in the code):

$$c_1 \Delta u + c_2 \nabla u = -q$$

where  $c_1$  and  $c_2$  are for reasons of simplicity constant coefficients. The real solution  $u$  is now expressed as approximate solution  $u_h$  and in the terminology of FEM  $q$  is a load. Hence

$$c_1 \Delta u_h + c_2 \nabla u_h + q = R \neq 0$$

as in general the residual will not be zero. The residual is now multiplied by a weighting function  $W$  and integrated over the whole domain and is required to vanish:

$$\int W \cdot R \, dA = 0$$

There are many possible choices for the weighting functions, the most popular is to chose the same function that we used to express  $u$  by its approximate values  $u_h$  (shape functions),  $W = N$ . This choice of weighting functions is called Galerkin's method. These integrals can be evaluated elementwise, the complete solution being the summation of all element contributions. For one element with all quantities and operators in finite element representation, the equation reads:

$$\int_e \mathbf{N}^T \cdot (c_1 \Delta \mathbf{u}_h + c_2 \nabla \mathbf{u}_h + \mathbf{q}) dA = 0,$$

where  $\mathbf{N}^T$  is the transposed of the  $1 \times 6$  vector containing the shape functions  $N_1$  to  $N_6$  of the quadratic triangle. The second derivative can be integrated partially, leading to

$$\int_e \mathbf{N}^T \cdot (\Delta \mathbf{u}_h) dA = \left( \int_e \mathbf{N}^T \cdot \mathbf{n} \cdot \nabla \mathbf{N} d\Gamma \right) \mathbf{u}_h - \left( \int_e \left( \frac{\partial \mathbf{N}^T}{\partial x} \frac{\partial \mathbf{N}}{\partial x} + \frac{\partial \mathbf{N}^T}{\partial y} \frac{\partial \mathbf{N}}{\partial y} \right) dA \right) \mathbf{u}_h \quad (\text{A.14})$$

where the first integral is over the boundary  $\partial\Gamma$  of the element and  $\mathbf{n} \cdot \nabla$  is the normal derivative. As the values of the unknown  $u_h$  are unique on a node, this contribution cancels for triangles in the inner of the domain. Only elements that have edges on computational domain contribute to this integral, if a value for the normal derivative is prescribed. Note that this representation leads to  $k \times k$  matrices for the operators and and  $k \times 1$  vector for the load term, where  $k$  is the number of nodes per element. The total equation for one element reads

$$R = \left( \int_e c_1 (\nabla \mathbf{N}^T \nabla \mathbf{N}) dA \right) \mathbf{u}_h + \int_e c_2 \mathbf{N}^T \nabla \mathbf{N} dA + \int_e \mathbf{q} \mathbf{N}^T dA = 0.$$

The evaluation of these integrals can be done analytically for simple cases or numerically via Gauss integration, as it is done in the code. Numerical integration converts the integrals to a sum of weighted contributions, evaluated at special sampling points:

$$\int_{A_\Delta} f(x, y) \, dA = \int \int \frac{1}{\det J} g(L_1, L_2) \, dL_1 dL_2 = \sum_{i=1}^n g(L_{1i}, L_{2i}) w_i$$

where  $n$  is the number of sampling points of an element and the  $w_i$  their associated weight. The number of sampling points must match at least the largest sum of the powers of  $L1$  and  $L2$  to integrate exactly.

The contributions of all elements are put together in a  $n_p \times n_p$  matrix for the operators, where  $n_p$  is the number of grid points, and a  $n_p \times 1$  vector for the load, the position of the contributions depending on the global numbering of the nodes of an element. This process is called assembling. Each row is the equation for one grid point.

### A.1.3 Boundary conditions

As the problem dealt with is a second order partial differential equation, there must be boundary conditions specified on a curve  $\Gamma$  enclosing the computational domain. The most common boundary conditions are those of Dirichlet, Neumann or Robin type. In the first case, values of the solution on the boundary are given, for example  $u_i = b_i$ , where the  $i$  denote the indices of points on the boundary. This is implemented by substituting the respective rows associated with boundary nodes by zeros, except where the column number equals the number of the boundary node: the entry there is one. When now substituting the corresponding entry of the right hand side (load vector), the equation for a boundary point reduces to  $u_i = b_i$  as intended and there is no need to deal with the interelement boundary term mentioned above.

Neumann boundary conditions prescribe values of the normal derivative of the solution,  $\mathbf{n} \cdot \nabla u_i = b_i$ . They are slightly more difficult to implement. Equation A.14 already contains the formulation of the boundary condition:

$$\left( \int_e \mathbf{N}^T \cdot \mathbf{n} \cdot \nabla \mathbf{N} d\Gamma \right) \mathbf{u}_i.$$

The expression is simply substituted by the known values of the normal derivative:

$$\left( \int_e \mathbf{N}^T \cdot \mathbf{N} d\Gamma \right) \mathbf{b}_i.$$

The integration is now over a line element instead of an area. In principle, the same mechanisms apply, only the shape functions and the numerical integration differ. The resulting matrix (with only entries at indices that are connected to the boundary) is then added to the right hand side of the equation (load vector). Robin boundary conditions are a combination of Dirichlet and Neumann bound-

ary conditions:

$$\mathbf{n} \cdot \nabla N d\Gamma = c\mathbf{u}_i + \mathbf{b}_i \text{ on } \Gamma.$$

The additional term is treated similar to the Neumann term, but the matrix-vector-multiplication cannot be executed as the  $u_i$  are unknown. So the matrix  $(\int_e N^T \cdot N d\Gamma)$  has to be added to the matrix describing all the operators on the left hand side. In the code, the boundary condition imposed is similar to the Robin type, but it is non-local.

#### A.1.4 Time-dependent problems

The time-dependent equations that appear in the code have the form

$$\lambda \frac{\partial u}{\partial t} + c_1 \Delta u + c_2 \nabla u + q = 0. \quad (\text{A.15})$$

The only new term is  $\lambda \frac{\partial u}{\partial t}$ . The term is treated in the same way as described above, leading to an expression for the contribution to the residual:

$$R_\lambda = \int_e \lambda (\mathbf{N}^T \mathbf{N} dA) \dot{\mathbf{u}}$$

The matrix  $N^T N$  is called mass matrix due to its origin in engineering applications. The temporal discretization is done with finite differences. Given the function  $u(t)$  and the time interval  $[t_1, t_2]$ , one can use the mean value theorem. It states that there is a value  $t_p$  of  $t$  for that holds

$$\mathbf{u}(t_2) - \mathbf{u}(t_1) = (t_2 - t_1) \frac{d\mathbf{u}}{dt}(t_p). \quad (\text{A.16})$$

Approximating  $\mathbf{u}(t_1)$  linearly and inserting leads to

$$\mathbf{u}(t_p) = (1 - \theta)\mathbf{u}(t_1) + \theta\mathbf{u}(t_2), \quad (\text{A.17})$$

with  $\theta$  defined as  $\theta = \frac{t_p - t_1}{\Delta t}$ . The value of  $\theta$  defines the way the equations is solved.  $\theta = 0$  is called forward difference method and solves the system explicitly, i.e. the solution for the time  $t_2$  is gained by multiplying the operator matrix with the solution at the time  $t_1$ . Implicit methods have  $\theta > 0$  and at every time step a matrix equation has to be solved. Explicit methods are constrained concerning the maximal allowable time step whereas implicit methods do not suffer from this condition (however, the solution gets inaccurate for too large time steps). In the code, all equations are solved implicitly but they are coupled with an explicit

time scheme (leap frog).

### A.1.5 Patch recovery

In the finite element approach of this work, any quantity is represented by bi-quadratic (or bi-linear) functions. When formulating derivatives these quantities, one degree in approximation order is lost, so that a quantity that was represented by six (three) nodes per element earlier, has now only three nodes (one node). In the case of quadratic triangles, these values are not unique at nodes that are shared by several triangles, as the shape functions are by construction only  $C_0$ -continuous, so that in different elements different values at the shared node can appear. The most obvious way to deal with this problem is to calculate the derivatives in each element separately and build the arithmetic or area weighted mean of all participating nodes. Indeed, this is a often followed way. Unfortunately, we lose an order in accuracy and especially in vicinity to domain borders the results are very unsatisfactory. A popular way of keeping the same representation order and gaining better results are recovery methods. The most common is the so-called ZZ-patch-recovery-technique ([59]). The derivatives are not calculated elementwise but in an assembly of elements, a so called patch (see figure A.4). Every internal node can be assigned a patch and the greater this patch is cho-

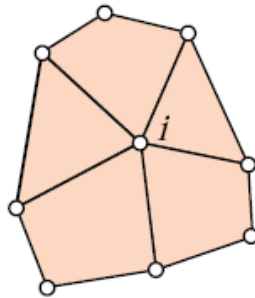


**Figure A.4:** Patch on which a least squares fit is calculated

sen, the more accurate the solution. Over this patch a least-squares smoothing is carried out, which shall be shown on the simple example of bilinear triangle elements. The finite element approximation is denoted by  $\mathbf{u}_h$ , the exact solution by  $\mathbf{u}$  and the nodal values by  $\bar{\mathbf{u}}$ .  $\mathbf{u}_h$  is obtained by the standard Galerkin procedure and reads:

$$\mathbf{u}_h = \mathbf{N}\bar{\mathbf{u}}.$$

The gradients are

$$\sigma_{\mathbf{h}} = D \mathbf{u}_{\mathbf{h}},$$

where  $D$  denotes the differential operator matrix. Of course, the  $\sigma$  have no interelement continuity (and as said above, even for quadratic elements this would in general not be given). The aim is now to find  $\sigma^*$ , the smoothed and continuous gradient field, defined by the same basis functions as  $\mathbf{u}$  and nodal coefficients  $\bar{\sigma}^*$ .

$$\sigma^* = \mathbf{N} \bar{\sigma}^*.$$

These nodal coefficients are assumed to belong to a polynomial expansion  $\sigma_{\mathbf{P}}^*$  of the same order as in the basis functions (one for linear triangles and two for quadratic ones) and which is valid over the above defined element patch:

$$\sigma_{\mathbf{P}}^* = \mathbf{P} \mathbf{a}$$

where  $\mathbf{a}$  are the unknown coefficients to determine and  $\mathbf{P}$  contains the appropriate polynomial expansion terms. For linear triangles,  $\mathbf{P}$  reads

$$\mathbf{P} = [1 \ x \ y]$$

while quadratic ones would need six entries of quadratic order. The least-squares fit works by minimizing the following expression:

$$\begin{aligned} R &= \sum_{i=1}^n (\sigma_{\mathbf{h}}(x_i, y_i) - \sigma_{\mathbf{P}}^*(x_i, y_i))^2 \\ &= \sum_{i=1}^n (\sigma_{\mathbf{h}}(x_i, y_i) - \mathbf{P}(x_i, y_i) * \mathbf{a})^2 \end{aligned}$$

where  $x_i$  and  $y_i$  are the coordinates of a group of sampling points of the element patch and  $\mathbf{a}$  the corresponding coefficients to the polynomial expansion. These sampling points (Gauss points, see [59]) lead to superconvergent nodal values, i.e. a convergence of  $O(h^4)$ . It follows

$$\sum_{i=1}^n \mathbf{P}(x_i, y_i)^T \mathbf{P}(x_i, y_i) * \mathbf{a} = \sum_{i=1}^n \mathbf{P}(x_i, y_i)^T \sigma_{\mathbf{h}}$$

or, in matrix form:

$$\mathbf{a} = \mathbf{A}^{-1} * \mathbf{b}$$

where

$$\mathbf{A} = \sum_{i=1}^n \mathbf{P}(x_i, y_i)^T \mathbf{P}(\mathbf{x}_i, \mathbf{y}_i), \mathbf{b} = \sum_{i=1}^n \mathbf{P}(x_i, y_i)^T \sigma_{\mathbf{h}}.$$

The calculation is carried out only for vertex nodes on a constant grid, so the matrix  $\mathbf{A}$  does not change for a given patch and has to be computed only once (which is quite inexpensive when solving time-dependent problems). For midside and boundary nodes, the values are calculated with the approximation of the respective patches. As these nodes can have several contributions, there has to be an averaging.

## A.2 Contouring

Two different contouring methods are implemented for the scalar quantities in the code. Let  $\Psi$  be the scalar field and  $\Psi_c$  the value of the contour one is interested in. The first one searches for an arbitrary point in the scalar field at which the condition  $(\Psi - \Psi_c)^2 < \epsilon$  holds. Starting from that point, the contour is traced from element to element, calculating the point on the element boundary at which the contour intersects ([58]). In this way, open and closed field lines can be distinguished. For finding the separatrix, saddle points of  $\Psi$  are determined. Usually, there are one or two saddle points in a computational domain. The x-point with the  $\Psi$  value closer to that of the magnetic axis belongs to the real separatrix within which all field lines are closed. The second contouring routine uses the condition that flux surfaces are uniquely defined within the separatrix. Any vertical or horizontal cut through the function  $\Psi - \Psi_c$  within the plasma region has exactly 2 roots. Many of these cuts are done and the identified positions of the roots are ordered, resulting in coordinates of a contour. As the mesh remains constant during the calculations, the time consuming parts of the computation can be done once in advance for both contouring routines.

## A.3 Slip Motion Condition

The Slip Motion Condition reads after temporal integration

$$\nabla \times (\mathbf{v} \times \nabla \phi) = 0$$

Inserting the expression for the velocity  $\mathbf{v} = -R^2 \nabla \phi \times \nabla \eta$  on the left hand side results in

$$\begin{aligned} \nabla \times ((-R^2 \nabla \phi \times \nabla \eta) \times \nabla \phi) &= 0 \\ -\nabla \times \left( \underbrace{(\nabla \phi \cdot \nabla \eta)}_{=0} \cdot R^2 \nabla \phi - \nabla \eta \right) &\equiv 0 \end{aligned}$$

## A.4 Vorticity equation

The vorticity is defined as

$$\Omega = R \mathbf{e}_\phi \cdot \nabla \times \mathbf{v}.$$

Applying the operation  $R \mathbf{e}_\phi \cdot \nabla \times$  on the force balance equation

$$\rho \frac{d\mathbf{v}}{dt} - \mathbf{J} \times \mathbf{B} + \nabla p = 0 \quad (\text{A.18})$$

leads to an equation with  $\Omega$  as evolving variable. As a first step, eq. (A.18) is transformed, using the convective derivative:

$$\frac{\partial \mathbf{v}}{\partial t} + (\mathbf{v} \cdot \nabla) \mathbf{v} = \frac{1}{\rho} (\mathbf{J} \times \mathbf{B} - \nabla p).$$

With the operation described above, the equation reads

$$\frac{\partial \Omega}{\partial t} + Re_\phi \nabla \times ((\mathbf{v} \cdot \nabla) \mathbf{v}) = Re_\phi \nabla \times \left( \frac{1}{\rho} (\mathbf{J} \times \mathbf{B} - \nabla p) \right)$$

It can be shown that

$$Re_\phi \nabla \times ((\mathbf{v} \cdot \nabla) \mathbf{v}) = Re_\phi \nabla \times \left( \frac{\nabla v^2}{2} + \mathbf{v} \times (\nabla \times \mathbf{v}) \right) = v \nabla \Omega.$$

The right hand side reads

$$Re_\phi \left[ \nabla \frac{1}{\rho} \times (\mathbf{J} \times \mathbf{B} - \nabla p) + \frac{1}{\rho} \nabla \times (\mathbf{J} \times \mathbf{B}) - \underbrace{\frac{1}{\rho} \nabla \times \nabla p}_{=0} \right].$$

It's useful to distinguish two cases:

1.  $\beta = 0$  Any terms involving the pressure vanish. Furthermore, there is no contribution from poloidal currents or the toroidal magnetic field, if for the density holds  $\rho = \frac{\text{const}}{R^2}$ , as the following calculation shows:

$$\begin{aligned}
& R \cdot \mathbf{e}_\phi [\nabla \times (1/\rho \cdot (\mathbf{J}_p \times \mathbf{B}_\phi))] \\
&= R \cdot \mathbf{e}_\phi [\nabla 1/\rho \times (\mathbf{J}_p \times \mathbf{B}_\phi) + 1/\rho \cdot \nabla \times (\mathbf{J}_p \times \mathbf{B}_\phi)] \\
&= R \cdot \mathbf{e}_\phi \left[ \nabla 1/\rho \times -j_z B_\phi \mathbf{e}_R + j_R B_\phi \mathbf{e}_z + 1/\rho \cdot \nabla \times \left( \left( -\frac{1}{R} \mathbf{e}_\phi \times \nabla F \right) \times \frac{F}{R} \mathbf{e}_\phi \right) \right] \\
&= R \cdot \mathbf{e}_\phi \left[ \nabla 1/\rho \times \left( -\frac{1}{2R^2} \frac{\partial F^2}{\partial R} - \frac{1}{2R^2} \frac{\partial F^2}{\partial z} + 1/\rho \cdot \nabla \times \left( -\frac{F \nabla F}{R^2} \mathbf{e}_\phi \right) \right) \right] \\
&= R \cdot \mathbf{e}_\phi \left[ \nabla 1/\rho \times \left( -\frac{1}{2R^2} \nabla F^2 + 1/\rho \cdot \left( \frac{1}{R^3} \vec{e}_R \times \nabla F^2 \right) \right) \right] \\
&\quad \text{Inserting the expression for } \rho \text{ results in} \\
&= \frac{1}{\text{const.}} \cdot R \cdot \mathbf{e}_\phi \left[ \frac{1}{R} \frac{\partial F^2}{\partial z} \mathbf{e}_\phi - \frac{1}{R} \frac{\partial F^2}{\partial z} \mathbf{e}_\phi \right] \\
&= 0
\end{aligned}$$

The remaining terms are

$$r.h.s. = R e_\phi \left( \nabla \frac{1}{\rho} \times (\mathbf{J}_\phi \times \mathbf{B}_p) + \frac{1}{\rho} \times \nabla \times (\mathbf{J}_\phi \times \mathbf{B}_p) \right)$$

Using the identity  $\nabla \times (\mathbf{J}_\phi \times \mathbf{B}_p) = \mathbf{B}_p R \nabla \frac{j_\phi}{R}$ , where  $j_\phi = \mathbf{e}_\phi \cdot \mathbf{J}$ , and inserting again the expression for the density leads to:

$$r.h.s. = \frac{R^4}{\text{const}} \left( \mathbf{B}_p \cdot \nabla \left( \frac{j_\phi}{R} \right) + 2 \frac{1}{R^2} j_\phi B_R \right). \quad (\text{A.19})$$

2.  $\beta \neq 0$

The density and the pressure are now arbitrary functions of  $\Psi$ . The left hand side is transformed in the same way as in the previous case. For the right hand side, no separation in poloidal and toroidal contributions is performed. Instead, the following identities are used:

$$\begin{aligned}
r.h.s. &= Re_\phi \left[ \underbrace{\frac{\nabla}{\rho} \times (\mathbf{J} \times \mathbf{B} - \nabla p)}_{=0} + \underbrace{\frac{1}{\rho} \nabla \times (\mathbf{J} \times \mathbf{B})}_{=\frac{1}{\rho} (\mathbf{B} R \nabla \frac{j_\phi}{R} - \frac{2 F F'}{\mu_0 R^3} \frac{\partial \Psi}{\partial z})} - \underbrace{\frac{1}{\rho} \nabla \times \nabla p}_{=0} \right] \\
r.h.s. &= \frac{1}{\rho} \left( \mathbf{B} R^2 \nabla \frac{j_\phi}{R} - 2 \frac{F F'}{\mu_0 R^2} \frac{\partial \Psi}{\partial z} \right). \tag{A.20}
\end{aligned}$$

For  $\beta = 0$ , the equations (A.19) and (A.20) are the same.

## A.5 Resistance and inductance of the PSL

The resistance can be calculated

$$\mathcal{R} = \frac{l}{\sigma A} = \frac{2 \cdot 2\pi R_{PSL}}{\sigma A}, \tag{A.21}$$

where  $l$  denotes the PSL circumference,  $A$  the cross area of one leg and  $R_{PSL}$  the radial center of the PSL defined as

$$R_{PSL} = \frac{\int R dA}{\int dA}.$$

The inductance is twice the sum of the self-inductance  $L_c$  and the (negative) mutual inductance

$$L = 2 \cdot (L_c - M) = 2 \cdot \mu_0 R_{PSL} \log \left( \frac{R_{PSL}}{r_{PSL}} \right) - 2 \cdot \frac{\mu_0}{4\pi} \oint_1 \oint_2 \frac{\mathbf{ds}_1 \cdot \mathbf{ds}_2}{r_{12}}, \tag{A.22}$$

where  $r_{PSL}$  is the radius of a circle with the same area as the cross section of one PSL leg,  $\mathbf{ds}_1$  and  $\mathbf{ds}_2$  are line elements on the upper and lower PSL and  $r_{12}$  is the distance between these line elements. The mutual inductance can simply be subtracted because the current in the upper PSL is the same as the current of the lower PSL with opposite sign.

## A.6 Estimate of required computer resources for building up a data base of VDE growth rates

If only a linear growth rate is of interest, as it would be for a data bank similar to the one already existing at ASDEX Upgrade (FP), it is sufficient to run the code during the linear stage of the instability. The growth rate can be determined from the observed displacement of the plasma current barycentre (the most accurately monitored quantity), using essentially the equation  $\tau = \gamma^{-1} \log \frac{z(\tau) - z_0}{\delta z}$ , where  $z, z_0$  and  $\delta z$  are the instantaneous position, the equilibrium position and the amplitude of the perturbation, respectively. Initial equilibria are calculated by a separate code with a different grid and both the uncertainty of the equilibrium position and the amplitude of the perturbation will be proportional to the grid spacing. Assuming this to be the major source of uncertainty, it follows that the relative error in  $\gamma$  will be proportional to  $\log \frac{z(\tau) - z_0}{\delta z}$ . The request for a certain maximum error implies to carry calculations to a fixed value of the argument, i.e. to a fixed ratio of the displacement to grid size - independently of the growth rate. As the time step is determined by the CFL condition, and hence does not depend on the growth rate, faster growing modes would require fewer time steps. However, faster growth rates imply the need for a finer grid to resolve the skin layers in the conductor and the plasma boundary. This allows on the one hand to reduce the interval of  $z(\tau) - z_0$  over which calculations need to be executed, but enhances of course the numerical effort of each individual step. Overall, the effect of growth rate on the needed computing time is modest. We can therefore estimate the total CPU hours requirement from a run with modest growth rate and corresponding resolution which takes about 4 hours to sufficient convergence in single core use of a computer. Arguing that by relatively simple programming, the parallel execution of cases on the individual cores of a node should be possible, a 2500 case data base (considered necessary to span the interesting operating regime of AUG equilibria) should be computable within a few thousand CPU hours.



# Bibliography

- [1] <http://www.worldenergy.org/>
- [2] <http://www.alaskajohn.com/physics/charts/>
- [3] Rebhan, Salat (1976)  
"Stability of Tokamaks with respect to slip motions",  
*Nuclear Fusion* 16, 1976, pp. 805-815
- [4] Rebhan (1975)  
"Stability boundaries of tokamaks with respect to rigid displacements",  
*Nuclear Fusion* 15, 1975, pp. 277-285
- [5] Laval, Pellat, Soule (1976),  
"Hydromagnetic Stability of a current-carrying pinch with noncircular cross section",  
*Nuclear Fusion* 16, 1976, pp. 835-845
- [6] R.R. Khayrutdinov and V.E. Lukash (1993),  
"Studies of Plasma Equilibrium and Transport in a Tokamak Fusion Device with the Inverse-Variable Technique",  
*Journal of Computational Physics*, 109 , pp. 193-201
- [7] Bernstein et al. (1957)  
"An energy principle for hydromagnetic stability problems",  
*Proceedings of the royal Society of London, Series A, Mathematical and Physical Sciences*, Vol. 244, No. 1236, pp. 17-40
- [8] Karl Lackner (1976)  
"Computation of ideal MHD equilibria",  
*Computer Physics Communications* 12, pp. 33-44
- [9] Jeffrey P. Freidberg (1987)  
"Ideal Magnetohydrodynamics",  
*Plenum Press*, New York, First Edition

- 
- [10] John Wesson (1987)  
"Tokamaks",  
*Clarendon Press, Oxford, First Edition*
- [11] S.C. Jardin, N. Pomphrey, J. DeLucia (1986)  
"Dynamic Modeling of transport and positional control of tokamaks",  
*Journal of Computational Physics 66*, p. 481
- [12] T.J.M. Boyd, J.J. Sanderson "The Physics of Plasmas" *Cambridge University Press (2003)*
- [13] John Wesson,  
"Hydromagnetic Stability of Tokamaks",  
*Nuclear Fusion 18 (1976)*, p. 87
- [14] V.S. Mukhatov, V.D. Shafranov,  
"Plasma Equilibrium in a Tokamak"  
*Nuclear Fusion 11 (1971)*, p. 605
- [15] A. Hassanein, T. Sizyuk and M. Ulrickson  
"Vertical displacement events: A serious concern in future ITER operation"  
*Fusion Engineering and Design 83 (2008)*, p. 1020
- [16] Täteo Kajita and Kenro Miyamoto,  
"Stress Distributions of Coils for Toroidal Magnetic Field"  
*Jpn. J. Appl. Phys. 15 (1976) pp. 1965-1971*
- [17] John D. Jackson (1982)  
"Klassische Elektrodynamik",  
*Walter de Gruyter, Berlin; New York, Zweite verb. Auflage*
- [18] Karl Lackner (2007), IPP, private Kommunikation
- [19] Jacques Blum (1989)  
"Numerical simulation and optimal control in plasma physics",  
*John Wiley and Sons, New York, First Edition*
- [20] O.C. Zienkiewicz (1975)  
"Methode der finiten Elemente",  
*Carl Hanser Verlag, München, Erste Auflage*
- [21] Larry J. Segerlind (1984)  
"Applied Finite Element Analysis",

*John Wiley and Sons, New York, Second Edition*

- [22] T.J.R. Hughes (1987)  
"The Finite Element Method: Linear Static and Dynamic Finite Element Analysis",  
*Prentice-Hall, Inc.a*
- [23] I. Bronstein, K. Semendjajew, W. Hackbusch (1996)  
"Teubner Taschenbuch der Mathematik",  
*Teubner Verlag, Stuttgart*
- [24] Asdex Upgrade Ringbuch, technical documentation,  
<http://www.aug.ipp.mpg.de/documentation/bin/view/Main/TOC>
- [25] "Partial Differential Equation Toolbox - User's Guide "  
*Mathworks, Natick (USA), 2010*
- [26] "Curve Fitting Toolbox 3 - User's Guide " *Mathworks, Natick (USA), 2010*
- [27] <http://www.aug.ipp.mpg.de/documentation/bin/view/...>  
VacuumVessel/PassiveStabilisingLoop
- [28] <http://www.ipp.mpg.de/ippcms/eng/pr/exptypen/tokamak/index.html>
- [29] <http://www.answers.com/topic/pinch-effect-1>
- [30] Hering, Martin, Stohrer (1992)  
"Physik für Ingenieure",  
*VDI Verlag, Düsseldorf, Vierte verbesserte Auflage*
- [31] W.D. d'Haeseleer, W.N.G. Hitchon, J.D. Callen, J.L. Shohet (1991)  
"Flux Coordinates and Magnetic Field Structure",  
*Springer Verlag, Berlin, First Edition*
- [32] A. Könies, K. Krieger u.v.a. (2004)  
"Summer University for Plasma Physics",  
*Max-Planck-Institut für Plasmaphysik, Garching*
- [33] Thomas Neukirch,  
[http://www-solar.mcs.st-and.ac.uk/sws10/Presentations/neukirch\\_solaire4.pdf](http://www-solar.mcs.st-and.ac.uk/sws10/Presentations/neukirch_solaire4.pdf)
- [34] Roberto Bilato, IPP, private Kommunikation
- [35] Wolfgang Schneider, IPP, private Kommunikation

- 
- [36] A. Portone, EFDA,  
email: alfredo.portone@tech.efda.org
- [37] Karl Lackner,  
Lecture Notes
- [38] Aiba, N. et al.,  
"Effects of 'Sharpness' of the Plasma Cross-section on the MHD Stability of Tokamak Edge Plasmas",  
*Nuclear Fusion*, vol.47, no.4, 2007, p.297-304
- [39] Christian Wigger, diploma thesis  
"Entwicklung eines Codes zum Test von Gleichgewichten gegen axisymmetrische Instabilitäten im Tokamak"
- [40] B. Braams,  
"Computational studies in tokamak equilibrium and transport",  
Ruksuniveriteit te Utrecht, 1986
- [41] Introduction to Finite Element Methods, University of Colorado at Boulder,  
<http://www.colorado.edu/engineering/CAS/courses.d/IFEM.d/>
- [42] Garching Equilibrium Code, K. Lackner, Peter Martin and others
- [43] McCarthy, P.J., Martin, P., Schneider, W.,  
"The CLISTE interpretive equilibrium code",  
Technical Report IPP 5/85, IPP, Garching, Germany (1999)
- [44] K. Lackner, A.B. McMahon,  
"Numerical study of displacement instability in elongated Tokamak",  
*Nuclear Fusion* 14 (1974), pp. 575-577
- [45] Weston M. Stacey,  
"Fusion Plasma Physics",  
*Wiley VCH Verlag* (2005)
- [46] P. Merkel, M. Sempf,  
"Feedback Stabilization of Resistive Wall Modes in the Presence of Multiply Connected Wall Structures",  
21st IAEA Fusion Energy Conference 2006, Chengdu, China, paper TH/P3-8, 2006
- [47] Sibylle Guenter, IPP, Vorlesungsskript "Plasma Physik II: Toroidaler Ein-

schluss”

- [48] O. Gruber, K.Lackner, G. Pautasso, U. Seidel, B.Streibl,  
”Vertical Displacement Events and Halo currents”,  
*Plasma Phys. Control. Fusion* 35 (1993) B191-B204
- [49] O. Gruber, private communication
- [50] R. Courant, K. Friedrichs and H. Lewy  
”Über die partiellen Differenzgleichungen der mathematischen Physik”,  
*Mathematische Annalen* (1928), vol. 100, no. 1, p. 32
- [51] Ren Shen-Ming and Yu Guo-Yang,  
”Reduced MHD equations in toroidal geometry”  
*Chin. Phys. Letter* (2001), p. 556
- [52] H.R. Strauss,  
”Finite Aspect-ratio MHD Equations for Tokamaks”  
*Nuclear Fusion* 23 (1982), p. 649
- [53] B. Lipschultz, S.C. Prager, A.M.M. Todd, J. Delucia,  
”Axisymmetric Instabilty in a Non-curcular Tokamak: Experiment and The-  
ory”,  
*Nuclear Fusion* 20 (1980), p. 683
- [54] K. Lackner,  
”Computation of Ideal MHD Equilibria”,  
*Computer Physics Communications* 12 (1976), p.33
- [55] Jean Donea,  
”Recent Advances in Computational Methods for Steady and Transient  
Transport Problems”,  
*Nuclear Engineering and Design* 80 (1984), p.141
- [56] Sebastian Jund, Stephanie Salmon  
”Arbitrary High-Order Finite Element Schemes And High-Order Mass  
Lumping”  
*Int. J. Appl. Math. Comput. Sci.* 17 (2007)
- [57] W.H. Press, S.A. Teukolsky, W.T. Vetterling, B.P. Flannery  
”Numerical Recipes in Fortran”  
*Cambridge University Press, Second Edition* (1992)

- 
- [58] S. Alfonzetti  
"An N-Dimensional Algorithm to Draw contour Lines over Triangular Elements"  
*IEEE Transactions on Magnetics* 32 (1996), p. 1473
- [59] O.C. Zienkiewicz and J.Z. Zhu,  
"The superconvergent patch recovery and a posteriori error estimates part 1: the recovery technique",  
*Int. Journal for numerical methods in engineering* 33 (1992) p. 1331
- [60] J.Y. Favez, R.R. Khayrutdinov, J.B. Lister and V.E. Lukash,  
"Comparing TCV experimental VDE responses with DINA code simulations"  
*Plasma Phys. Control. Fusion* (2002), p. 171

# Danksagung

An dieser Stelle möchte ich denjenigen persönlich danken, die mir bei dieser Arbeit geholfen haben, sei es direkt durch Rat und Tat oder indirekt durch ihren Zuspruch und ihre Inspiration.

An erster Stelle danke ich meinem Betreuer Karl Lackner, der mich mit viel Geduld und seinem unerschöpflichen Wissen leitete, viele Ideen einbrachte und immer Zeit und freundliche Worte für mich fand.

Ich danke Sibylle Günter für die Betreuung meiner Arbeit, ihre Nachsicht und Freundlichkeit. Ich bin mir fast sicher, dass sie meinen fragwürdigen Sinn für Humor rückblickend als sehr liebenswürdig empfinden wird.

Für all die Berechnungen, Ratschläge und Informationen, die sie mir gaben, danke ich Wolfgang Schneider, Paddy McCarthy, Otto Gruber und insbesondere Peter Martin.

Meinen Freunden und Kollegen Matthias Hölzl, Klaus Reuter, Rainer "Rainsch" Piechoczek, Hagen Langhuth, Johannes Griefhammer, Anja Bauer und Gabriele Daube danke ich für zahllose Besuche in Kantinen, Mensen und Cafeterien, die hilfreichen Gespräche über Physik und Nicht-Physik und alle Ratschläge, Ideen und Gefallen, die zu dieser Arbeit beigetragen haben. Das gleiche gilt für Michael Brüdgam (maskulin), der mit mir über viele Jahre in erschreckender Harmonie das Büro geteilt hat und mir mit seiner Freundschaft und Hilfsbereitschaft zur Seite stand.

Meinem Bruder Jan danke ich für seine stets klare Sicht der Dinge, seinen Zuspruch und seine Unterstützung.

Mein besonderer Dank gilt Frederik, der mir in allen Belangen eine große Hilfe war und mein Leben so bereichert hat.